CZECH TECHNICAL UNIVERSITY IN
PRAGUE

Faculty of Nuclear Sciences and Physical
Engineering

Department of Physics

Master's thesis

Charged charm mesons in Au+Au collisions

Bc. Jakub Kvapil

Supervisor: Mgr. Jaroslav Bielčík, Ph.D.

Consultant: Mgr. Pavol Federič, Ph.D
Consultant: Ing. Miroslav Šimko

Prague, 2017

ČESKÉ VYSOKÉ UČENÍ TECHNICKÉ
V PRAZE
Fakulta jaderná a fyzikálně inženýrská
Katedra fyziky

Diplomová práce

Nabité půvabné mesony v Au+Au srážkách

Bc. Jakub Kvapil

Vedoucí práce: Mgr. Jaroslav Bielčík, Ph.D.

Konzultant: Mgr. Pavol Federič, Ph.D
Konzultant: Ing. Miroslav Šimko

Praha, 2017

Katedra: fyziky

Akademický rok: 2016/2017

ZADÁNÍ DIPLOMOVÉ PRÁCE

Student: Bc. Jakub Kvapil

Studijní program: Aplikace přírodních věd

Obor: Experimentální jaderná a částicová fyzika

Název práce: Nabité půvabné mesony v Au+Au srážkách
(česky)

Název práce: Charged charm mesons in Au+Au collisions
(anglicky)

Pokyny pro vypracování:

1) Přehled měření půvabných mesonů v jádro-jaderných srážkách
2) Experiment STAR
3) Rekonstrukce mezonu D+
4) Korekce na geometrickou akceptanci detektoru a účinnost rekonstrukce
5) Jaderný modifikační faktor a srovnání s modely
6) Diskuze a závěr

Prohlášení:

Prohlašuji, že jsem svou diplomovou práci vypracoval samostatně a použil jsem pouze podklady (literaturu, projekty, software, atd.) uvedené v přiloženém seznamu.

Nemám závažný důvod proti užití tohoto školního díla ve smyslu § 60 Zákona č. 121/2000 Sb., o právu autorském, o právech souvisejících s právem autorským a o změně některých zákonů (autorský zákon).

V Praze dne 30.4.2017   Jakub Kvapil

Title:
Charged charm mesons in Au+Au collisions

Author: Bc. Jakub Kvapil

Specialization: Experimental nuclear and particle physics

Supervisor: Mgr. Jaroslav Bielčík, Ph.D.
Consultant: Mgr. Pavol Federič, Ph.D
Consultant: Ing. Miroslav Šimko

Abstract:

Charm quarks are mainly produced in hard processes at the beginning of heavy-ion collisions and can be used as a tool to study properties of the Quark-Gluon Plasma (QGP). The modification to D-meson production in heavy-ion collisions is sensitive to the energy loss of charm quarks in the QGP. The Heavy Flavor Tracker was installed at the STAR experiment in 2014 and it enables the topological reconstruction of the decay vertices for open charm mesons. It significantly improves precision on charm meson measurements. Besides the measurement of D^0, $D^{\pm}$ provides an additional handle and cross-check to study the interaction between the charm quarks and the medium.

In this thesis, we present the measurements of $D^{\pm}$ production in Au+Au collisions at $\sqrt{s_{\mathrm{NN}}} = 200$ GeV. $D^{\pm}$ mesons are reconstructed topologically via the hadronic decay channel $D^{\pm} \rightarrow K^{\mp}\pi^{\pm}\pi^{\pm}$ from the data collected in 2014 with the Heavy Flavor Tracker. The invariant yield of $D^{\pm}$ mesons as a function of transverse momentum as well as centrality is extracted. The nuclear modification factor is calculated and found to be consistent with the D^0. The experimental results are compared with the theoretical models.

Key words:
RHIC, STAR, HFT, $D^{\pm}$, invariant yield, R_{AA}, reconstruction efficiency, systematic uncertainties, Run14, Au+Au, 200 GeV

Název práce:
Nabité půvabné mezony v Au+Au srážkách

Autor: Bc. Jakub Kvapil

Obor: Experimentální jaderná a částicová fyzika

Vedoucí práce: Mgr. Jaroslav Bielčík, Ph.D.
Konzultant: Mgr. Pavol Federič, Ph.D
Konzultant: Ing. Miroslav Šimko

Abstrakt:

Těžké kvarky vznikají převážně při tvrdých procesech na začátku srážky těžkých iontů a proto mohou být použity jako sonda ke studiu vlastností Kvark-gluonového plazmatu (QGP). Produkce D mezonů ve srážkách těžkých iontů silně závisí na energetické ztrátě půvabných kvarků v QGP. Heavy Flavor Tracker byl nainstalován do experimentu STAR v roce 2014 a umožňuje topologickou rekonstrukci rozpadových vrcholů půvabných mezonů. Výrazně tím zvyšuje přesnost měření půvabných mezonů. $D^{\pm}$, vedle D^0, poskytuje nezávislé ověření interakce mezi půvabnými kvarky a médiem.

V této práci je ukázáno měření produkce $D^{\pm}$ v Au+Au srážkách při $\sqrt{s_{NN}} = 200$ GeV. $D^{\pm}$ mezony jsou zrekonstruovány topologicky přes hadronový rozpadový kanál $D^{\pm} \to K^{\mp}\pi^{\pm}\pi^{\pm}$ z dat naměřených v roce 2014 pomocí Heavy Flavor Trackeru. Invariantní výtěžek $D^{\pm}$ mezonů jako funkce transversální hybnosti a centrality je změřen. Jaderný modifikační faktor je vypočítán a je konzistentní s D^0. Experimentální výsledky jsou porovnány s teoretickými modely.

Klíčová slova:

RHIC, STAR, HFT, $D^{\pm}$, invariantní výtěžek, R_{AA}, efektivita rekonstrukce, systematické chyby, Run14, Au+Au, 200 GeV

Acknowledgement

Contents

List of Figures

List of Tables

Introduction

This work is dedicated to the ongoing research at Solenoidal Tracker At Relativistic heavy ion collider (STAR) experiment located in Brookhaven National Laboratory (BNL) in the USA. One method of studying extreme states of the nuclear matter are collider experiments. The main physics program of STAR is to study the ultra-relativistic heavy ion collisions in order to unravel the properties of nuclear matter at extreme state. Many particles are produced during heavy ion collision. From particles that can be detected in detector we infer the properties of nuclear matter created at the collision. Most of the produced particles are composed from light u and d quarks. In this work we focus to $D^{\pm}$.

$D^{\pm}$ is a meson (quark–antiquark bound state) containing a charm and down quark with decay length $\lambda = 311.8$ μm. Due to their large masses charm mesons are created during the initial phase of the collision and thus can be used to study the properties of following phases. Since the decay length is relatively short the meson decays before it reaches the detector. It must be reconstructed from its decay products, the decay channel used in this work is $D^{\pm} \to K^{\mp}\pi^{\pm}\pi^{\pm}$. As it is a three-body decay the combinatorial background is large, therefore this measurement became possible only after the vertex detector upgrade in the year 2014.

The first chapter is dedicated to the theoretical introduction of heavy ion collisions. It includes the descriptions of basic variables used in high energy physics, such as rapidity, pseudorapidity, luminosity, centrality, nuclear modification factor, flow and cold nuclear matter effects.

The second chapter describes the RHIC accelerator, its future plans and the STAR detector with the most important mid-rapidity subdetectors. The two most innermost layers of the Heavy Flavor Tracker (HFT) consist of pixel detectors build with novel MAPS technology. This is the first time when MAPS technology was used in a collider experiment. Contribution of the HFT to the tracking resolution with D^0 as example is discussed as well.

The third chapter introduces results of D meson measurements performed at STAR, ALICE (A Large Ion Collider Experiment), CMS (Compact Muon Solenoid) and LHCb (Large Hadron Collider beauty). The main goal of this work is to accomplish this type of measurement for $D^{\pm}$ at STAR.

The fourth chapter is dedicated to $D^{\pm}$ meson reconstruction with the HFT in the experimental data taken in the year 2014 in Au+Au collisions at $\sqrt{s_{\mathrm{NN}}} = 200$ GeV. Before the HFT installation at STAR in the year 2014, the D mesons were reconstructed without any topological cuts and the $D^{\pm}$ were impossible to reconstruct because three-body decay has large combinatorial background. However, with the introduction of the HFT and dramatic increase of the pointing resolution of STAR,

one can reduce the combinatorial background by several orders of magnitude by using topological reconstruction of the $D^\pm$ secondary vertices. As a complement measurement to the D^0, the new $D^\pm$ information provides additional handle to study the behavior of the c quark in the medium.

The yield corrections and systematic uncertainties are analyzed in chapter five. The detector efficiency and acceptance were obtained with the help of the data-driven fast simulator. Yield uncertainties were calculated by topological cuts variation. Correction of the bin p_T of the spectrum is discussed as well.

In the last chapter a nuclear modification factor (R_{AA}) of $D^\pm$ with comparison to STAR published D^0 R_{AA} measured in 2010 and the preliminary D^0 R_{AA} from 2014 is shown.

As it was stated above this work was done within STAR collaboration. During the years 2016-2017 I served 3 weeks as a STAR detector operator. Here I would like to specify my original contribution.

Service work

During the years 2015-2016 I was a member of STAR Heavy Flavor Tracker software group. My main task was to test, tune and compare the simulation of a newly developed MAPS slow simulator with a real data collected in the year 2014 at STAR. The simulator takes a significant role in pixel sensor efficiency estimation. This work was presented at 15th Zimányi School, Wigner Research Centre for Physics, Budapest, Hungary.

Data analysis

From 2016 I work in Heavy Flavor physics working group. I reconstructed signal of $D^\pm$ from Au+Au collisions from 2014 at $\sqrt{s_{NN}} = 200$ GeV. I have performed all steps of the analysis as described in chapters 4 and 5. I have developed selection criteria to identify $D^\pm$ candidates. I have QA (Quality Assurance) of the data, the QA plots was used as a input for Data-Driven fast simulator to get the reconstruction efficiency. The candidates were further analyzed and the background was subtracted. I have performed all corrections of the extracted yield and estimated systematic uncertainties. The results in the 0-10% centrality were approved as STAR preliminary and presented as a poster at a Quark Matter 2017 conference, Chicago, USA.

Chapter 1

Theoretical introduction

1.1 Quantum chromodynamics phase diagram

At near zero baryon density and critical temperature $T_c \simeq 170$ MeV quantum chromodynamics (QCD) predicts a phase transition between confined hadrons and deconfined quarks [1]. QCD is a gauge theory explaining strong interaction as an exchange of gluons between color charged particles. Gluons carry a color charge thus can self-interact. This implies that colored system is weakly coupled at short distances and strongly coupled on longer distances. This is called asymptotic freedom and confinement [2]. The Quark Gluon Plasma (QGP) is a state of matter with deconfined quarks and gluons. Figure 1.1 shows QCD phase diagram, phases are shown as a function of temperature T and baryo-chamical potential μ. At low temperature and/or baryo-chemical potential, particles are confined in hadrons e.g. protons and pions. When nuclear matter is at sufficient hight temperature it may undergo a phase transition to QGP. Finding the exact value of this critical temperature is one of the main tasks of Relativistic Heavy Ion Collider (RHIC). Enough energy to create QGP on Earth can be reached by colliding ultra-relativistic heavy ions in accelerators. It is also expected that naturally QGP exists inside neutron stars and was created shortly after the Big Bang.

After nucleus–nucleus collision, the kinetic energy of ions is transformed to heating of nuclear matter and creation of new particles. The dynamical evolution of created system can be divided into several phases:

1. Hard processes,

2. QGP formation - thermalization,

3. QGP hadronization,

4. QGP freeze out:

    chemical,

    kinetic.

During the hard processes phase, there is enough density and energy to produce heavy quarks (c,b). The system further expands until it is thermalized – the system follows collective behavior. The energy for creating heavy quarks is not sufficient
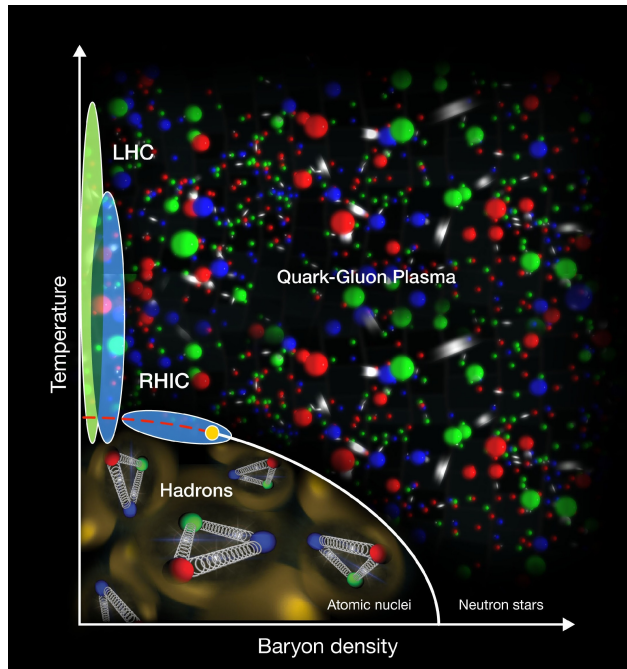
Figure 1.1: The QCD matter phase diagram in the plane of temperature T and baryo-chemical potential μ_B. The parton–hadron phase transition line from lattice QCD ends in a critical point E. Taken from Ref. [3].

at this moment, therefore their amount in conserved throughout the whole system evolution. The QGP is strongly interacting matter of quarks and gluons (partons), where the strong force is the main agent and its collective behavior can be described by hydrodynamical models. System further expands and cools down until the partons are transformed into hadrons, which is called hadronization. Hadrons can still interact between themselves until the rate of inelastic scattering is negligible and the, so called, chemical freeze out occur, after this, the abundance of hadrons is conserved. Finally, with growing distance between hadrons, elastic collisions are rarer until they disappear completely. This is called kinetic freeze out and from this point on, the hadrons momentum is conserved. The space-time evolution of the heavy-ion collision can be seen in Figure 1.2. First, hard processes take place until the QGP formation at around $\tau = 1$ fm/c. The system further evolves until critical temperature T_c is reached and hadronization takes place. Finally, the chemical and kinetic freeze out temperature T_{ch} and T_{fo} is achieved.

1.2 Heavy-ion collision variables

Our interest is to study this new interacting matter to understand the theory of strong force. We would like to obtain thermodynamical properties (temperature, energy density) and transport properties (viscosity). Before one can take more in depth immersion into the QGP study new variables [4], often used in heavy-ion collisions, will be defined.
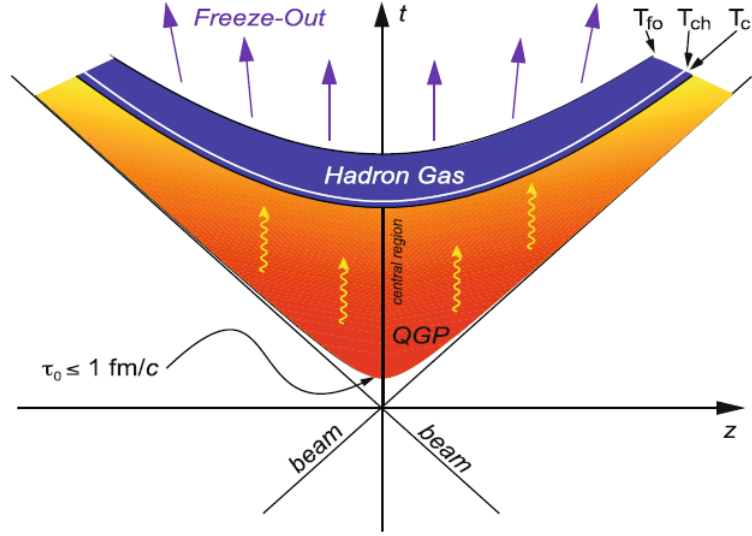
Figure 1.2: The space(z)-time(t) evolution of heavy ion collision. The T_C represents critical temperature, T_{ch} temperature of the chemical and T_{fo} of the kinematic freeze out. Taken from Ref. [5].

1.2.1 Rapidity

The coordinates along the beam line (z-axis) is called longitudinal and perpendicular is called transverse (x–y). The momentum can be decomposed into the longitudinal (p_z) and transverse $p_T = \sqrt{p_x^2 + p_y^2}$ part. Rapidity is defined as [6]:

$$y = \frac{1}{2} \ln \left(\frac{E + p_z}{E - p_z} \right), \qquad (1.1)$$

where the E is particle energy. Transverse momentum p_T is invariant under longitudinal Lorentz boost and rapidity changes by additive constant, thus particle momentum described in form (y, p_T) is an appropriate observable.

1.2.2 Pseudorapidity

Since it is difficult to compare rapidity directly to the measured properties for the detected particles, pseudorapidity was defined in its place. Let assume that a particle is emitted at an angle θ relative to the beam axis, rapidity can be rewritten [6] as

$$
\begin{aligned}
y &= \frac{1}{2} \ln \left(\frac{E + p_z}{E - p_z} \right) = \frac{1}{2} \ln \left(\frac{\sqrt{m^2 + p^2} + p \cos \theta}{\sqrt{m^2 + p^2} - p \cos \theta} \right) \overset{p \gg m}{=} \\
&= \frac{1}{2} \ln \left(\frac{p + p \cos \theta}{p - p \cos \theta} \right) = - \ln \tan \frac{\theta}{2} \equiv \eta
\end{aligned}
\qquad (1.2)
$$

There is only one quantity to be measured, angle θ which is independent of any particle identification - mass, momentum and collision energy.

1.2.3 Luminosity

Luminosity ($cm^{-2}s^{-1}$) [4] is the ability of a particle accelerator to deliver required amount of interactions defined, in case of colliders, as

$$L = fn\frac{N_1 N_2}{A},\tag{1.3}$$

where f is the revolution frequency, n number of bunches in one beam, N_1 and N_2 number of particles in each bunch and A cross-sectional area of the beams. The number of desired interactions is defined as

$$R = \sigma L,\tag{1.4}$$

where σ is the interaction cross-section.

1.2.4 Centrality

In a collision of two nuclei with diameters R_1 and R_2 one can define the impact parameter b [4]. It is the distance between the nuclei centers in transverse plane and can carry values from $b \approx 0$ (head-on – central collisions) to $b > (R_1 + R_2)$ (ultra-peripheral). The impact parameter can not be measured directly but it is estimated through, so called, multiplicity. Multiplicity is a number of good quality tracks measured by Time Projection Chamber, the more central collision, the more tracks are created. The relation between multiplicity and impact parameter can be determined by Glauber model [7]. Now e.g. the 5 % of events with highest multiplicity is defined as centrality range 0–5%. From the impact parameter, the number of participants N_{part} and the number of binary collisions N_{coll} can be estimated. As will be shown later, binary collisions are important for the measurement normalization. In more central collisions there is higher probability of QGP creation due to higher parton density.

1.3 Parton energy loss in QGP matter

As mentioned in the previous section, heavy quarks are created before the QGP formation, allowing them to propagate and be affected by the medium. With their abundance conservation during the system evolution they can be used as a good probe. The measured particle energy loss ΔE depends on particle characteristics (energy E, mass m) and plasma properties (temperature T, particle-medium coupling α, thickness L), where the particle characteristics and coupling constant can be predicted directly from QCD [8].

1.3.1 Mechanism of in-medium energy loss

In the most general case the total energy loss consists of two terms - collisional and radiative energy loss

$$\Delta E = \Delta E_{coll} + \Delta E_{rad}.\tag{1.5}$$

The collisional energy loss takes place via elastic scattering, while the radiative energy loss is by radiating a gluon. The radiative loss dominates at higher momenta,

yet if the particle is heavy, the amount of radiation at angle within a cone $\theta < \frac{M}{E}$ is suppressed by factor $\frac{m_D^2}{M^2}$, where m_D is the Debye mass. It characterizes the lowest momentum exchange with the medium. This suppression is known as the Dead cone effect [9] and it highly reduces the radiative energy loss of heavy quarks. It is expected that the energy loss of gluons, u,d and s quarks will be much larger then the energy loss of c and b quarks.

The collision energy loss of particle traversing distance l through hot and dense nuclear matter of thickness L can be described [8]: for a light lepton ($M^2 \ll ET$)

$$-\frac{\mathrm{d}E_{coll}}{\mathrm{d}l} \approx \frac{\pi}{3}\alpha m_D^2 \ln\left(\frac{ET}{m_D^2}\right) \tag{1.6}$$

and for a heavy lepton ($M^2 \gg ET$)

$$-\frac{\mathrm{d}E_{coll}}{\mathrm{d}l} \approx \frac{2\pi}{3}\alpha m_D^2 \ln\left(\frac{ET}{m_D M}\right). \tag{1.7}$$

The radiative energy loss depends on the thickness of the plasma L and particle mean free path λ, in case of thin medium ($L \ll \lambda$)

$$-\frac{\mathrm{d}E_{rad}}{\mathrm{d}l} \approx \alpha^3 T^3 L \tag{1.8}$$

and for thick medium ($L \gg \lambda$)

$$-\frac{\mathrm{d}E_{rad}}{\mathrm{d}l} \approx \alpha^2 \sqrt{ET^3 \ln\left(\frac{E}{T}\right)}. \tag{1.9}$$

In general, the radiative losses of an energetic lepton crossing QGP are much larger than collisional losses [8]. In case of light quarks and gluons the collisional energy loss can be described as

$$-\frac{\mathrm{d}E_{coll}}{\mathrm{d}l} \approx \frac{1}{4}C_R\alpha_s(ET)m_D^2 \ln\left(\frac{ET}{m_D^2}\right), \tag{1.10}$$

where C_R is the quark (gluon) color charge. In case of heavy quarks the energy loss is

$$-\frac{\mathrm{d}E_{coll}}{\mathrm{d}l} \approx -\frac{2}{9}C_R\pi\left(\alpha_s(M^2)\alpha_s(ET)\ln\left(\frac{ET}{m_D^2}\right)\right). \tag{1.11}$$

The radiative loss of quarks and gluon in thin medium ($L \ll \lambda$) is proportional to

$$\Delta E_{rad} \approx \alpha_s C_R q L^2 \ln\left(\frac{E}{m_D^2 L}\right) \tag{1.12}$$

and for thick medium ($L \gg \lambda$)

$$\Delta E_{rad} \approx \alpha_s C_R q L^2 \begin{cases} 1 & (\omega < \omega_c) \\ \ln\left(\frac{E}{qL^2}\right) & (\omega > \omega_c) \end{cases} \tag{1.13}$$

where $\omega_c = \frac{1}{2}qL^2$ is the characteristic gluonstrahlung energy and q is the transport coefficient [8].

Experimentally we can compare particle yields in Au+Au and p+p collisions (see 1.4) in order to access the information about possible energy loss of high p_T particles. However this can be done only as model comparison. The phenomenological models differs in detail how collisional and radiative energy loss is taken into account.

1.4 Consequences of energy loss and Nuclear modification factor

The energy loss can be addressed experimentally by comparing the yield of hard particles produced in ion-ion and proton-proton collisions scaled by number of binary collisions. The Nuclear modification factor (R_{AA}) is defined [2] as

$$R_{AA} = \frac{1}{\langle N_{coll} \rangle} \frac{\frac{\mathrm{d}N_{AA}}{\mathrm{d}p_T}}{\frac{\mathrm{d}N_{pp}}{\mathrm{d}p_T}}, \tag{1.14}$$

where N_{coll} is the average number of binary collisions, $\frac{\mathrm{d}N_{AA}}{\mathrm{d}p_T}$ is the particle invariant yield in ion–ion collisions and $\frac{\mathrm{d}N_{pp}}{\mathrm{d}p_T}$ invariant yield in proton–proton collisions. One of the goals of this thesis is to calculate the nuclear modification factor of the $D^\pm$.

1.5 Hydrodynamic Flow

Together with the invariant yield and nuclear modification factor, another important observable is the Hydrodynamic Flow [2]. As mentioned above, QGP is a hot and dense strongly interacting matter showing collective behavior, which can be described by hydrodynamical calculation. The particles azimuthal momentum distribution can be expanded into a Fourier series

$$E\frac{\mathrm{d}^3N}{\mathrm{d}^3p} = \frac{1}{2\pi}\frac{\mathrm{d}^2N}{p_\mathrm{T}\mathrm{d}p_\mathrm{T}\mathrm{d}y}\left(1 + 2\sum_{n=1}^{\inf} v_n \cos\left[n(\phi - \Psi_{RP})\right]\right), \tag{1.15}$$

where E is the energy, p momentum, p_T transverse momentum, y rapidity, $v_n = \langle\cos\left[n(\phi - \Psi_{RP})\right]\rangle$ is the Fourier coefficient of n-th harmonics and ϕ is the angle and Ψ_{RP} reaction plane angle, which is a plane in direction of the beam line on connector of two colliding nuclei centers. The most measured harmonics are the v_1, v_2 and v_3 which are called the direct, elliptic and triangular flow. Early measurements at RHIC energy shows, that the v_2 for the most peripheral collisions at STAR was 50% larger than at SPS at CERN and was concluded to me non-zero. This was for the first time a non-zero v_2 was measured [10]. The latest measurement of D^0 elliptic flow in minimum bias $\sqrt{s_\mathrm{NN}} = 200$ GeV collisions measured by STAR detector can be seen in Figure 1.3. The TAMU [11] model uses a non-perturbative approach assuming the two-body interaction is a function od transferred 4-momentum. The TAMU model including charm diffusion corresponds with data while the prediction without diffusion is systematically lower [12]. Diffusion coefficient $D = 2\frac{T^2}{\kappa}$, characterizes the dynamics of heavy non-relativistic particles traversing the plasma, where T is the plasma temperature and κ represents the momentum space diffusion coefficient of heavy quarks. [8]. The SUBATECH [13] employs perturbative QCD with Hard Thermal Loop approximation for soft collisions and the Duke [14] model treats the diffusion coefficient as a free parameter, which has been constrained by LHC R_{AA}. The last model underpredicts the v_2 observed in data [12]. The v_2 and R_{AA} is important for model validation. It is expected that model should describe both observables at once, which as will be discussed later, is not always precise.
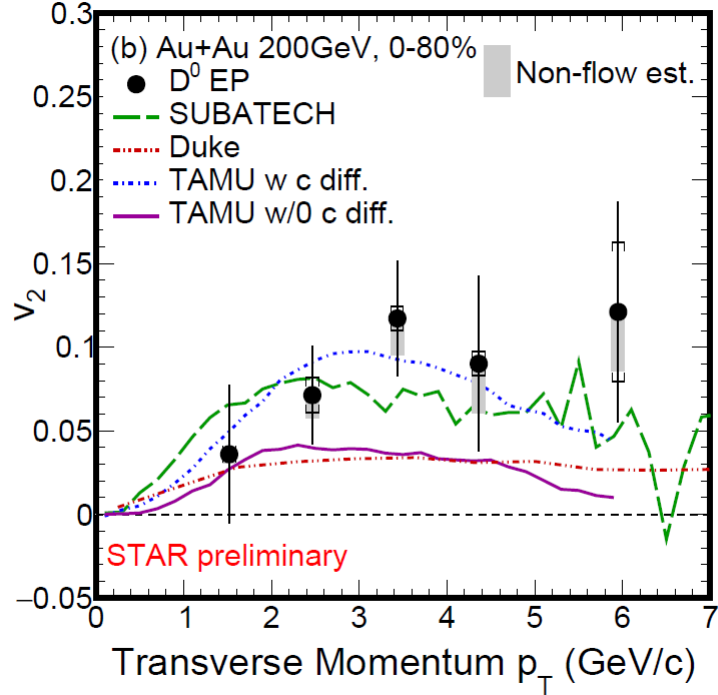
Figure 1.3: D^0 v_2 for 0–80% centrality at $\sqrt{s_{NN}} = 200$ GeV Au+Au collisions measured at the STAR detector and compared to theoretical models. Taken from Ref. [12].

1.6 Cold Nuclear Matter effects

Characterizing the QGP in ion-ion collisions requires the understanding of the effect induced by the presence of nuclei, the so called cold nuclear matter (CNM) effects [15,16]. Open heavy flavor production can be affected by the following CNM effects:

- Nuclear modification to parton distribution function (PDF). This effect is often referred as shadowing when the modification is positive and anti-shadowing when negative with respect to unmodified PDF.

- Multiple scattering of partons in the nucleus leading to parton energy loss and transverse momentum broadening, the Cronin effect.

- Nuclear absorption of bound state when passing through nucleus.

- To study a set of particles produced in proton-ion collisions which may be responsible for open flavor modification and thus clarify whenever this set of particles could form in QGP.

These effects can be studied in proton-ion or deuteron-ion collisions. CNM effects can be quantified by nuclear modification factor R_{pA} defined as

$$R_{pA} = \frac{1}{\langle N_{coll} \rangle} \frac{\frac{\mathrm{d}N_{pA}}{\mathrm{d}p_T}}{\frac{\mathrm{d}N_{pp}}{\mathrm{d}p_T}}, \tag{1.16}$$

where N_{coll} is the number of binary collisions, $\frac{\mathrm{d}N_{pA}}{\mathrm{d}p_T}$ is the particle invariant yield in proton-ion collisions and $\frac{\mathrm{d}N_{pp}}{\mathrm{d}p_T}$ is the invariant yield in proton-proton collisions. In absence of CNM effects the R_{pA} is equal to unity.

Nuclear modification factor R_{pPb} of D-mesons (average of D^0, D^+, D^{*+} and D_s^+) in p-Pb collisions at $\sqrt{s_{NN}} = 5.02$ TeV can be seen in Figure 1.16. The measurement is compared with theoretical calculations including various CNM effects and the R_{pPb} is equal to unity within uncertainties.
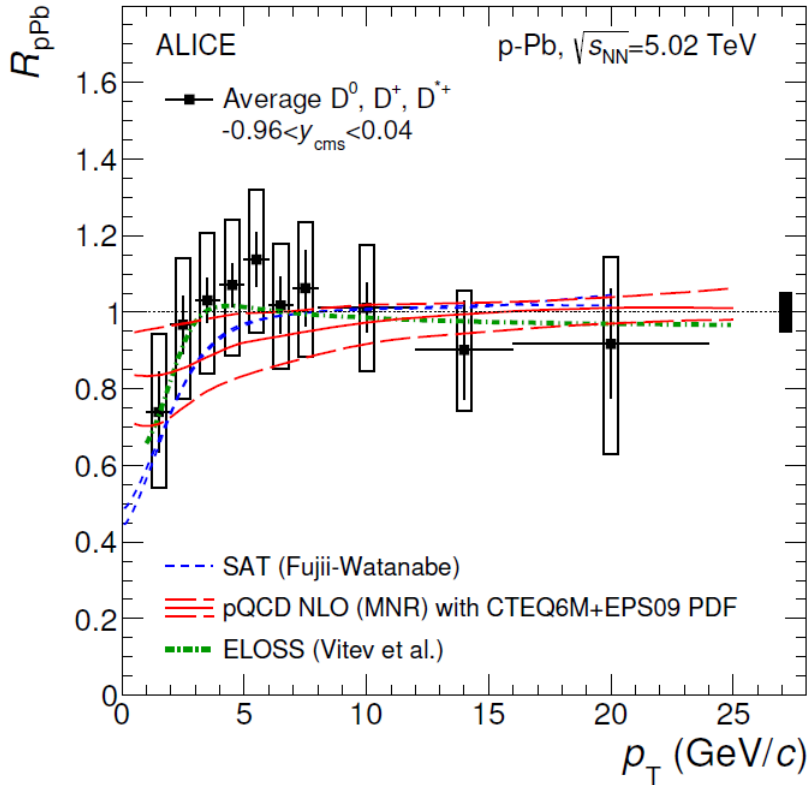
Figure 1.4: Nuclear modification factor R_{pPb} of D-mesons in p-Pb collisions at $\sqrt{s_{NN}} = 5.02$ TeV as a function of transverse momentum measured with the ALICE detector. The measurement is compared with theoretical calculations including various CNM effects. Taken from Ref. [16].

Chapter 2

Overview of charm mesons measurements

Charm quarks are predominantly produced in hard processes before the QGP formation and can be used as a good probe of the medium created in ultra-relativistic heavy-ion collisions, as has been discussed in previous chapter. There are measurements of several charm D-mesons which are worth studying, namely the D^0, $D^\pm$, $D^{*\pm}$ and D_s^+ with their main decay hadronic channels [17]:

$$
\begin{aligned}
D^0 &\to K^-\pi^+, \\
D^+ &\to K^-\pi^+\pi^+, \\
D^{*+} &\to D^0\pi^+, \\
D_s^+ &\to K^-K^+\pi^+,
\end{aligned}
\tag{2.1}
$$

and their charge conjugates. Their branching ratios and decay lengths are (3.88 ± 0.05) % and 123 μm, (9.13 ± 0.19) % and 312 μm, (67.7 ± 0.05) % and (2.24 ± 0.13) %, respectively. The $D^{*\pm}$ decays by strong interaction and D_s^+ contains a strange quark. At STAR, D^0 are the most experimentally approachable as they decay into two charged particles and they are the most abundant in heavy-ion collisions. The $D^\pm$ is the most abundant three-body decay in comparison to other studied D-mesons, hence these measurement together provides interesting handle to study various aspects of physics. The abundance is proportional to c quark fragmentation functions [18]

$$
\begin{aligned}
f(c \to D^0) &= 0.565 \pm 0.032 \\
f(c \to D^+) &= 0.246 \pm 0.020 \\
f(c \to D^{*+}) &= 0.224 \pm 0.028 \\
f(c \to D_s^+) &= 0.080 \pm 0.017
\end{aligned}
\tag{2.2}
$$

If the coalescence mechanism (quark recombination) takes significant role for charm quark, the D_s^+ can help to unravel the strange quark enhancement.

In this chapter an example of these measurements performed at STAR, ALICE, CMS and LHCb will be shown.

2.1 STAR

The charm quark cross section (invariant yield divided by luminosity) can be calculated from an amplitude by summing the three lowest order (Leading order - LO) diagrams for charm quark. One can evaluate them at the Next-to-leading order (NLO) level including diagrams of order α^2 and α^3, where α is the strong interaction coupling constant. Finally, extending this calculation by including term of order $\alpha^2 \left(\alpha \log \left(\frac{p_T}{m_q} \right) \right)^k$ (Leading Log) and $\alpha^3 \left(\alpha \log \left(\frac{p_T}{m_q} \right) \right)^k$ (Next-to-leading Log) one gets the, so called, Fixed-Order Next-to-Leading-Log (FONLL) model [2]. The charm quark cross-section measured from (D^0 and D^*) in 2009 at $\sqrt{s_{NN}} = 200$ GeV p+p collisions compared with FONLL calculation can be seen in Figure 2.1. The data in p+p collisions are well described on the upper bound of FONLL calculation [19].
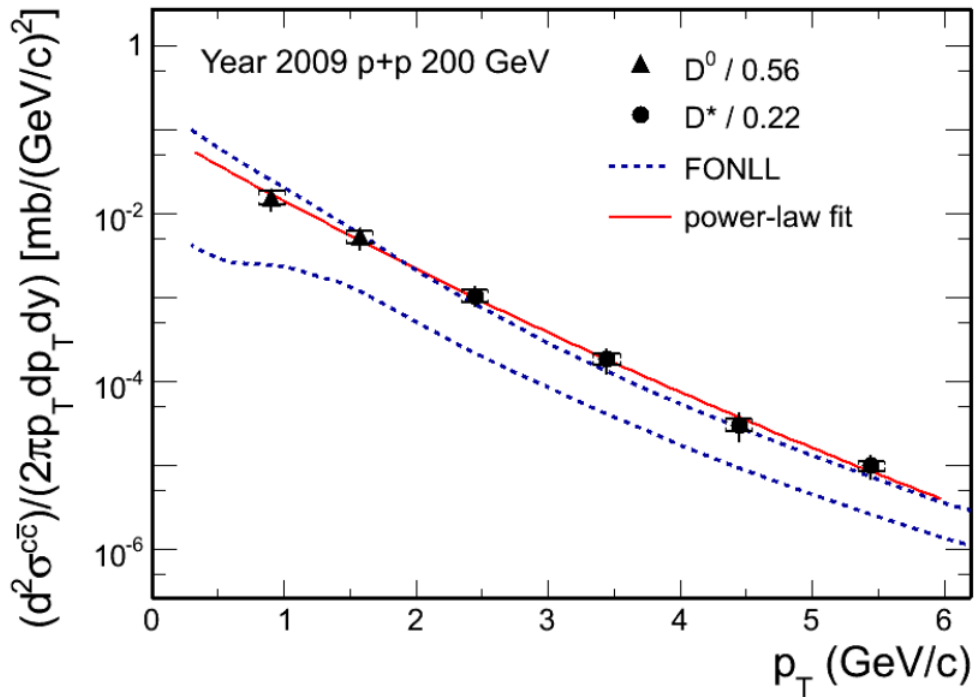
Figure 2.1: The $c\bar{c}$ pair production cross-section as a function of the transverse momentum p_T in $\sqrt{s_{NN}} = 200$ GeV p+p collisions measured by the STAR detector. FONLL model is included and compared to the data. Taken from Ref. [19].

The STAR R_{AA} measurement of D^0 in Au+Au collisions in the centrality range 0–10% and flow v_2 in centrality range 0–80% at $\sqrt{s_{NN}} = 200$ GeV can be seen in Figure 2.2. Comparison between measurement in year 2010/2011 and 2014 as well as comparison with models is shown. The D^0 exhibits a high suppression for higher momentum and the measurement from the year 2014, which was done with the help of HFT, confirms this trend. As can be seen, the HFT increases the reconstruction precision and greatly reduces the statistical uncertainties. The gray bands indicate a systematic uncertainty of proton-proton reference that comes from the experimental

setup from 2011 (without the HFT). The Duke [14] model uses a Langevin simulation with diffusion coefficient $2\pi T D_s = 7$, where D_s is heavy quark spacial diffusion coefficient and T is the medium temperature. The TAMU [11] calculation uses a non-perturbative approach and the T-matrix calculation which predicts $2\pi T D_s \sim 2-10$. The SUBATECH [13]uses a perturbative QCD calculation with Hard Thermal Loop, where $2\pi T D_s \sim 2-4$. As has been mentioned in previous chapter one needs a model which describes both R_{AA} and v_2. The TAMU and SUBATECH calculation describes both observables, while the Duke calculation underestimates the v_2 [20].

The measurement of D_s^+ with HFT can be seen in Figure 2.3. The D_s^+ in Au+Au collisions exhibits high enhancement in transverse momentum $2 < p_T < 4$ GeV/c in comparison to p+p collisions. The production of $D^\pm$ is the main task of this work and will be discussed later in this thesis.

2.2   ALICE

The ALICE (A Large Ion Collider Experiment) experiment at CERN measured production of charmed mesons D^0, $D^\pm$ and $D^{*\pm}$ in Pb-Pb collisions at $\sqrt{s_{NN}} = 2.76$ TeV. Particles were reconstructed via their hadronic decay channels mentioned above where for the D^{*+} reconstruction a D^0 topology was used. The D^0, D^+ and D^{*+} invariant yield in the 0-10% and 30-50% centrality range in Pb-Pb $\sqrt{s_{NN}} = 2.76$ TeV collisions can be seen in Figure 2.4. D^{*+} is scaled for visibility, the horizontal line represent the bin widths, where symbols are placed in the bin center.

The nuclear modification factor is shown in Figure 2.5. The D^0 points are placed in the bin center while D^+ and D^{*+} are shifted for better visibility. The global uncertainty represents the normalization error. D-mesons are compatible within uncertainties for both centrality classes, showing a high suppression. For the 0–10% most central collisions the suppression is maximal for $p_T = 10$ GeV/c, i.e. yield is reduced by factor 5 with respect to the proton-proton reference. The suppression of yields for the 30–50% centrality is smaller than in the most central collisions.

The comparison with STAR's data shown in Chapter 2.1 is in Figure 2.6. The average ALICE D-meson R_{AA} is compared to STAR D^0 R_{AA} in the 0–10% most central collisions. The suppression is consistent within uncertainties for $p_T > 2$ GeV/c. Since the nuclear modification factor is sensitive to the p_T spectra in proton-proton collisions, the combined effect of a denser medium and harder proton spectra at LHC could result in similar values of R_{AA} as at a lower collisions energies [21]. At lower p_T STAR shows a maximum, this effect can be described by models including parton energy loss, collective radial flow and the contribution to charm quark recombination and diffusion in the medium. The ALICE results do not show a maximum. However, due to large uncertainties of both measurements a firm conclusion cannot be made. The difference can be explained by different collision energies – with growing energy the suppression is expected to rise. Another explanation could be the Cronin effect.
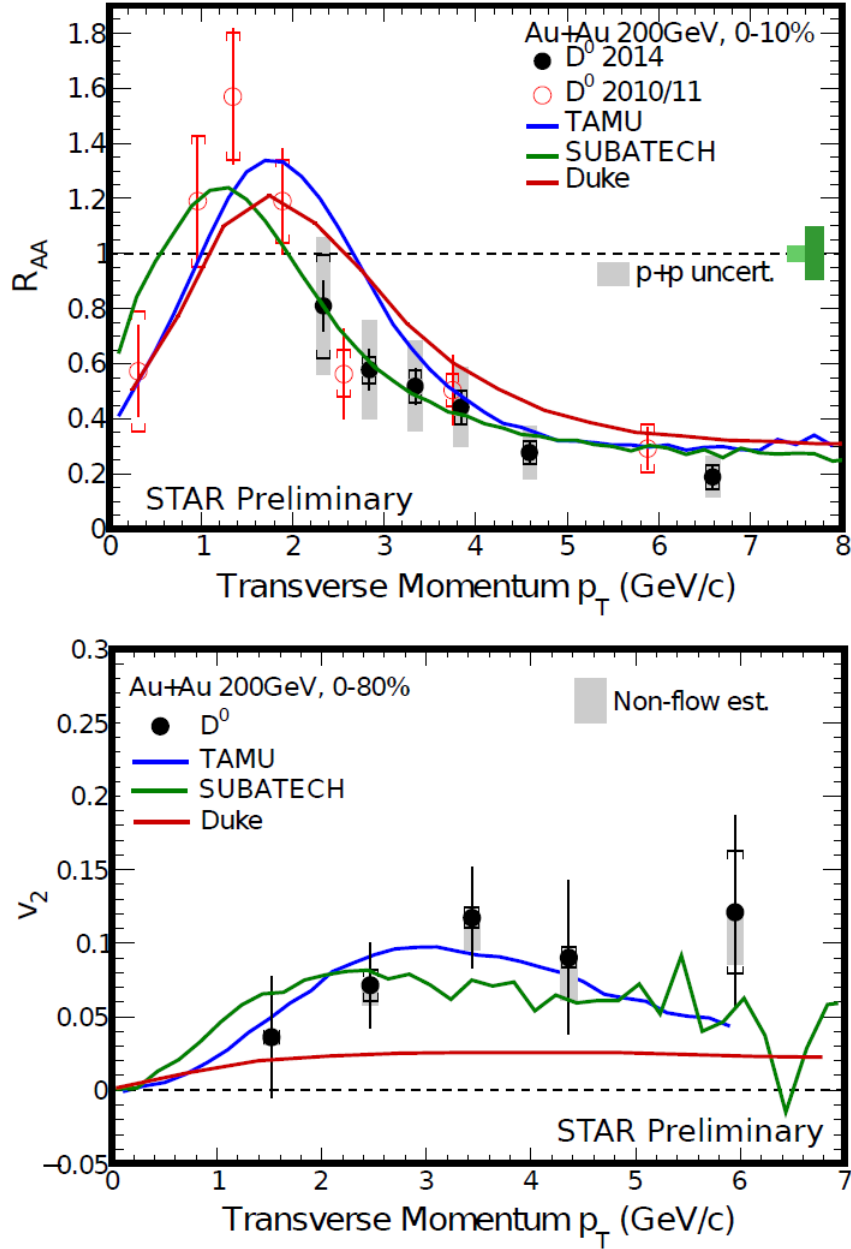
Figure 2.2: The D^0 nuclear modification factor in the 0–10% centrality range in Au+Au $\sqrt{s_{NN}} = 200$ GeV collisions compared to theoretical models measured by the STAR detector in year 2010 and 2014. Taken from Ref. [20].
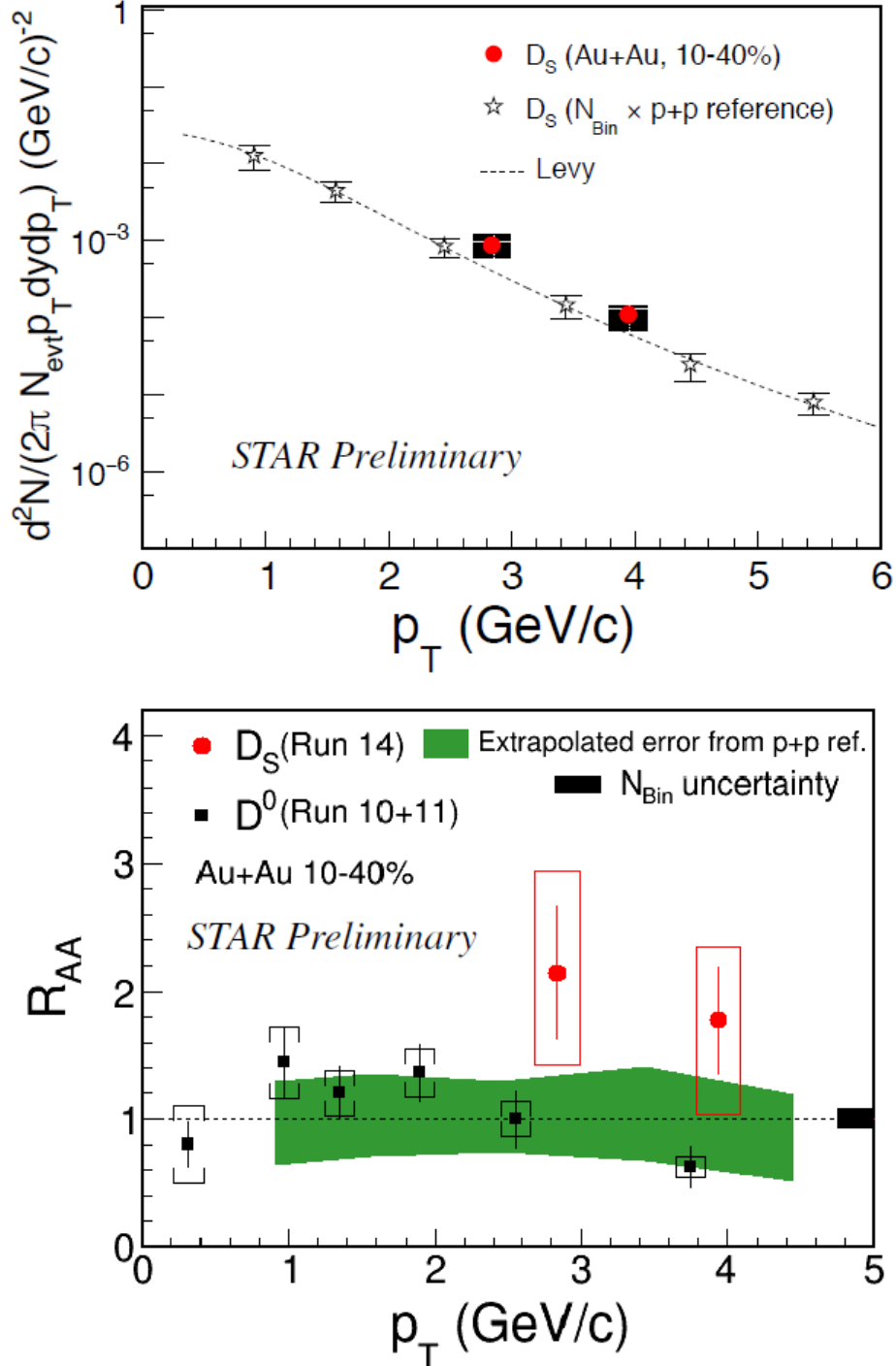
Figure 2.3: The D_s^+ invariant yield (top) and R_{AA} (bottom) in the 10–40% centrality range in Au+Au $\sqrt{s_{NN}} = 200$ GeV collisions compared to p+p $\sqrt{s} = 200$ GeV collisions measured by the STAR detector. Taken from Ref. [22].
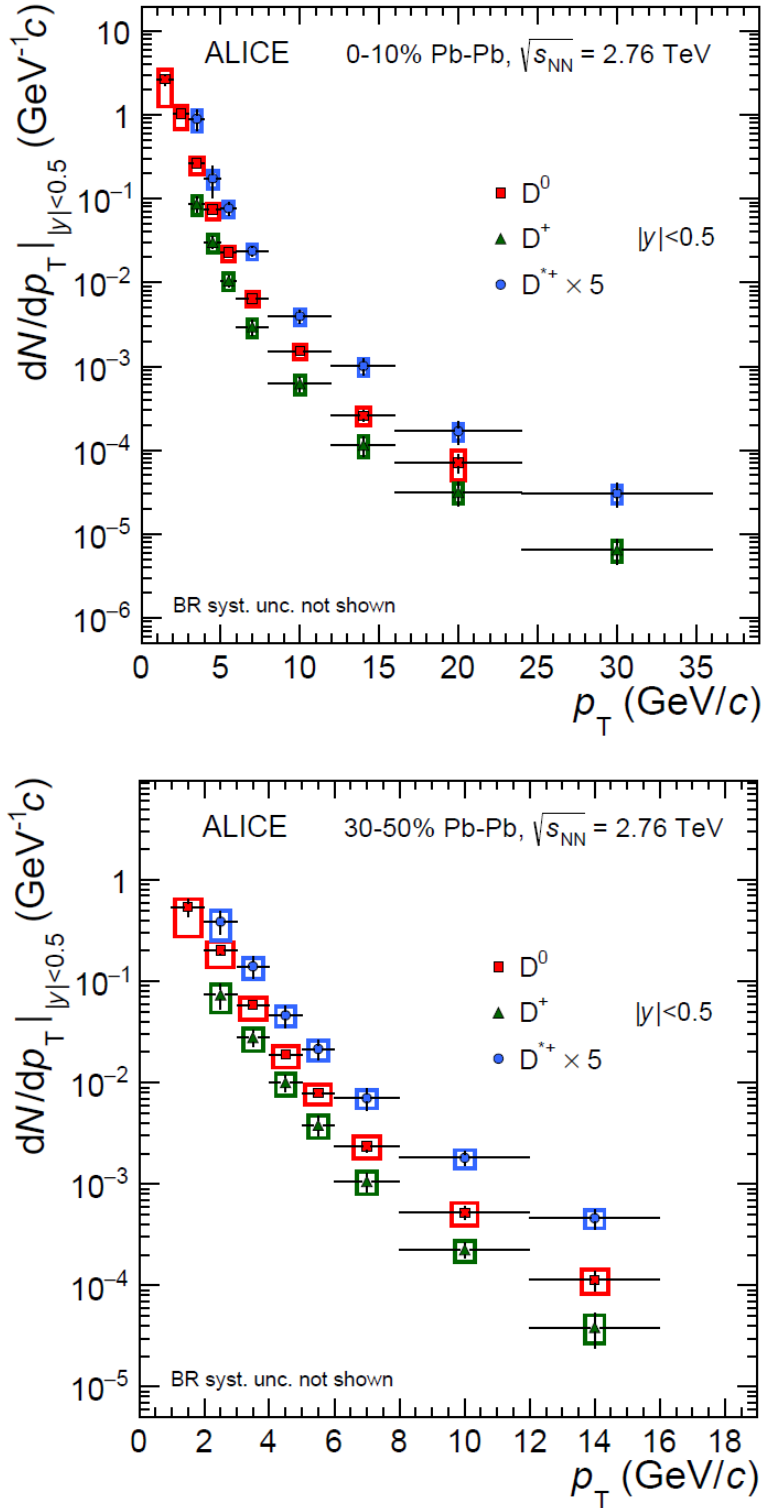
Figure 2.4: The D^0, D^+ and D^{*+} invariant yield in the 0–10% and 30–50% centrality range in Pb-Pb $\sqrt{s_{NN}} = 2.76$ TeV collisions measured by the ALICE detector. D^+ and D^{*+} are shifted for better visibility. Taken from Ref. [21].
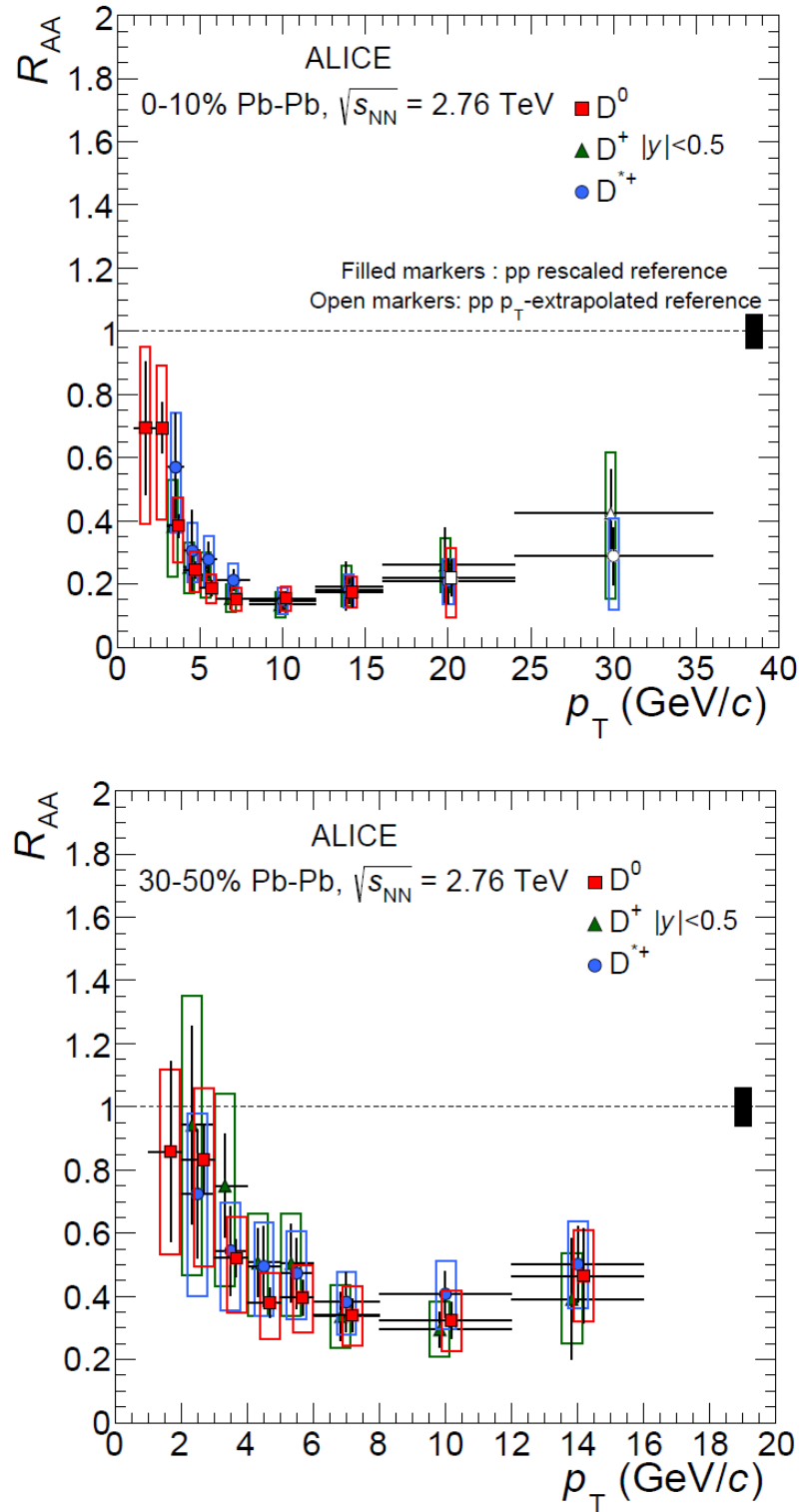
Figure 2.5: The D^0, D^+ and D^{*+} nuclear modification factor in the 0–10% and 30–50% centrality range in Pb-Pb $\sqrt{s_{NN}} = 2.76$ TeV collisions measured by the ALICE detector. Taken from Ref. [21].
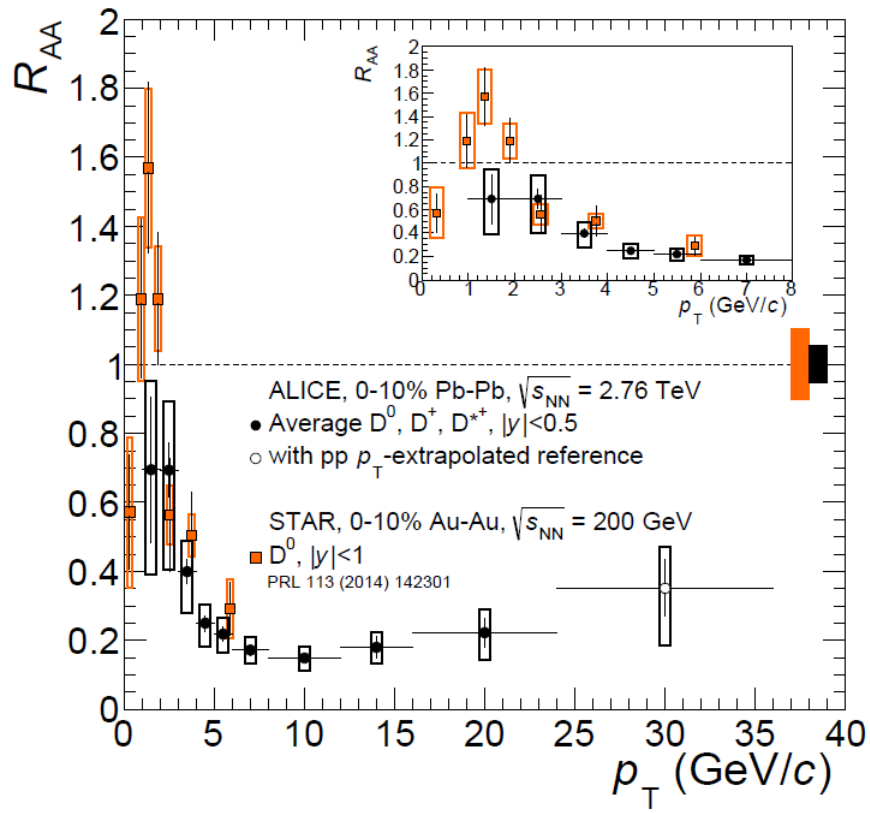
Figure 2.6: The averaged D^0, D$^+$ and D^{*+} nuclear modification factor measured by ALICE experiment compared to STAR's D^0 in the 0–10%. Taken from Ref. [21, 23].

2.3 CMS

The p_T-differential cross section of prompt D^0 mesons in p+p collisions at $\sqrt{s_{NN}} = 5.02$ TeV measured by the CMS detector in central rapidity $|y| < 1$ can be seen in Figure 2.7. The prediction of FONLL is superimposed in the figure and the ratio between data and prediction is shown bellow. The measurement lies in the upper bound of FONLL prediction. The nuclear modification factor in Figure 2.8. it shows a suppression by factor 4 at p_T around 6 GeV/c and at higher p_T the suppression decreases to a value of about 1.5. Measurement of charged hadrons for an equivalent event selection is included. Within uncertainties both measurements are consistent. The CMS measurement is consistent with the ALICE measurement in p_T up to 40 GeV/c. The ALICE is showing maximum suppression $R_{AA} = 0.2$ around $p_T = 10$ GeV/c while CMS around $p_T = 7$ GeV/c. Both measurements start to rise up to $R_{AA} = 0.4$ at $p_T = 40$ GeV/c. Further, CMS greatly expands the measurement up to $p_T = 100$ GeV/c with a extreme for $R_{AA} = 0.8$.
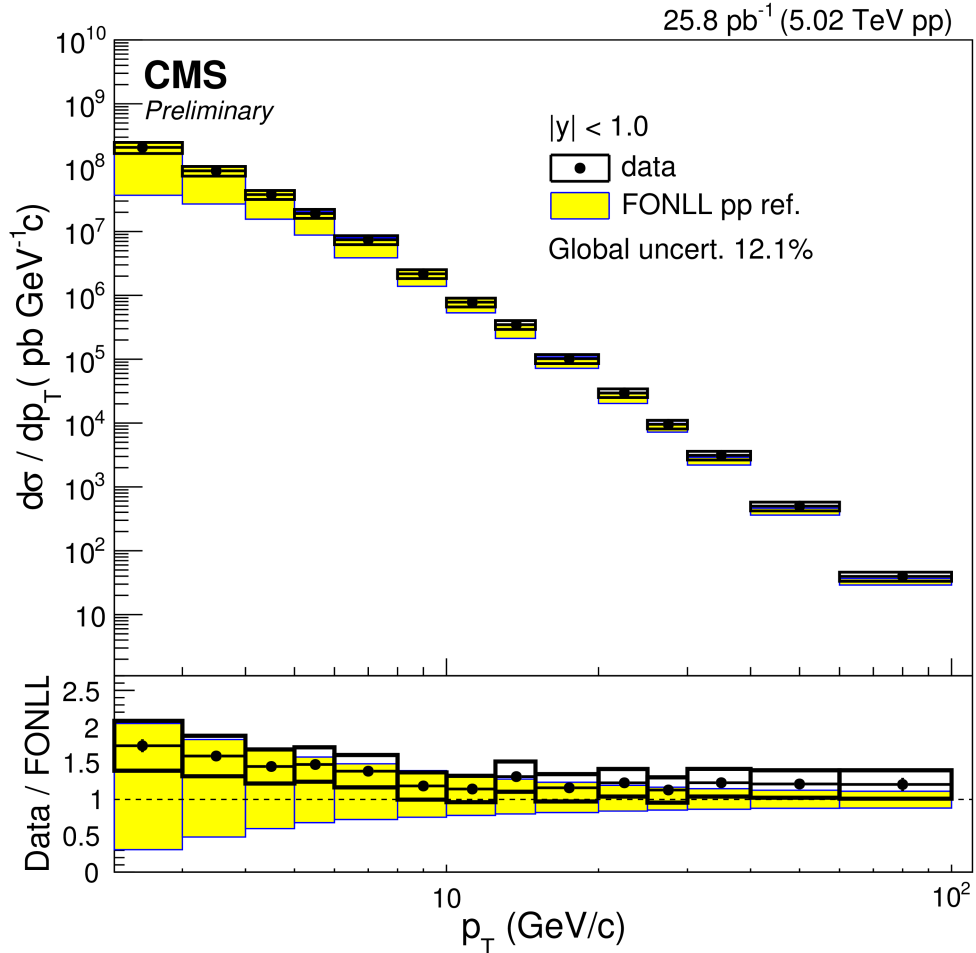
Figure 2.7: The p_T-differential cross section of prompt D^0 mesons in pp collisions at $\sqrt{s_{NN}} = 5.02$ TeV compared to the FONLL predictions measured by the CMS detector. Taken from Ref. [24].
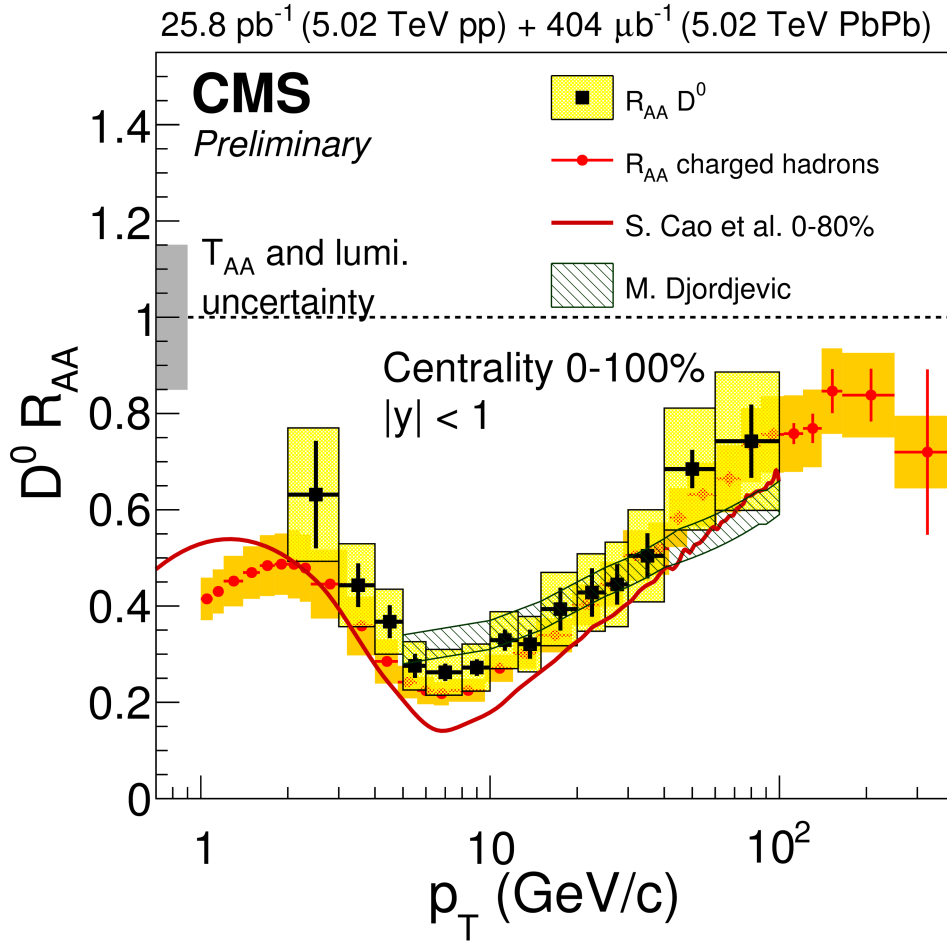
Figure 2.8: The D^0 nuclear modification factor in the 0–100% centrality in pp $\sqrt{s_{\mathrm{NN}}} = 5.02$ TeV collisions measured by the CMS detector. Taken from Ref. [24].

2.4   LHCb

The measurement of prompt D^0, and D^+ cross-sections in pp at $\sqrt{s} = 13$ TeV in forward rapidity measured by the LHCb detector can be seen in Figure 2.9 and measurement of D_s^+, and D^{*+} in Figure 2.10. The FONLL prediction in included and the data lies on the upper bound of prediction similarly to CMS and STAR measurement.
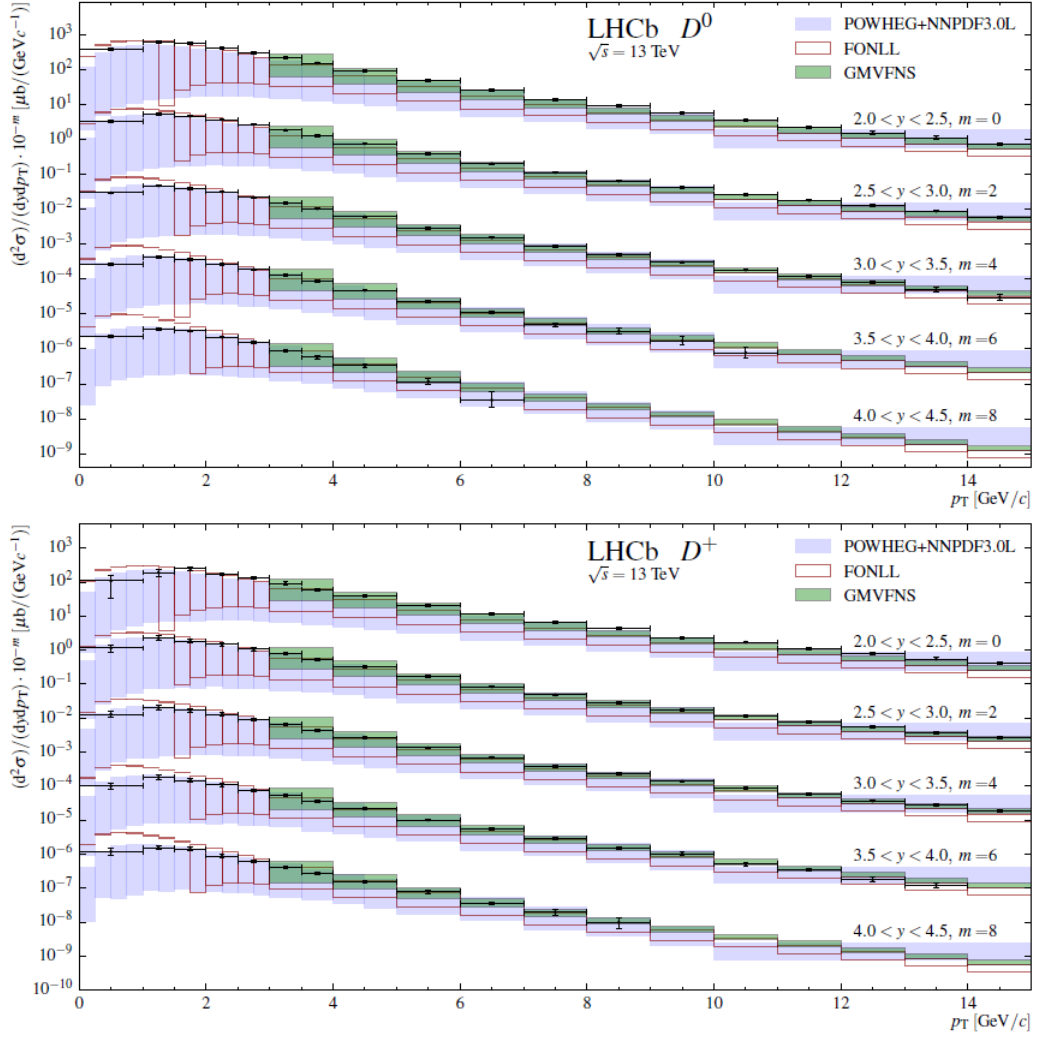
Figure 2.9: Measurements and predictions for the absolute prompt D^0, and D^+ cross-sections in pp at $\sqrt{s} = 13$ TeV measured by the LHCb detector. Each measurement and prediction in given rapidity is offset by a multiplication factor 10^{-m}, where m is shown on the plots. The boxes indicate the uncertainty band on the theory predictions, in cases where this band spans more than two orders of magnitude only its upper edge is indicated. Taken from Ref. [25].
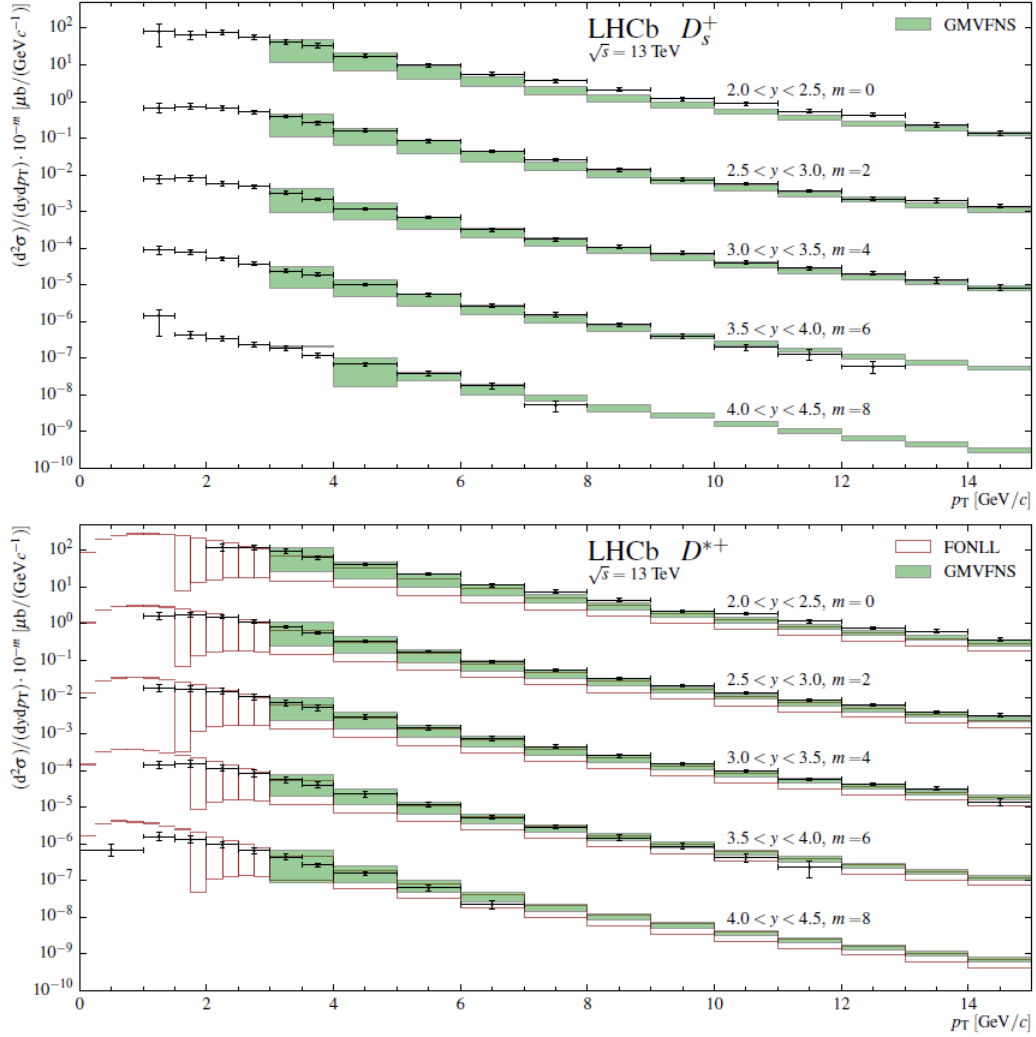
Figure 2.10: Measurements and predictions for the absolute prompt D_s^+, and D^{*+} cross-sections in pp at $\sqrt{s} = 13$ TeV measured by the LHCb detector. Each measurement and prediction in given rapidity is offset by a multiplication factor 10^{-m}, where m is shown on the plots. The boxes indicate the uncertainty band on the theory predictions, in cases where this band spans more than two orders of magnitude only its upper edge is indicated. Taken from Ref. [25].

Chapter 3

Solenoidal Tracker at RHIC

In this chapter, Brookhaven National Laboratory and Relativistic Heavy Ion Collider situated in BNL is described including up to date experimental plans for the years 2017 and 2018. STAR experiment and its main mid–rapidity detectors are shown, i.e. Muon Telescope detector, Barrel Electromagnetic Calorimeter, Time of Flight, Time projection Chamber and Heavy Flavor Tracker (Silicon Strip Tracker, Intermediate Silicon Tracker and Pixel detectors). Finally, the importance of the Heavy Flavor Tracker at STAR is shown with respect to heavy–flavor measurements.

3.1 Brookhaven National Laboratory (BNL)

Brookhaven National Laboratory was established in 1947 on the eastern end of Long Island to explore the peaceful applications of atomic energy. During the years Brookhaven broaden its scope to various fields from basic and applied research. The example of current facilities [26] includes:

- Relativistic Heavy Ion Collider (RHIC),

- National Synchrotron Light Source II (NSLS-II) - nanometer scale resolution imaging technique,

- Center for Functional Nanomaterials (CFN) - state-of-the-art tools for creating and exploring the properties of nanomaterials,

- NASA Space Radiation Laboratory (NSRL) - simulation of space radiation using RHIC beam

- Brookhaven Linac Isoptope Producer (BLIP) - research of radioisotopes, used in cancer treatment and diagnosis.

Historically, there have been other significant facilities [27, 28]:

- Cosmotron (1952 - 1966) - first GeV energy accelerator with energy 3.3 GeV,

- Alternating Gradient Synchrotron (AGS) (1960-) - 33 GeV accelerator currently used as pre-accelerator for RHIC,

- National Synchrotron Light Source (NSLS) (1982-2014),

- Brookhaven Graphite Research Reactor (BGRR) (1950-1968) - neutron experiments,

- High Flux Beam Reactor (HFBR) (1965-1996) - BGRR successor,

- Brookhaven Medical Research Reactor (BMRR) (1959-2000) - neutron flux for medical research.

Seven Nobel prices [29] were awarded to scientists from BNL:

- 1959 - T. D. Lee and C. N. Yang - parity violation (Cosmotron),

- 1976 - C. C. Ting - J/ψ discovery (AGS),

- 1980 - J. W. Cronin and V.L. Fitch - charge–parity violation (AGS),

- 1988 - L. Lederman, M. Schwartz and J. Steinberg - muon neutrino discovery (AGS),

- 2002 - R. Davis - detection of Cosmic neutrinos,

- 2003 - R. MacKinnon - the chemistry of Cell (NSLS),

- 2009 - V. Ramakrishnan - atomic level picture of ribosome (NSLS).

Other than the Nobel prices, several other discoveries [30] have been made:

- quark-gluon plasma,

- K meson, Ω^-, charmed and Σ baryons, Φ meson, Ξ antiparticles,

- MagLev - magnetically levitated transportation,

- first video game,

- Tc^{99m} - most widely used radioisotope for imaging diseased organs,

- human insulin - The first chemical synthesis of a human protein,

- strong focusing (alternating) for magnets (used at AGS).

3.2 Relativistic Heavy Ion Collider (RHIC)

The Relativistic Heavy Ion Collider , which started its operation in 2000, is located in the Brookhaven National Laboratory in Upton, New York. After the Large Hadron Collider , it is the second largest particle accelerator in the world. Furthermore, it is the only ultra-relativistic accelerator capable of colliding polarised protons [31]. The current spokesperson of the STAR experiment is Zhangbu Xu [32] and is composed of 61 institution from 13 countries, with a total of 602 collaborators [33].

RHIC is, so called, storage ring collider, two independent rings are filled with particles, accelerated in opposite direction and collided in interaction points. The collider can hold and collide particles up to 10 hours and can accelerate different types of positively charged ions. The accelerator has a hexagonal shape, is 3834 m

long, contains 1740 Ni-Ti superconducting magnets with the magnetic field of 3.45 T to bend the beam trajectory. RHIC contains a total of 6 interaction points where the rings intercept. Each interaction point is numbered similarly as on a clock. At 6 o'clock, the injector and the STAR (Solenoidal Tracker at RHIC) experiment is located. Experiment PHENIX located at 8 o'clock ceased its operation in the year 2016, experiment PHOBOS located at 10 o'clock in the year 2005 and experiment BRAHMS located at 2 o'clock stopped their operation in the year 2006 [32].

Before injection into RHIC, particles must be pre-accelerated, this is done in several steps:

1. For ions a so called Electron Beam Ion Source (EBIS) (2 MeV/nucleon in the case of Au) and for protons a 200 MeV Linear accelerator (Linac) is used,

2. Booster synchrotron – 100 MeV/nucleon in the case of Au,

3. Alternating Gradient Synchrotron (AGS) – 8,86 GeV/nucleon in the case of Au.

RHIC is able to accelerate and collide many types of ions e.g. p+p, d+Au, He3+Au, Cu+Cu, Cu+Au, Au+Au, U+U [34]. Gold can be collided at the center-of-mass energy of $9.2-200$ GeV per nucleon pair at $85 \cdot 10^{28}$ cm^{-2}s^{-1} luminosity (year 2015). RHIC's special feature is that it can collide polarized protons. In the year 2013, RHIC reached up to 52 % p+p polarization at 500 GeV and $160 \cdot 10^{30}$ cm^{-2}s^{-1} luminosity. The ability to collide polarized systems is essential for the current and future research of the proton spin. Basic information about the RHIC accelerator are in Table 3.1 and a photograph of the complex with marked individual pre-accelerators is shown in Figure 3.1.

3.3   RHICs run 2017–2018

For the year 2017 (Run17), STAR collaboration proposed 13 weeks of transverse polarised p+p at 500 GeV and one week p+p at 500 GeV. Also 2 weeks is designated to Coherent electron Cooling (CeC), as a novel form of electron cooling. This test is a part of preparation for the future eRHIC era. Remaining 4 weeks are designated to Au+Au at 62.4 GeV [35].

The year 2018 (Run18) is designated to isobaric nuclei measurements, 3.5 weeks of Ru+Ru at 200 GeV and 3.5 weeks of Zr+Zr at 200 GeV in order to understand the phenomenon of chiral magnetic effects [36]. Run will be ended by 2 weeks of Au+Au at 27 GeV [35] as a part of critical point study. In 2019–2020 as a part of Beam Energy Scan II (BES-II) collision energies 7.7, 9.1, 11.5, 14.5 and 19.6 GeV will be measured in order of searching for critical point [37].

It is worth mentioning that a new collaboration RHICf [38](RHIC forward) was created. It will use a calorimeter build for future The Compressed Baryonic Matter (CBM) experiment at Facility for Antiproton and Ion Research (FAIR). Calorimeter was installed at forward STAR region and will use STARs DAQ (Data acquisition). The main physics program is to study single spin asymmetry and cross section particles in the forward direction in order to constrain cosmic-ray shower models. Measurement will be taken during year 2017 .
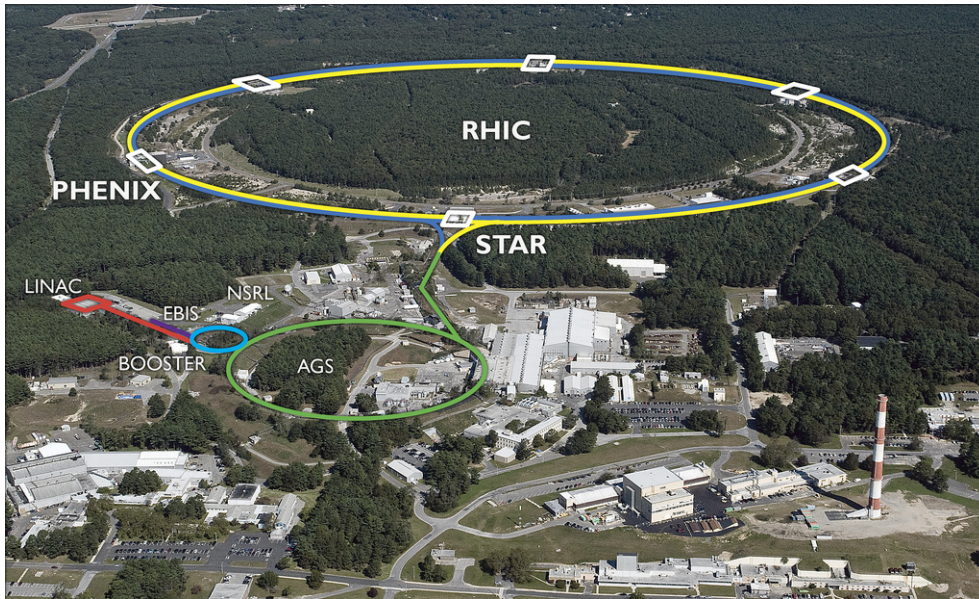
Figure 3.1: Photograph of the RHIC facility with marked individual pre-accelerators. One RHIC ring is labeled yellow other one blue. Taken from Ref. [39].

Circumference	3833.845 m
No. of interaction points	6
No. of dipole magnets	396
No. of quadrupole magnets	492
Dip. mag. magn. field @ 100GeV/n Au	3.458 T
Dip. mag. current	5.093 kA
Operation temperature (Helium coolant)	< 4.6 K
Cooling power at 4 K	24.8 kW
Time needed to cooling the system from 50 K	0.5 week
Au operating lifetime	10 h
No. of bunch/ring	111
No. of ions/bunch	$1.6 \cdot 10^9$
Beam energy	560 kJ
Kinetic energy (each beam): p	$31.2 - 250$ GeV
Kinetic energy (each beam): Au	$4.6 - 100$ GeV/N
Average luminosity, Au @ 100 GeV/N	$50 \cdot 10^{26}$ cm^{-2}s^{-1}

Table 3.1: Basic informations about the RHIC accelerator. Taken from Ref. [31,34, 40].

3.4   STAR Detector

The main barrel of the STAR detector (Solenoidal Tracker At RHIC) consists of several central mid-rapidity sub-detectors [41]. Detectors used in this analysis from outside to the center:

- Muon Telescope Detector – MTD,

- Barrel Electromagnetic Calorimeter – BEMC,

- Time of Flight – TOF,

- Time Projection Chamber – TPC,

- Silicon Strip Detector – SSD,

- Intermediate Silicon Tracker – IST,

- Pixel detector – PXL.

The last 3 named are part of a unit called (Heavy Flavor Tracker – HFT), which was used to measurements in years 2014 – 2016. STAR detector is shown in the Figure 3.2.
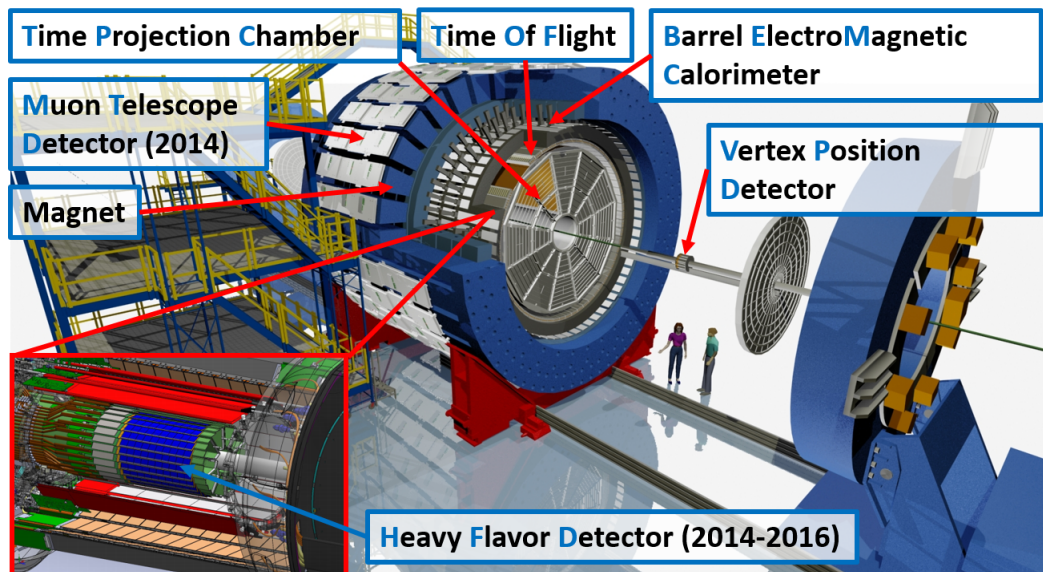
Figure 3.2: STAR detector with sub-detectors.

3.4.1   Muon Telescope Detector

Muon Telescope Detector (MTD) is located on the outer side of the STAR magnet, 400 cm far from interaction point. Muons traverse easily through STAR magnet unlike other particles thus we can exploit this property to identify muons from other particles, and measure Υ and J/ψ mesons trough di-muon decays. Basic specifications are in Table 3.2.

Azimuthal coverage	45 %
Pseudorapidity coverage	$|\eta| \leq 0.5$
Time resolution	≤ 100 ps
Spartial resolution	~ 1 cm
Number of channels	2808

Table 3.2: Specification of the STAR MTD. Taken from Ref. [42, 43].

3.4.2 Barrel Electromagnetic Calorimeter

Barrel Electromagnetic Calorimeter (BEMC) is located on the inner side of the magnet at 220 cm. The calorimeter includes Barrel Shower Maximum detector (BSMD) is used for measuring γ from π^0 decay. Its other purposes are e.g. direct γ and electrons identification and jets. It is divided into towers and each tower consists of scintillation and lead layers. Basic specification are in Table 3.3.

Inner radius	≈ 220 cm
Length	586 cm
Pseudorapidity coverage	$|\eta| \leq 1$
Number of towers	4800
Scintillation layers per tower	19×5 mm
	2×6 mm
Lead layers per tower	20×5 mm

Table 3.3: Specification of the STAR BEMC. Taken from Ref. [44].

3.4.3 Time of Flight

The Time of Flight (TOF) detector is located between the calorimeter and Time projection Chamber covering full azimuth and pseudorapidity $\eta \leq 1$ [45]. It consists of 120 Multigap Resistive Plate Chambers (MRPC)–glass plates with gas for proportional amplification. TOF is used for the measurement of the time of flight of particles Δt, while the initial time is taken from VPD (Vertex Position Detector). The Time Projection Chamber (TPC) provides the particle momentum and flight path Δs. Together with these three pieces of information, one can identify the particles using following equations

$$\frac{1}{\beta} = c\frac{\Delta t}{\Delta s} \tag{3.1}$$

and

$$m = \frac{p}{c}\sqrt{\left(\frac{1}{\beta}\right)^2 - 1}. \tag{3.2}$$

TOF can precisely identify particles with low momenta, thus improve the TPC identification precision. Inverse velocity $1/\beta$ as function of transverse momentum p_T is shown in Figure 3.3. A slice through the histogram is shown for the momenta of $1.2 < p_T < 1.4$ GeV/c.
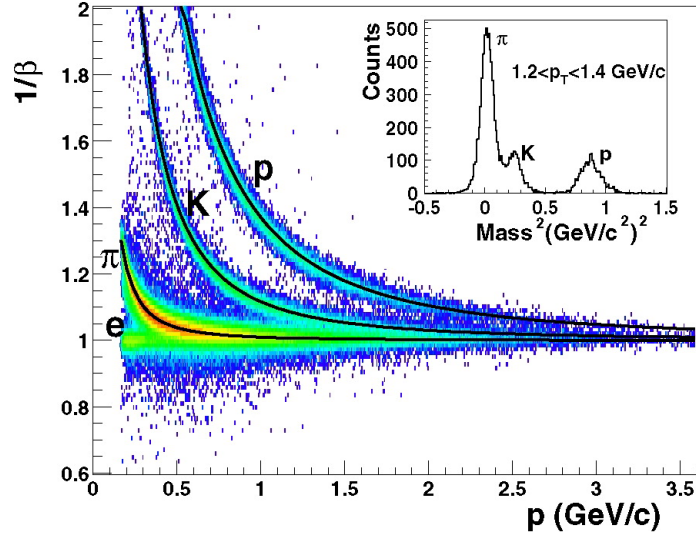
Figure 3.3: Inverse velocity $\frac{1}{\beta}$ for pions π, kaons K and protons p as function of transverse momentum p_{T} in STAR TOF for d+Au at 200 GeV with projection in range $1,2 < p_T < 1,4$ GeV/c with distinguishable particles. Taken from Ref. [46].

3.4.4 Time Projection Chamber

The Time Projection Chamber (TPC) is located between the Heavy Flavor Tracker and the TOF detector. The TPC is the main tracking device used for measurements of trajectories, particles momenta and for particle identification (PID) via ionizing energy loss $\langle \mathrm{d}E/\mathrm{d}x \rangle$. TPC covers the whole azimuth and pseudorapidity $|\eta| \leq 1.8$ [47]. The TPC is a barrel shaped with the outer diameter of 4 m and is 4.2 m long filled with the, so called, P10 gas (90% Argon for multiplication and 10 % Methane for quenching of positively-charged ions). The barrel is divided into 2 parts, the middle membrane is connected to an electric potential of -28 kV and the base is grounded. The area between the membrane and the base is divided into 182 rings, where one ring is common for both halves and carries the membrane. Rings are bridged by 2MΩ resistors providing uniform electric field between the membrane and the base. The scheme of the TPC in shown in Figure 3.4.

A charged particle traversing through the TPC creates electron–ion pairs. The emitted electrons are drifted towards the TPC sides where they are collected. The barrel base is divided into 12 sectors on the basis of Multi-Wire Proportional Chambers (MWPC). Each wire-anode is 20 μm in diameter and provides charge amplification by a factor of 1000–3000. Each sector is divided into 2 halves — inner and outer sector — each with a different number of collecting pads.

In the year 2019, the TPC will be improved to iTPC. The TPC transition to the iTPC [48] doubles the number of collecting pads and front end electronics in the inner sector which improves trajectory reconstruction in pseudorapidity $1 < \eta < 1.8$, enhances the efficiency up to 95 % and improves the measurement of the particle momentum and the energy loss $\langle \mathrm{d}E/\mathrm{d}x \rangle$. By improving the energy loss measurement, one can better distinguish between kaons and protons in the high momentum region [48]. Basic specifications of STAR TPC are in Table 3.4.
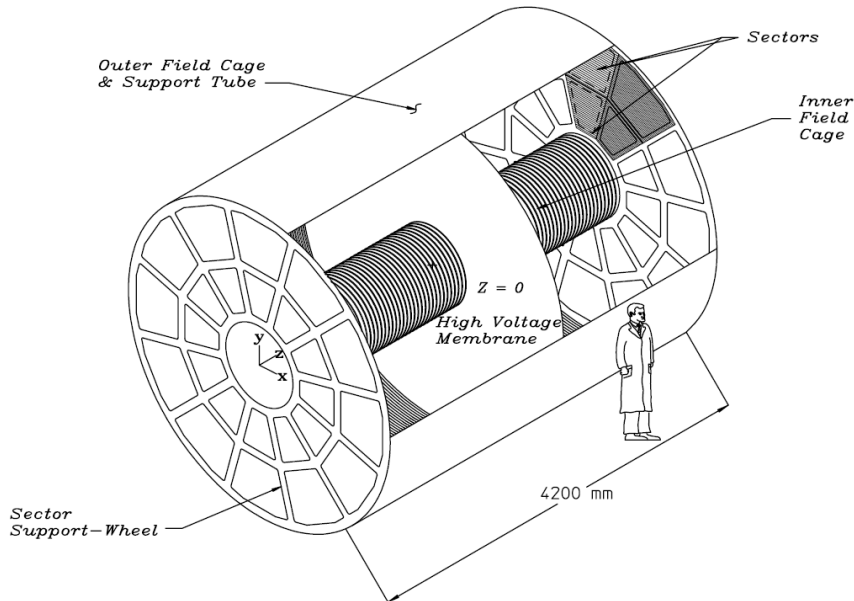
Figure 3.4: Scheme of the STAR TPC. The barrel is divided into two parts by the central membrane (High Voltage Membrane) which is under the potential of -28 kV. The area between the membrane and the base is divided into 182 rings, providing uniform electric field between the membrane and the base. The base is divided into 12 segments used for charge collection. Each segment is divided into inner and outer sectors. Taken from Ref. [47].

Charged particles (deuteron, proton, kaon, pion, muon, electron etc.) are identified via ionizing energy loss which obeys the Bethe-Bloch formula [49]

$$-\left\langle \frac{dE}{dx} \right\rangle = 2\pi N_A r_e^2 m_e c^2 \frac{Z}{A} \frac{z^2}{\beta^2} \left[\ln \frac{2m_e c^2 \beta^2 \gamma^2 W_{max}}{I^2} - 2\beta^2 - \delta(\beta\gamma) \right], \qquad (3.3)$$

where N_A is the Avogadro constant, r_e classical electron radius, m_e electron mass, c speed of light, Z medium atomic number, A medium mass number, z charge of the interacting particle, $\beta = \frac{v}{c}$, where v is the speed of the interacting particle, γ Lorentz factor, I average ionizing energy, δ density correction and W_{max} maximum energy transfer in a single collision.

Energy loss as a function of transverse momentum p_T in STAR TPC is shown in Figure 3.5.

3.4.5 Heavy Flavor Tracker

The inner-most detector of STAR is the Heavy Flavor Tracker (HFT) which is barrel-shaped and consists of 4 layers of silicon detectors. The outermost layer of the HFT is the Silicon Strip Detector (SSD), in the middle Intermediate Silicon Tracker (IST) and the inner-most 2 layers of Pixel detectors (PXL). These detectors improve the tracking and momentum resolution of STAR and are used for more precise measurement of decay vertices. Particle vertex is calculated by fitting hits

Outer radius	200 cm
Inner radius	50 cm
Length	420 cm
Pseudorapidity coverage	$|\eta| \leq 1.8$
Working gas	P10 (10 % methan + 90 % Argon)
Pressure	atmospheric + 2 mbar
Number of channels	136608
Magnetic field	0.5 T

Table 3.4: Specification of the STAR TPC. Taken from Ref. [47].
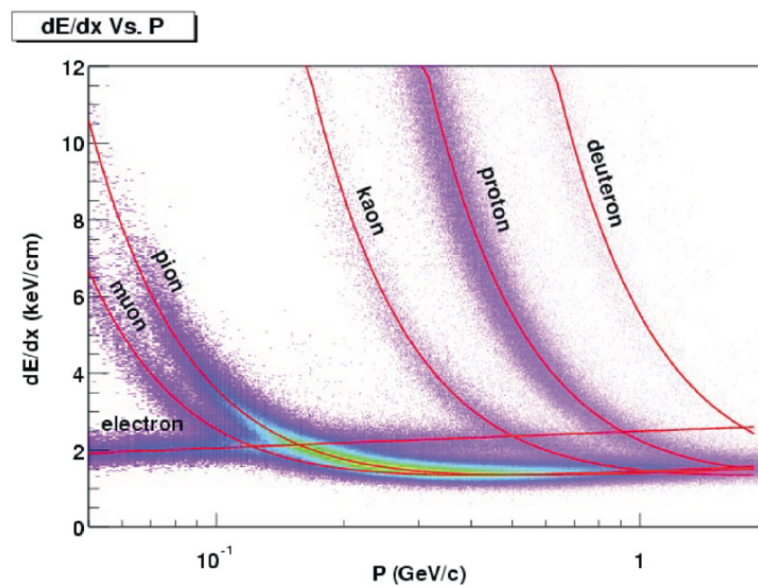
Figure 3.5: Energy loss as a function od transverse momentum p_T with magnetic field 0.25 T. Taken from Ref. [47].

in detector layers therefore hits closer to vertex greatly enhance fitting resolution. HFT was installed in 2014 and discontinued in 2016. HFT+, a faster successor which enables bottom quark measurement, is being prepared and will be ready for runs 2021-2022.

Silicon Strip Detector

Silicon Strip Detector (SSD) is the outermost layer of the HFT, it is barrel-shaped with 22 cm in radius and 106 cm in length, a photograph of the SSD can be seen in Figure 3.6. The barrel is divided into 20 triangle cross-sectional ladders carrying 16 double sided strip modules each. Each strip module is 75×42 mm^2 carrying 768 strips of width 95 μm on each side. The Strips have a stereoscopic angle of 2°, the total number of channels is 491520. The ladders are air-cooled [50]. Basic specification of the STAR HFT SSD are in Table 3.4.5.

Figure 3.6: The SSD team during detector installation. Taken from Ref. [51].

Radius	22 cm
Length	106 cm
Pseudorapidity coverage	$|\eta| \leq 1.2$
Module size	75×42 mm^2
Strip size	73×95 μm^2
R-Φ, Z resolution	740×20 μm^2
Number of channels	4915202

Table 3.5: Specification of the STAR SSD. Taken from Ref. [50].

Intermediate Silicon Tracker

Intermediate Silicon Tracker (IST) makes the second outermost layer of the HFT [50], it is barrel-like with 14 cm in radius and 50 cm in length. Sensors are divided into 24 hybrids (ladders). Each ladder is carrying 6 sensors 76.9×40 mm^2 in size and is divided into 6 chips. Each chip is a strip array of 2 columns and 64 rows, the size of each strip is 6275×596 μm^2. There is a total 110592 strips on 144 sensors, in comparison to SSD strips, they are only one–sided. IST covers the pseudorapidity of $-1.2 < \eta < 1.2$ and is cooled by Novec 7200[1] liquid. Photograph of the IST is in the Figure 3.7. Basic specification of STAR IST are in Table 3.4.5.

---

[1]Novec 7200 during leakage evaporates quickly, does not damage the ozone layer and its vapours are non-flammable and non-toxic.
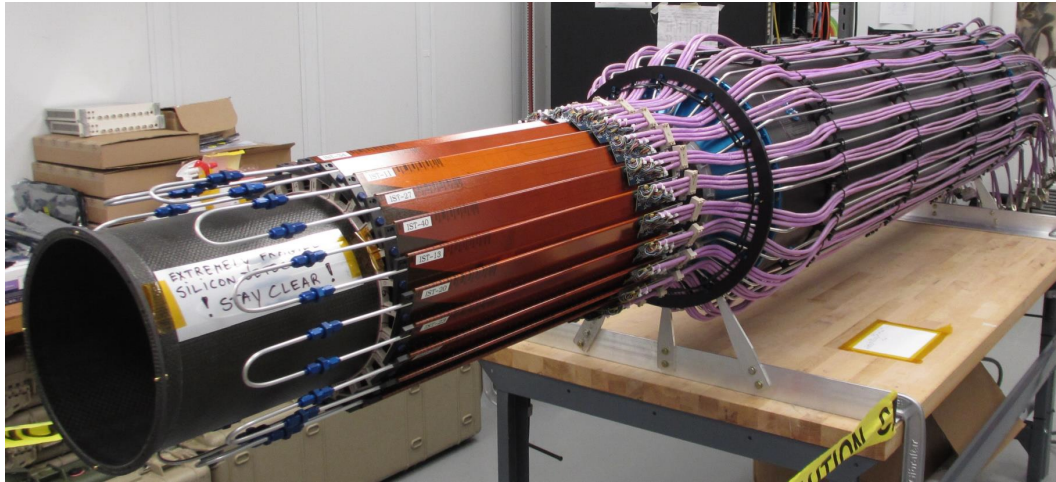
Figure 3.7: The IST structure. The ladders are brown, cooling loops on the one side and readout cables on the other side. Taken from Ref. [51].

Radius	14 cm
Length	50 cm
Pseudorapidity coverage	$|\eta| \leq 1.2$
Sensor size	76.9×40 mm^2
Strip size	6275×594 μm^2
R-Φ, Z resolution	1811×172 μm^2
Number of channels	110592
Readout time	185.6 μs

Table 3.6: Specification of the STAR IST. Taken from Ref. [50, 51].

Pixel detectors

Pixel detectors are the two innermost layers of the HFT [50], they are barrel-like with the radii of 2.8 cm and 8 cm. Both layers are attached to a common injection mechanism. The injection mechanism is divided into 10 sectors, each carrying 3 outer pixel ladders and 1 inner pixel ladder. Each ladder has 10 CMOS MAPS sensors of the size 2×2 cm^2. Each sensor is an 960×928 pixel array, with the pixel size of 20.7 μm and thickness of 50 μm. A total of 356M pixels is distributed among 400 sensors in 40 ladders. The pixel detector is cooled by air. Due to the proximity to the primary vertex, the sensors must be radiation resilient, because the ionizing environment is $20 - 90$ kRad/year and non-ionizing environment $2 \cdot 10^{11} - 10^{12}$ 1 MeV n eq/cm^2. Thanks to an innovative mechanical injection mechanism, the whole pixel detector can be replaced in one day. Basic specifications of the HFT PXL are in Table 3.4.5.

Figure 3.8: Structure of the Pixel detector. The sectors are grey and are carrying ladders with detectors, the readout cables are on the far side. Taken from Ref. [51].

Radius	2.8 and 8 cm
Pixel size	$20.7 \times 20.7 \ \mu m^2$
Resolution	$< 25 \ \mu m$
Number of channels	365 M
Readout time	185.6 μs

Table 3.7: Specification of the HFT PXL. Taken from Ref. [50,51].

3.5 Importance of the HFT

Heavy-quarks measurements are crucial for the heavy ion physics program at RHIC. The main motivation for the construction of the HFT was to expand the ability of the STAR detector to measure secondary vertices and directly identify particles containing heavy open flavor in p+p, p+A and A+A collisions.

The HFT opens new physics by the measurements of decay vertices by precise measurements of trajectories of the daughter particles, e.g.:

$$
\begin{aligned}
&D^0 \rightarrow K^- \pi^+, \ c\tau \sim 120 \ \mu m, \\
&D^\pm \rightarrow K^\mp \pi^\pm \pi^\pm, \ c\tau \sim 310 \ \mu m, \\
&D_s^\pm \rightarrow K^\mp K^\pm \pi^\pm, \ c\tau \sim 150 \ \mu m, \\
&\Lambda_c^+ \rightarrow pK^- \pi^+, \ c\tau \sim 60 \ \mu m, \\
&B \text{ mesons} \rightarrow J/\Psi X \text{ or } eX, \ c\tau \sim 500 \ \mu m,
\end{aligned}
\tag{3.4}
$$

where $c\tau$ is the decay length of a particle. The B-mesons can be studied via determination of the secondary vertex of single electrons or non-prompt J/Ψ. If we want to reconstruct the open-charmed hadrons, hadronic channels with p, K, and pi have to be used. Because these hadrons are abundant in heavy-ion collisions, these measurements have to deal with a sizable combinatorial background which can be reduced via topological cuts on the secondary vertices. As the lifetimes of the open-heavy-

flavor hadrons are extremely short, the HFT needs to have an excellent pointing resolution.

TPC itself has a resolution of 1 mm and each layer of HFT improves it, as can be seen in Figure 3.9. The HFT resolution for identified protons, kaons and pions can be seen in Figure 3.10. Figure 3.11 shows the D^0 invariant mass measurement. As can be seen in the smaller histogram, HFT can suppress the combinatorial background by 4 orders of magnitude.
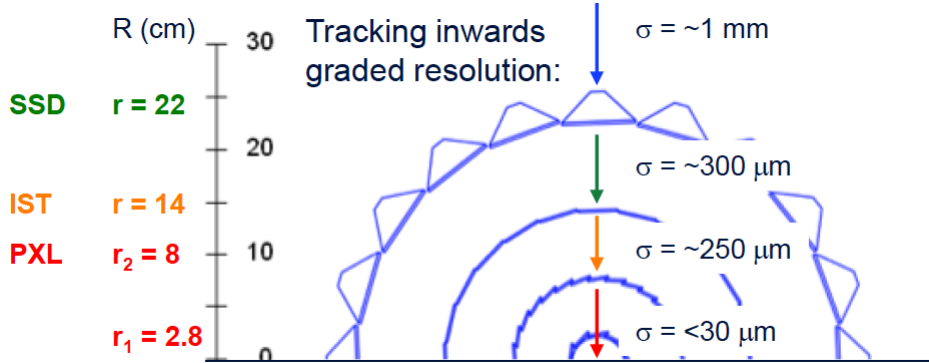
Figure 3.9: Resolution for each HFT layer. Taken from Ref. [51].
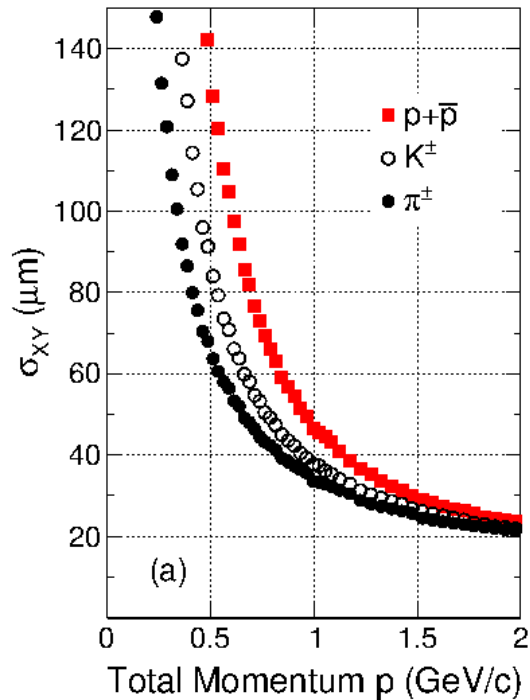
Figure 3.10: Pointing resolution in the transverse plane for p, K and π as a function of particle momentum p. Taken from Ref. [52].
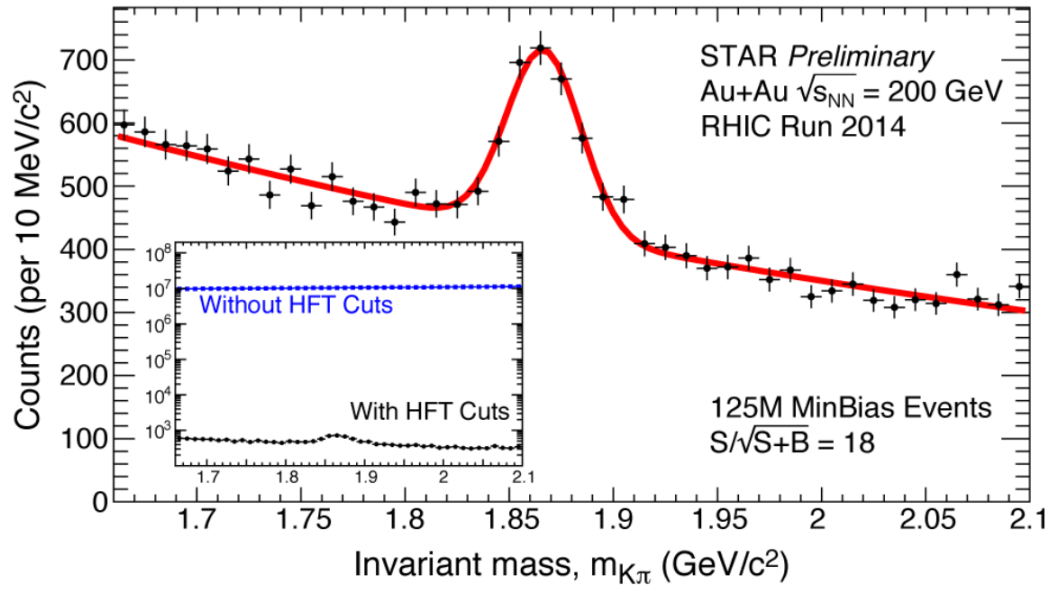
Figure 3.11: D^0 invariant mass for run 2014 Au+Au collisions at $\sqrt{s_{NN}} = 200$ GeV. The smaller histogram shows measurement without HFT cuts (blue points) and with HFT cuts (black points). Taken from Ref. [53].

Chapter 4

D meson reconstruction

This chapter is dedicated to the main research goal of this thesis – the $D^{\pm}$ meson reconstruction. In the year 2014, the STAR collaboration presented that the $D^{\pm}$ may be possible to measure [54]. Here, we aim to extract and correct the first measurement of $D^{\pm}$ p_T spectra and nuclear modification factor R_{AA}. The following section describes important selection criteria (cuts) that have been used, i.e. event and track selection, particle identification and topological cuts on the secondary vertex. Finally, raw yield mass distribution is shown and subtraction by the, so called, wrong–correct sign method is made.

The fundamental properties of $D^{\pm}$ are shown in Table 4.1. The D^+ meson consists of $c\bar{d}$ quark and D^- meson of $d\bar{c}$. In this work $D^{\pm}$, are reconstructed via the reconstruction of its decay products from the decay channel $D^{\pm} \rightarrow K^{\mp}\pi^{\pm}\pi^{\pm}$ with the branching ratio (B.R.) of 9.13 %. The $D^{\pm}$ meson decay with the mean decay length of $c\tau = 311.8$ μm, therefore the HFT is crucial in this type of reconstruction to distinguish the D^+ signal from the combinatorial background of K$\pi\pi$ triplet.

Mass	$m = (1869.61 \pm 0.1)$ MeV$/c^2$
Mean life time	$\tau = (1040 \pm 7) \times 10^{-15}$ s
Mean flight path	$c\tau = 311.8$ μm
Decay mode	$D^{\pm} \rightarrow K^{\mp}\pi^{\pm}\pi^{\pm}$ B.R 9.13%

Table 4.1: Important $D^{\pm}$ parameters. Taken from Ref. [55].

4.1 Reconstruction of $D^{\pm}$ mesons

4.1.1 Event selection criteria

The Au+Au $\sqrt{s_{NN}} = 200$ GeV minimum-bias data collected in the year 2014 was used in this analysis. Total $1.3 \cdot 10^9$ events were collected, after the trigger restrictions, cut on $|v_z| < 6$ cm and $|v_z(\text{VPD}) - v_z| < 3$ cm, 900M events were accepted for further analysis. v_z is the distance along beampipe from the detector center given by Time Projection Chamber (TPC) and $v_z(\text{VPD})$ is the distance along beampipe taken from Vertex Position Detector (VPD).

4.1.2 Track selection criteria

Each global track[1] must have hit in each layer of the HFT. That means in both pixel layers and in IST layer (SSD was not used in 2014). It is also required that the track generates at least 20 hits in TPC to ensure proper particle track fit. The track transverse momentum is required to be $p_T > 0.5$ GeV/c for both pions and kaons to lower combinatorial background of lower bins.

4.1.3 Particle identification criteria

Several Particle Identification (PID) cuts have been made.

TPC $n\sigma_X^{\mathrm{d}E/\mathrm{d}x}$ signal standard deviation for particle of kind X is defined [2] as

$$n\sigma_X^{\mathrm{d}E/\mathrm{d}x} = \frac{\ln \frac{\mathrm{d}E/\mathrm{d}x}{\langle \mathrm{d}E/\mathrm{d}x \rangle_X}}{R^{\mathrm{d}E/\mathrm{d}x}}, \tag{4.1}$$

where $\mathrm{d}E/\mathrm{d}x$ is the TPC ionization loss, $\langle \mathrm{d}E/\mathrm{d}x \rangle_X$ is the mean value of ionization loss given by the Bischel function and $R^{\mathrm{d}E/\mathrm{d}x}$ is the corresponding resolution. For pion the standard deviation must be $n\sigma_\pi < 3$ and for kaon $n\sigma_K < 3$.

The required TOF inverse pion velocity $|\frac{1}{\beta} - \frac{1}{\beta_\pi}| < 0.03$ and kaon $|\frac{1}{\beta} - \frac{1}{\beta_K}| < 0.03$, where $\frac{1}{\beta_X}$ is inverse velocity of track calculated from track momentum and tabular particle X mass and $\frac{1}{\beta}$ is inverse velocity of track measured by the TOF detector.

The standard deviation for pions and kaons with corresponding cuts can be seen in Figure 4.2 and the inverse velocity in Figure 4.3. Grow in left part of TPC/TOF kaon distribution is the parasitic contribution of pions.

4.1.4 Topological reconstruction

At this point, in each event we look for D$^\pm$ candidates, thus topological cuts in vertex reconstruction are applied. The distance of closest approach (DCA) between the daughter pair tracks ($\pi\pi$, πK, Kπ) must be smaller than 80 μm. The distance of reconstructed secondary vertex[2] from the primary vertex (in other words, reconstructed D$^\pm$ mean decay length) must be greater than 30 μm and smaller than 2000 μm. The lower limit is taken from the PXL minimum resolution to distinguish the primary from the secondary vertices. The pointing angle $\cos(\theta)$ must be greater than 0.996. The pointing angle is the deviation between the reconstructed momentum direction of the K$^\mp\pi^\pm\pi^\pm$ triplet and line connecting primary and secondary vertex. The variables, used in the topological reconstruction, are shown in Figure 4.1.

---

[1]All tracks reconstructed by TPC regardless of the origin, i.e. tracks from the primary and decay vertices, are called global tracks. Primary tracks are the tracks, that originate in the primary vertex, i.e. not tracks from secondary decays. This distinction has been made to improve the track reconstruction as the primary vertex can be used in the tracking for the primary tracks. However, the global tracks are used in this analysis.

[2]The secondary vertex is calculated by following way: A straight line approximation for the particle helix is used. DCA's from the first track to the second one and from the second to the first track are calculated. This is also done between the third track. All 6 vectors are added together and divided by 6.
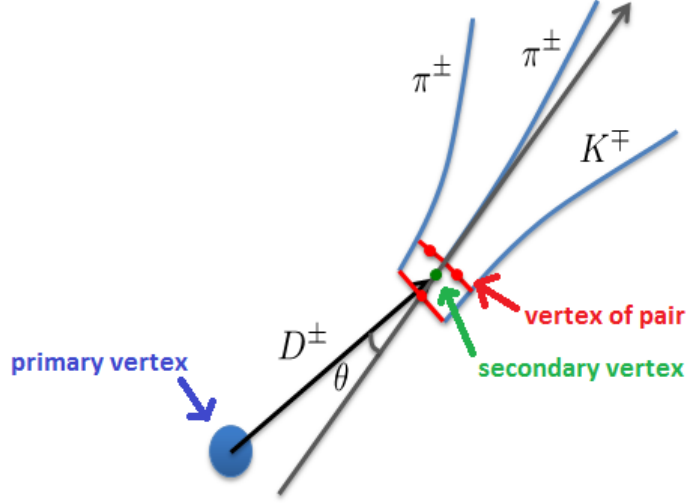
Figure 4.1: The $D^{\pm}$ pointing angle. Its the deviation of the reconstructed momentum vector and line connecting primary and secondary vertex.

Another cut on $\Delta_{max} < 200$ μm is used. Δ_{max} is the maximum distance between $v_{\pi\pi}$, $v_{\pi K}$ and $v_{K\pi}$, where $v_{\pi K}$ is the reconstructed pair vertex[3] of π and K track etc. The daughter DCA to primary vertex must be greater than 100 μm for pions and 80 μm for kaons to be certain they do not originate from the primary vertex, the total of 30M candidate triplets passed the selection criteria. Candidate triplets separated by charge combination can be seen in Table 4.2. That means the first bin represent the D^+, second bin D^- and the rest are different wrong charge combinations used as wrong-sign background.

$K^-\pi^+\pi^+(D^+)$	$K^+\pi^-\pi^-(D^-)$	$K^-\pi^+\pi^-$ $K^-\pi^-\pi^+$	$K^+\pi^+\pi^-$ $K^+\pi^-\pi^+$	$K^-\pi^-\pi^-$	$K^+\pi^+\pi^+$
$3.68{\cdot}10^6$	$3.71{\cdot}10^6$	$7.26{\cdot}10^6$	$7.46{\cdot}10^6$	$3.57{\cdot}10^6$	$3.74{\cdot}10^6$

Table 4.2: The number of $D^{\pm}$ triplets charge combination candidates. The first bin represents the D^+, second bin D^- and the rest are different wrong charge combinations used as wrong sign–correct sign background.

All used cuts are summarized in the Table 4.3. Distribution of $D^{\pm}$ decay length and Δ_{max} of candidate tracks can be seen in Figure 4.4. Track DCA to primary vertex and transverse momentum p_{T} distribution for π and K with track and PID cuts can be seen in Figure 4.5 and 4.6. The DCA cut is important to remove particle contribution from the primary vertex as they cannot originate from D–meson decay. As can be seen further improvement can be done by lowering the momentum cut to get more candidates, however this step is redeemed by computing time.

---

[3]A straight line approximation for the particle helix is used. DCA's from the first track to the second one and from the second to the first track are calculated. Vectors are added together and divided by 2.

Event selection	Distance along beampipe	$|v_z| < 6$
	Deviation between VPD and distance	$|v_z(VPD) - v_z| < 3$
Track selection	Hits HFT	PXL1, PXL2, IST
	Hits in TPC	$N_{TPC} > 20$
Topological Cuts	DCA between $\pi\pi$, πK, $K\pi$	$DCA_{XY} < 80~\mu m$
	$D^{\pm}$ decay length	$30~\mu m < c\tau < 2000~\mu m$
	Pointing angle	$\cos\theta > 0.998$
	Max reconstructed vertex pair distance	$\Delta_{max} < 200~\mu m$
	Daughter DCA to primary vertex	$DCA_{\pi 0} > 100~\mu m$
		$DCA_{K0} > 80~\mu m$
Particle identification	TPC particle transverse momentum	$p_T^{\pi} > 0.5$ GeV/c
		$p_T^{K} > 0.5$ GeV/c
	TPC ionization loss standard deviation	$n\sigma_{\pi} < 3$
		$n\sigma_K < 2$
	TOF particle transverse momentum	$p_T^{\pi} > 0.5$ GeV/c
		$p_T^{K} > 0.5$ GeV/c
	TOF inverse velocity	$|\frac{1}{\beta} - \frac{1}{\beta_{\pi}}| < 0.03$
		$|\frac{1}{\beta} - \frac{1}{\beta_K}| < 0.03$

Table 4.3: Summary of used event selection, track selection, topological cuts and PID cuts.

4.2 Wrong-sign background and Yield

After applying cuts, invariant mass (mc^2) is constructed from conservation of four-momentum $(E, \vec{p}c)$ as $mc^2 = \sqrt{E^2 - \| \vec{p} \|^2 c^2}$, where E is particle energy and $\vec{p}$ particle momentum. An example of $D^{\pm}$ signal in 2 transverse momentum bins can be seen in Figure 4.7. The background has been created as wrong charge combination according to Table 4.2 and can be seen in Figure 4.7.

Candidates were divided by centrality and reconstructed $D^{\pm}$ transverse momentum p_T to several bins. The following corrections were made separately for each bin. The signal peak in Figure 4.7 was fitted with a Gaussian and 3σ wide invariant mass windows were used as a signal interval, i.e. $(1.795 - 1.945)$ GeV/c^2. Counts outside signal interval were counted and simultaneously, counts outside the same interval were counted in background, thus the scaling parameter has been estimated. The background was scaled and subtracted from signal+background, significant residual background remains so the following correction was applied: The signal has been fitted with a gaussian and a polynomial of the first order and the polynomial has been subtracted. The result can be seen in Figure 4.8. The yield and significance was calculated by bin counting method i.e. bins in signal were counted. The ranges for bin counting method has been tuned manually for each centrality and transverse momentum range. The peak significance has been evaluated as

$$\sigma = \frac{S}{\sigma_S}, \tag{4.2}$$

where S is the yield in signal window and σ_S is the yield uncertainty.
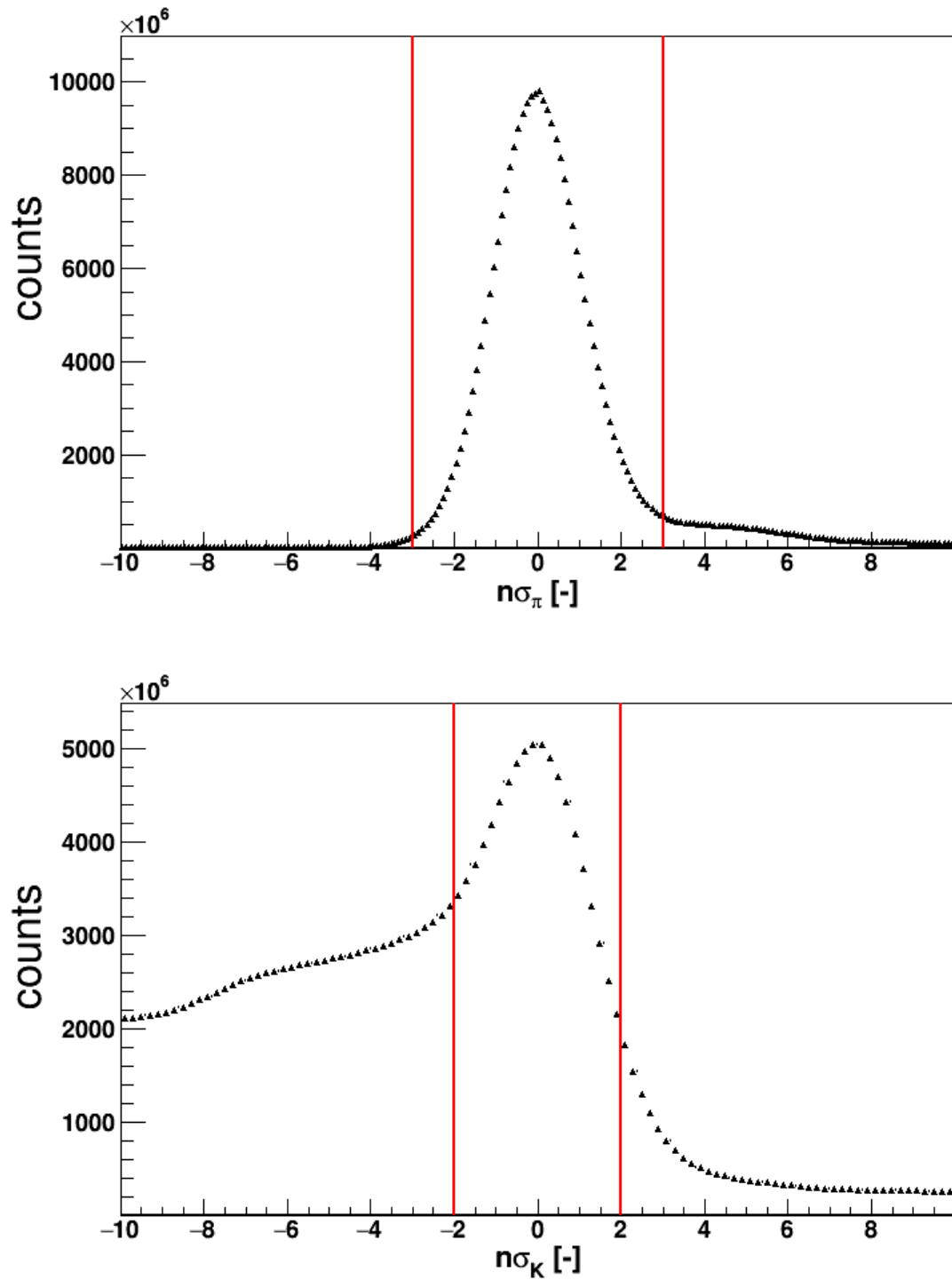
Figure 4.2: TPC $n\sigma$ distribution for π and K. Cuts are represented by red lines, tracks between this cuts are accepted.
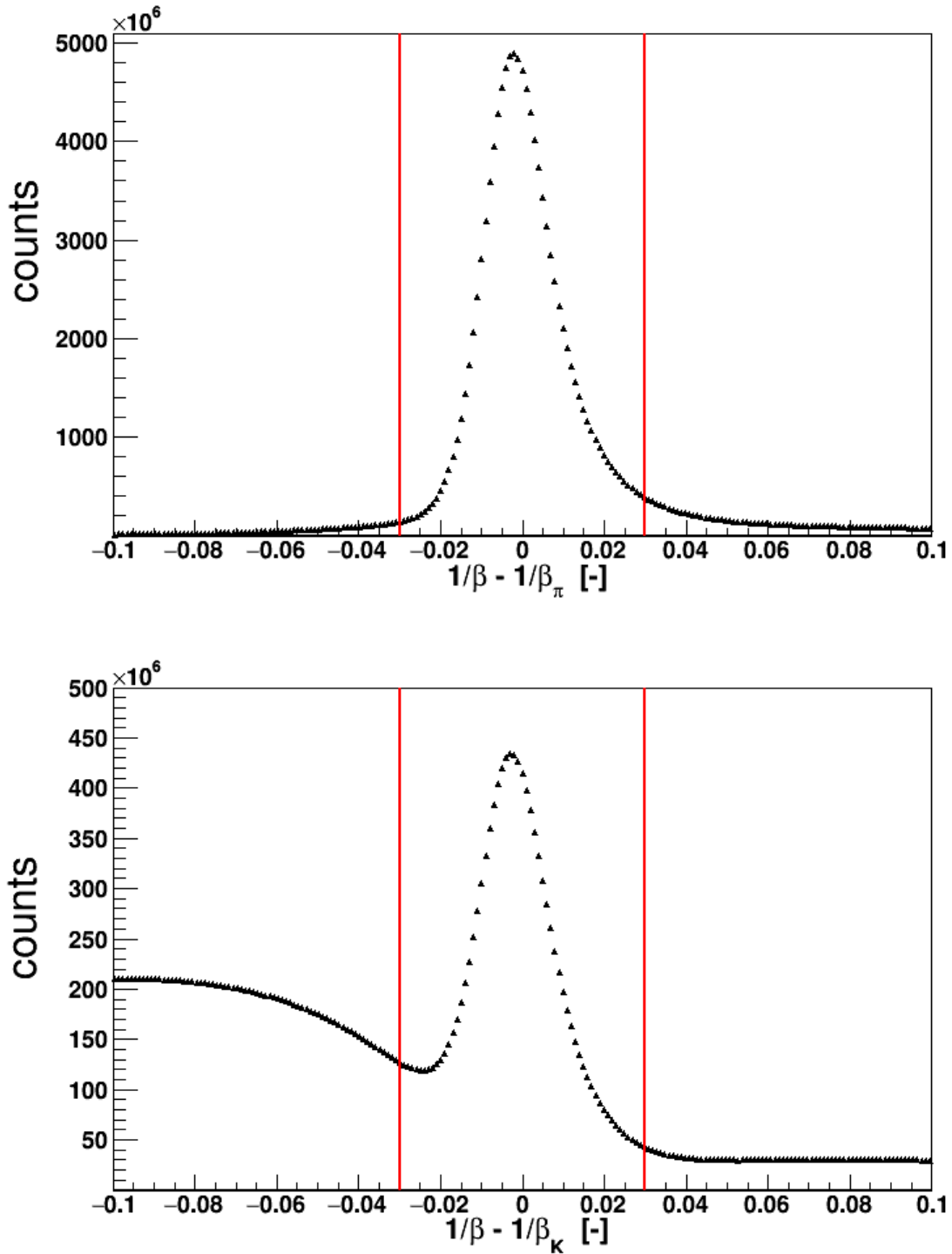
Figure 4.3: TOF $|\frac{1}{\beta} - \frac{1}{\beta_{\pi/K}}|$ distribution for π and K. Cuts are represented by red lines, tracks between this cuts are accepted.
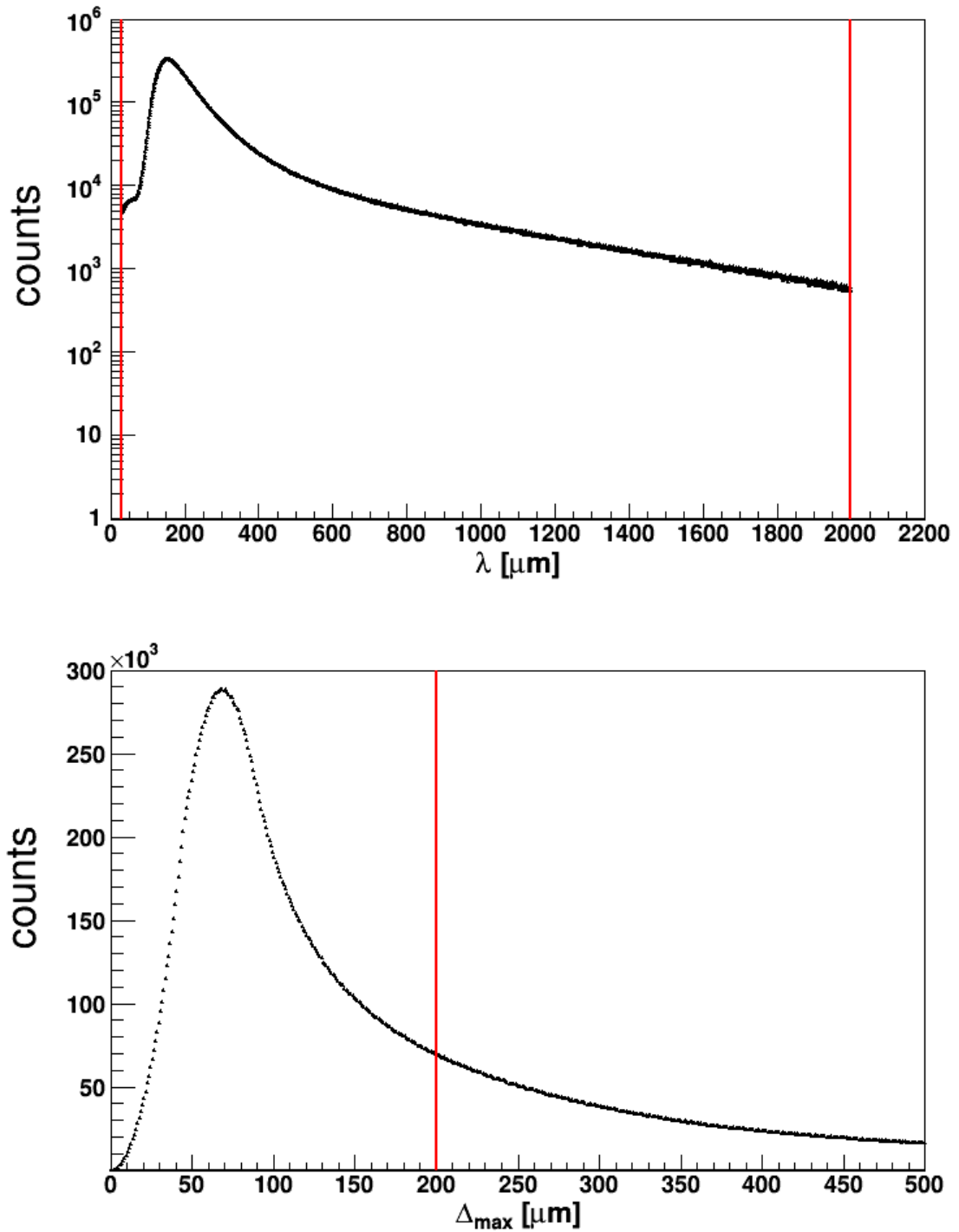
Figure 4.4: The D$^{\pm}$ decay length and Δ_{max} distribution. Cut is represented by red line, for the Δ_{max} candidates < 200 μm are accepted.
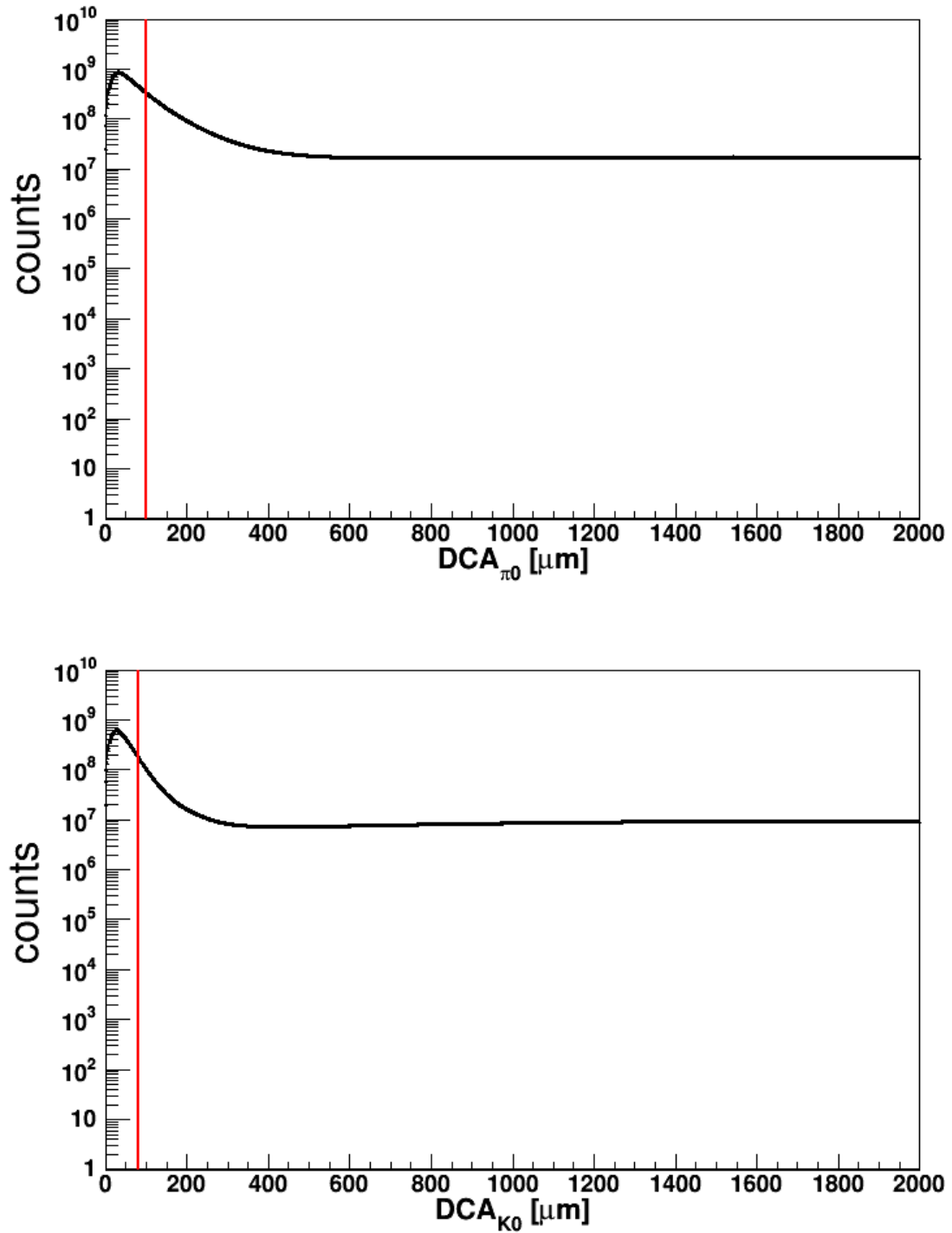
Figure 4.5: Tracks DCA to the primary vertex distributions for π and K. Cut is represented by red line, tracks above this cut are accepted.
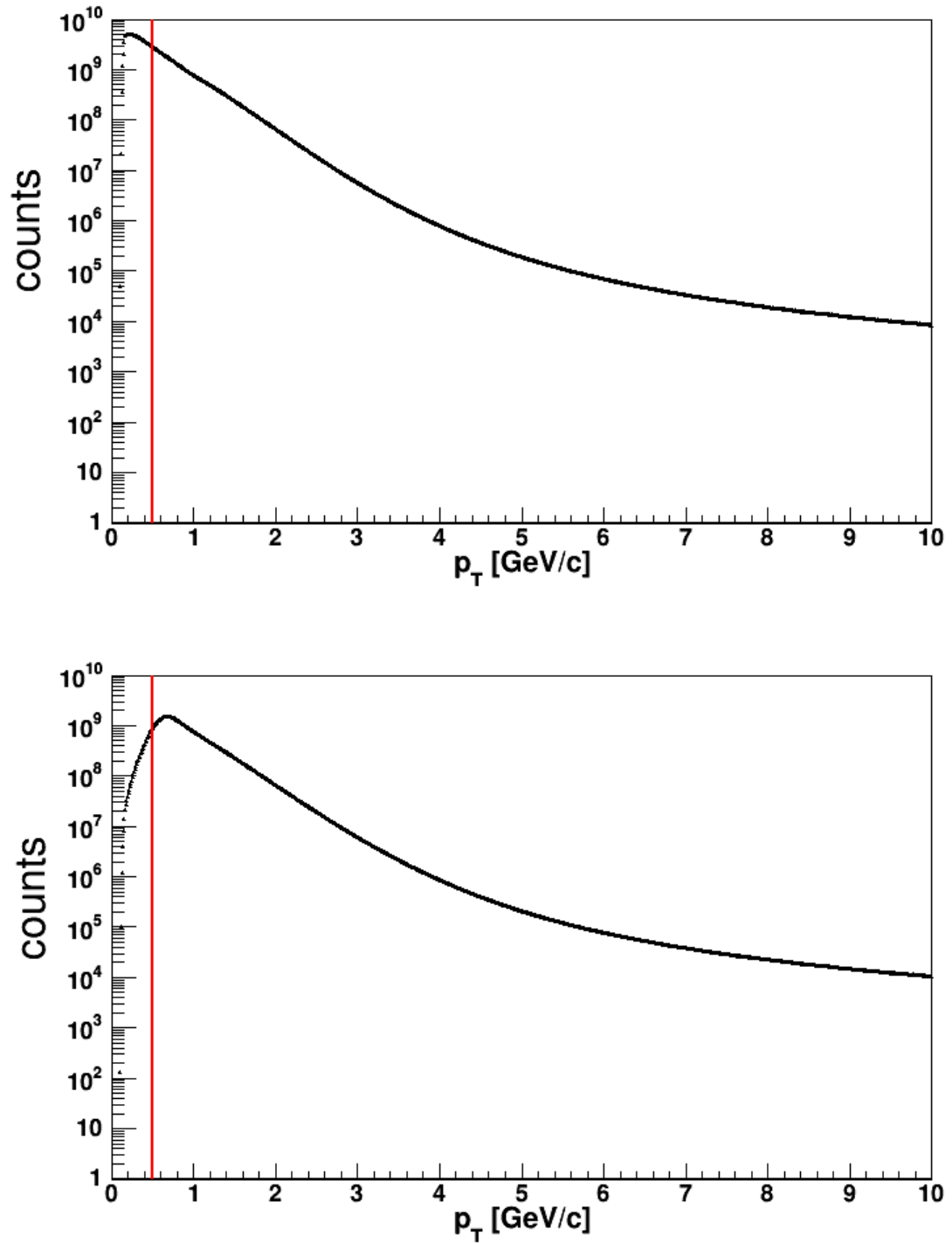
Figure 4.6: Tracks transverse momentum p_T distributions for π and K. Cut is represented by red line, tracks above this cut are accepted.

Yields with peak significance per transverse momentum p_T for different centralities can be found in Table 4.4. Yields with significance $\sigma < 3$ were rejected.

p_T [GeV/c]	0–10%		10–40%		40–80%		0–80%	
	Yield [−]	Sig.[−]	Yield [−]	Sig.[−]	Yield [−]	Sig.[−]	Yield [−]	Sig.[−]
$1.0 - 2.0$	263 ± 286	0.9	1176 ± 238	4.9	368 ± 41	8.4	1813 ± 375	4.8
$2.0 - 2.5$	580 ± 120	4.8	1675 ± 103	16.3	436 ± 26	17.0	2686 ± 160	16.8
$2.5 - 3.0$	757 ± 73	10.3	1672 ± 69	24.2	483 ± 24	20.0	2901 ± 104	28.0
$3.0 - 3.5$	471 ± 41	11.4	1216 ± 47	26.1	401 ± 21	19.2	2079 ± 66	31.6
$3.5 - 4.0$	273 ± 24	11.4	801 ± 33	24.3	261 ± 17	15.3	1327 ± 44	30.1
$4.0 - 4.5$	182 ± 17	10.0	465 ± 24	19.0	169 ± 14	12.5	809 ± 33	24.7
$4.5 - 5.0$	86 ± 11	7.7	294 ± 19	15.5	101 ± 11	8.9	470 ± 25	19.0
$5.0 - 5.5$	57 ± 10	5.9	178 ± 15	11.9	59 ± 8	7.1	288 ± 20	14.7
$5.5 - 6.0$	36 ± 6	5.6	99 ± 11	8.7	35 ± 6	5.5	163 ± 15	11.2
$6.0 - 7.0$	28 ± 7	4.2	103 ± 11	9.2	32 ± 6	5.3	157 ± 14	11.0
$7.0 - 8.0$	13 ± 3	3.7	38 ± 6	5.9	16 ± 4	0	57 ± 8	7.1
$8.0 - 10.0$	7 ± 3	2.6	21 ± 5	4.1	19 ± 4	0	35 ± 6	9.5

Table 4.4: Raw yield and peak significance per transverse momenta bin p_T per centrality bin.
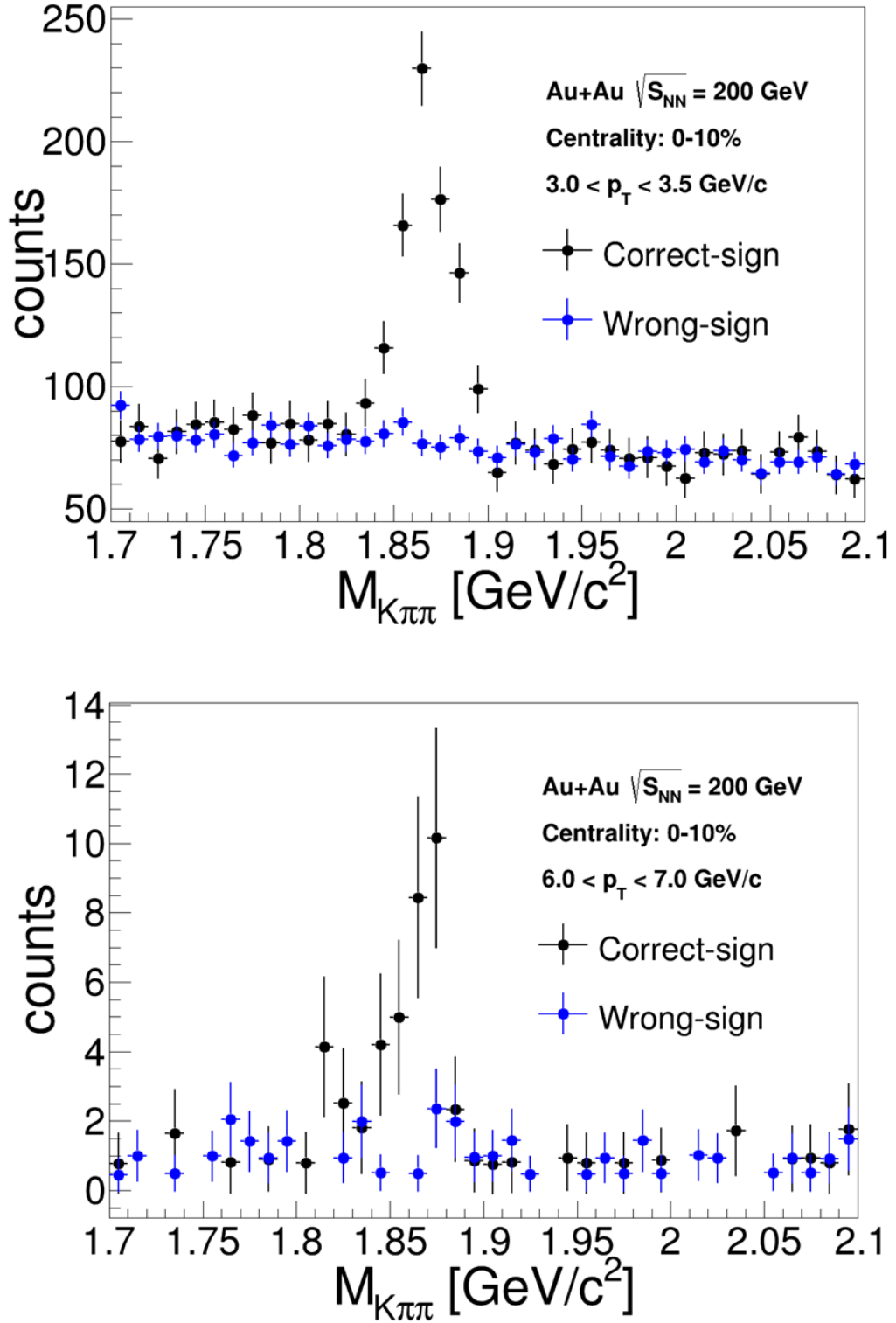
Figure 4.7: The D$^\pm$ signal+background for Au+Au $\sqrt{s_{\mathrm{NN}}} = 200$ GeV in centrality range 0–10% for 2 transverse momentum p_{T} bin.
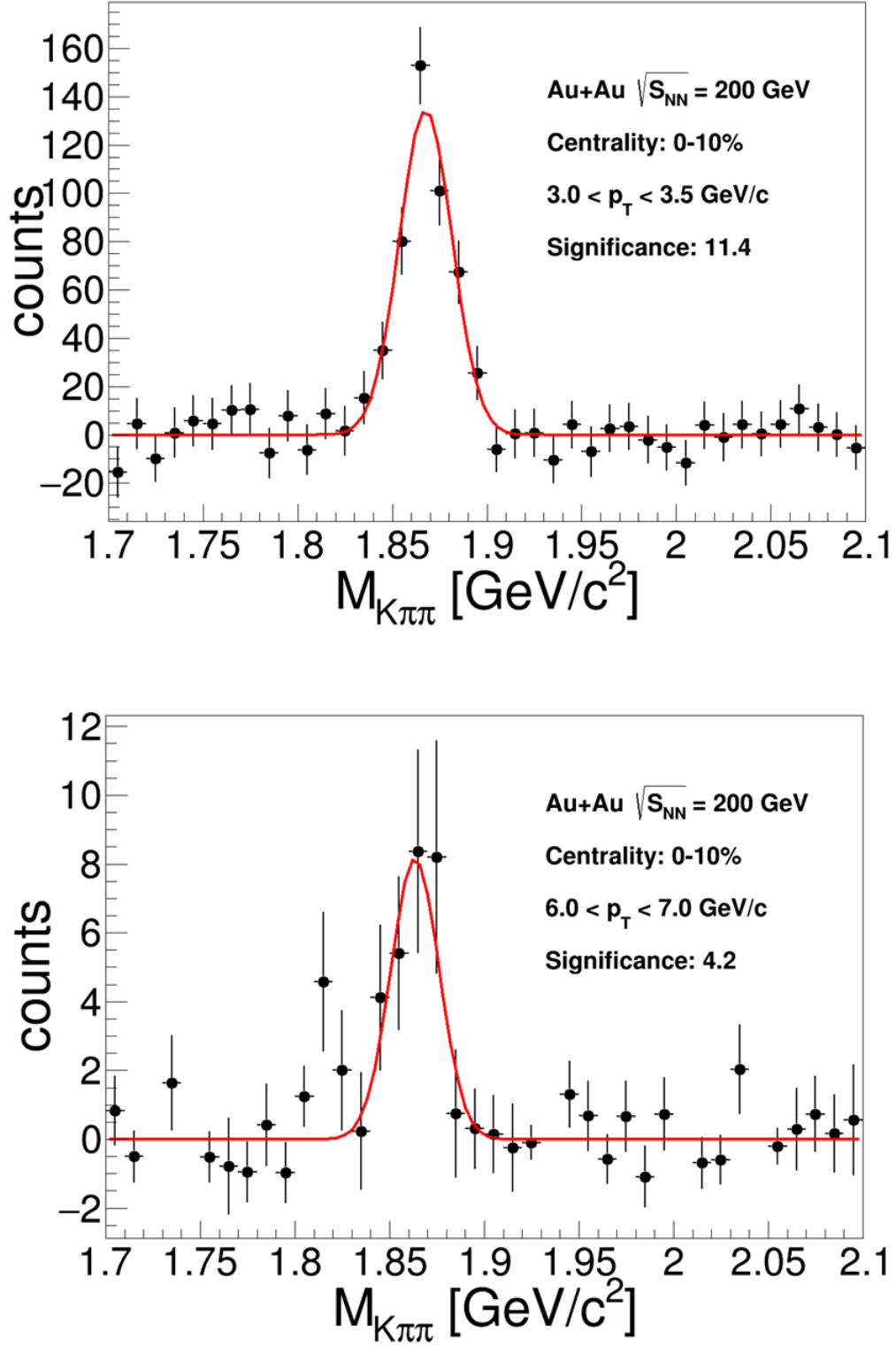
Figure 4.8: The D$^{\pm}$ signal after background subtraction in centrality range 0–10% for 2 transverse momentum p_{T} bin.

Chapter 5

Invariant yield

This chapter is dedicated to the raw spectra correction to obtain invariant yield and to the calculation of the systematic uncertainty. Finally, the invariant yield is compared to measurements of D^0 done in year 2010 and 2014.

5.1 Spectra corrections

The raw yield cannot be compared with any other measurements or experiments, since it is sensitive to cut selection and detector alignment which is experiment dependent and also varies in time. Hence, it needs to be corrected to obtain so called invariant yield using the following formula:

$$\frac{\mathrm{d}^2 N}{\mathrm{d}p_T \mathrm{d}y} \frac{1}{2\pi p_T} = \frac{Y_{uncorrected}}{2\pi \cdot N_{charge} \cdot N_{events} \cdot BR \cdot p_T \cdot \Delta p_T \cdot \Delta y \cdot Eff(p_T)}, \qquad (5.1)$$

where $Y_{uncorrected}$ uncorrected raw yield, $N_{charge} = 2$, N_{events} number of events, $BR = (9.13\pm0.19)\%$, Δp_T bin width, $\Delta y = 2$ rapidity width, $Eff(p_T)$ detector acceptance$\times$efficiency.

The uncorrected (raw) yield in Table 4.4 must be normalized in order to ensure measurement invariance. $N_{charge} = 2$ since we are studying 2 particles (D^+,D^-). Number of events per studied centrality can be found in Table 5.1.

centrality	N_{events}
0–10%	$102.8 \cdot 10^6$
10–40%	$320.1 \cdot 10^6$
40–80%	$435.4 \cdot 10^6$
0–80%	$858.3 \cdot 10^6$

Table 5.1: The N_{events} number of events per centrality.

5.1.1 Detector acceptance$\times$efficiency Eff($\mathbf{p_T}$)

One of the most important normalization factors is detector acceptance$\times$efficiency. It contains the geometrical acceptance and efficiency of STAR´s each single sub–

detectors (HFT,TPC,TOF) used in this measurement. Data-driven fast simulator has been developed for this purpose. Simulator requires three main inputs: centrality-dependent V_z distributions and ratio of HFT matched tracks to TPC tracks extracted from data and TPC efficiency and momentum resolution from embedding. This simulator has been validated with full GEANT simulation and its error is within 5%, this value has been included in systematical errors. The simulator provides centrality dependent efficiency for reconstructed D-meson, the centrality probability in realistic collision in not equally represented, thus to get the total efficiency a normalization for number of binary collisions N_{coll} must be done. Number of binary collisions is shown in Table 5.3 and for normalization following formula has been used

$$Eff(0-80\%, p_T) = \frac{N_{coll}(0-5\%) \cdot Eff(0-5\%, p_T)..N_{coll}(70-80\%) \cdot Eff(70-80\%, p_T)}{N_{coll}(0-5\%)..N_{coll}(70-80\%)}$$
(5.2)

As an initial approach acceptance×efficiency has been parametrized to soften the bin effect by a function with no physical meaning:

$$Eff(p_T) = Ae^{-\left(\frac{B}{x}\right)^C} e^{-\left(\frac{x-D}{E}\right)^2},$$
(5.3)

where A, B, C, D and E are real parameters. Normalized detector acceptance×efficiency for centrality 0–10%, 10–40%, 40–80% and 0–80% can be seen in Figure 5.1 and parametrization parameters in Table 5.2. The acceptance×efficiency statistical uncertainties and fit parameters uncertainties are not propagated further in this analysis. Instead, an overall systematic uncertainty 5 % (mentioned above) is used. Further study on parametrization function must be done by changing the function and/or improving simulation statistics.

centrality	A	B	C	D	E
0-10%	0.5 ± 0.2	14 ± 2	0.89 ± 0.06	-51 ± 18	37 ± 7
10-40%	4 ± 3	22 ± 6	0.76 ± 0.06	-58 ± 30	36 ± 10
40-80%	16 ± 12	93 ± 34	0.53 ± 0.04	-39 ± 22	27 ± 8
0-80%	2.1 ± 0.6	21 ± 2	0.76 ± 0.02	-55 ± 8	35 ± 3

Table 5.2: The D$^{\pm}$ detector acceptance×efficiency parametrization (5.3) parameters.

5.2 Invariant yield systematic uncertainty

The yield systematic uncertainty has been estimated by variating basic topological cuts. It is expected, that by changing the cuts the invariant yield should be same, thus the difference will be used as systematic uncertainty. Only one cut has been changed at the same time while the rest was fixed on its original value:

- Daughter p_T: 500 $\rightarrow$ 520 MeV

- Particles DCA to primary vertex:

    $DCA_{\pi 0} > 100 \rightarrow 90 \ \mu$m

    $DCA_{K0} > 80 \rightarrow 70 \ \mu$m

centrality	N_{coll} $[-]$
0–5%	1066.5 ± 27.8
5–10%	852.8 ± 23.7
10–20%	606.9 ± 30.6
20–30%	375.9 ± 33.4
30–40%	222.6 ± 30.3
40–50%	124.0 ± 24.6
50–60%	64.0 ± 17.8
60–70%	30.6 ± 11.4
70–80%	13.7 ± 6.2

Table 5.3: The N_{coll} number of binary collisions per centrality in run 2014.
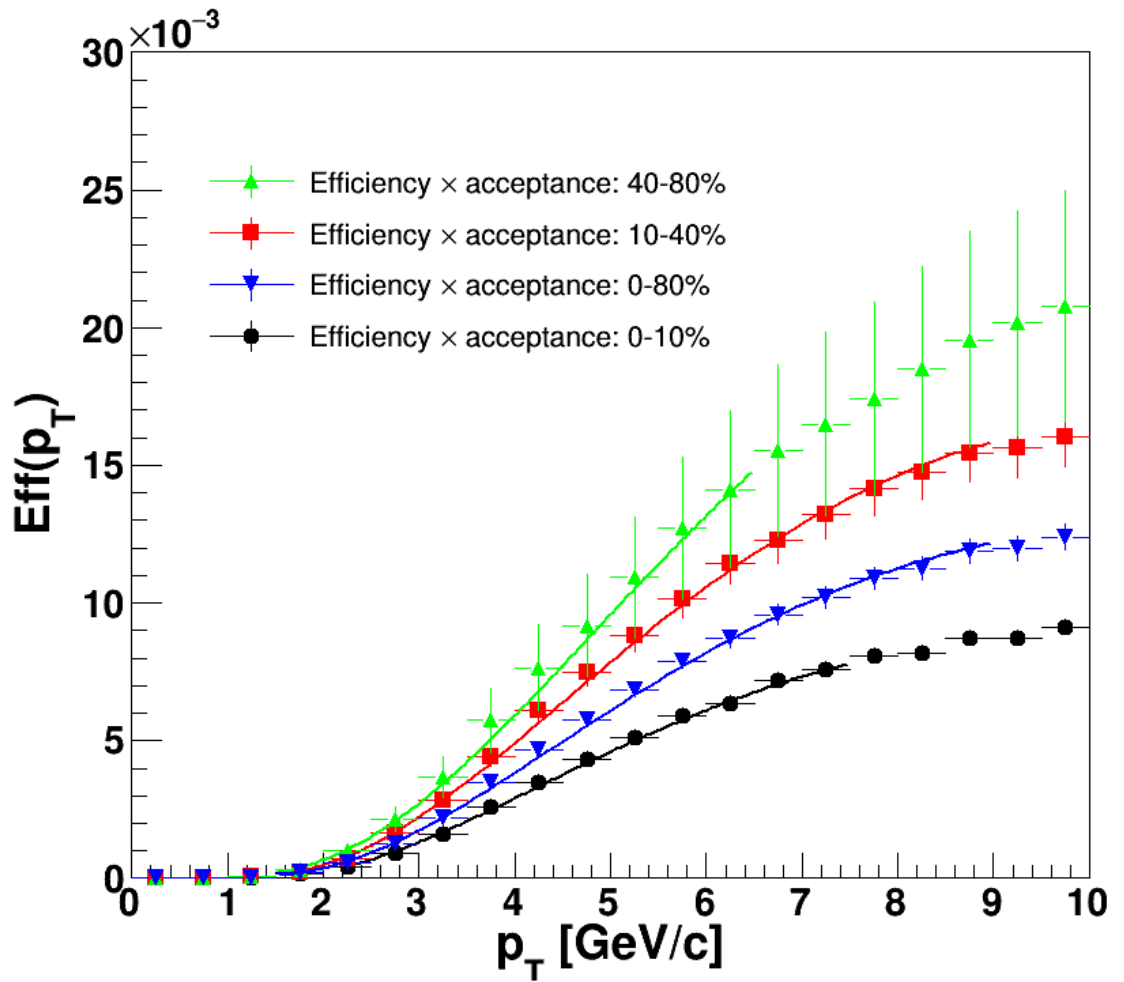
Figure 5.1: The $D^{\pm}$ detector acceptance×efficiency for different centralities.

- DCA between pairs $DCA_{XY} < 80 \rightarrow 90$ μm

- Max reconstructed vertex pair distance $\Delta_{max} < 200 \rightarrow 220$ μm

- Hits in TPC $N_{TPC} > 20 \rightarrow 15$

- Invariant mass binning $40 \rightarrow 50$

- Invariant mass fit stability (fit range change)

The total yield systematic error was calculated as

$$\sigma_{total} = \sqrt{\sum \sigma_{var}}, \tag{5.4}$$

where σ_{var} is the difference between base and variated cuts yields for each centrality and transverse momentum bin. I would like to mention that for each variation of the topological cuts appropriate acceptance$\times$efficiency was calculated. This means that the correlation between cuts is not taken into account and the uncertainty is overestimated. Further improvement can be done by including uncertainties correlations. The correspond values of the raw yields for different variation can be seen in Table 5.6.
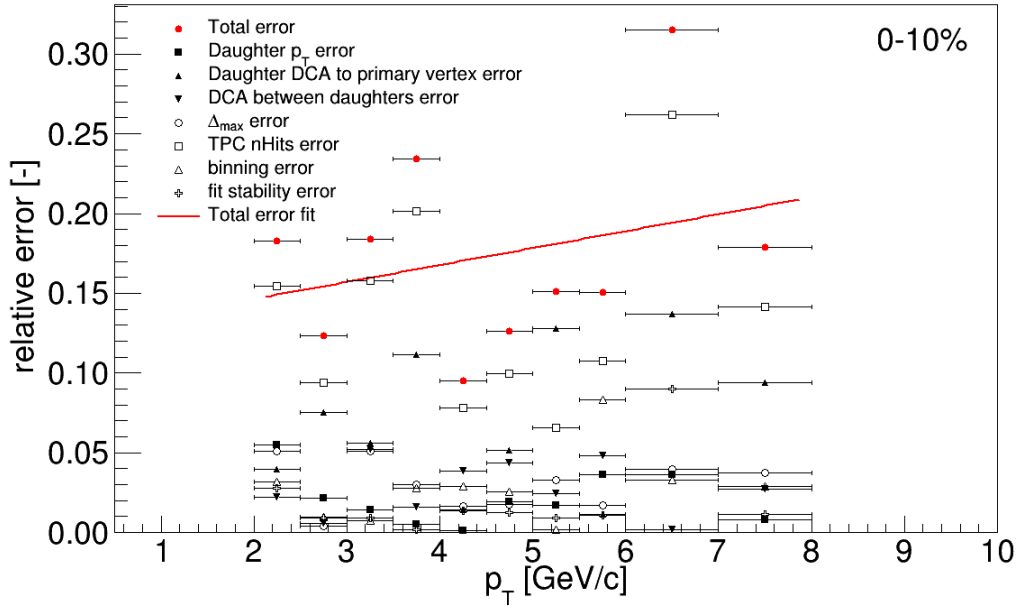
Figure 5.2: The D$^{\pm}$ systematic uncertainty for 0–10%. Red circle represent total relative systematic uncertainty calculated with equation (5.4) and rest represent relative systematic uncertainty for each variation. Red curve is first order polynomial function to soften bin effect deviation.

The systematic uncertainties for centrality 0–10% can be seen in Figure 5.2. Since the uncertainty fluctuates between bins, which is unphysical, a fit with first order polynomial function (constant function for 10–40%) was made. If the systematic

error on the edges does not follow group behavior as the rest, direct value has been taken instead of the one obtained from fitting function. For centralities 10–40% and 0–80% this applies to 1–2 GeV/c bin and for centrality 40–80% to 1–2 and 2–2.5 GeV/c bin. Yield relative uncertainty for studied centralities can be seen in Table 5.4.

p_{T} [GeV/c]	Relative uncertainty [%]			
	0–10%	10–40%	40–80%	0–80%
$0 - 1.0$	-	-	-	-
$1.0 - 2.0$	-	30.1	12.7	50.0
$2.0 - 2.5$	14.9	10.1	8.4	9.2
$2.5 - 3.0$	15.4	10.1	4.5	9.4
$3.0 - 3.5$	16.0	10.1	6.9	9.6
$3.5 - 4.0$	16.5	10.1	9.4	9.7
$4.0 - 4.5$	17.0	10.1	11.9	9.9
$4.5 - 5.0$	17.6	10.1	14.4	10.0
$5.0 - 5.5$	18.1	10.1	16.9	10.2
$5.5 - 6.0$	18.6	10.1	19.3	10.3
$6.0 - 7.0$	19.4	10.1	23.1	10.6
$7.0 - 8.0$	20.5	10.1	-	10.9
$8.0 - 10.0$	-	10.1	-	11.4

Table 5.4: The D$^{\pm}$ yields relative systematic uncertainties for different centralities. For centralities 10–40% and 0–80% value for $1.0 - 2.0$ GeV/c bin and for centrality 40–80% a value for $1.0 - 2.0$ and $2.0 - 2.5$ GeV/c bin was taken directly from calculation instead of fitting function, as it does not follow group behavior.

Finally, last uncertainty in the calculation is the Branching ratio BR = (9.13±0.19)%, which has the uncertainty of 2.1%. Summarized uncertainties for the invariant yield can be found in Table 5.5. The total uncertainty is calculated as a square root of sum of squared uncertainties in Table 5.5.

Uncertainty type	Uncertainty [%]
Yield	Table 5.4
$Eff(p_T)$	5
BR	2.1

Table 5.5: The D$^{\pm}$ invariant yield uncertainty list. Yield uncertainty calculated with topological cuts variation and $Eff(p_T)$ from comparison with GEANT.

p_T [GeV/c]	Base	Daughter p_T	Particle DCA	DCA_{XY}	Δ_{max}	N_{TPC}	binning	Fit stability
$1.0 - 2.0$	263 ± 286	495 ± 246	701 ± 468	594 ± 328	300 ± 291	558 ± 315	219 ± 296	219 ± 296
$2.0 - 2.5$	580 ± 120	496 ± 112	637 ± 200	632 ± 137	553 ± 123	670 ± 132	564 ± 127	564 ± 127
$2.5 - 3.0$	757 ± 73	726 ± 70	738 ± 118	823 ± 82	758 ± 75	828 ± 80	749 ± 74	750 ± 74
$3.0 - 3.5$	471 ± 41	458 ± 40	525 ± 61	481 ± 46	498 ± 43	545 ± 45	475 ± 41	475 ± 41
$3.5 - 4.0$	273 ± 24	264 ± 23	321 ± 30	287 ± 26	283 ± 25	328 ± 26	273 ± 24	273 ± 24
$4.0 - 4.5$	182 ± 17	178 ± 17	191 ± 20	186 ± 18	187 ± 18	197 ± 18	185 ± 17	185 ± 17
$4.5 - 5.0$	86 ± 11	83 ± 11	86 ± 12	86 ± 12	88 ± 11	94 ± 12	87 ± 11	87 ± 11
$5.0 - 5.5$	57 ± 10	57 ± 10	53 ± 11	58 ± 10	56 ± 10	61 ± 10	58 ± 10	58 ± 10
$5.5 - 6.0$	36 ± 6	35 ± 6	39 ± 7	36 ± 6	36 ± 6	40 ± 7	36 ± 7	36 ± 7
$6.0 - 7.0$	28 ± 7	26 ± 6	33 ± 7	29 ± 7	29 ± 7	35 ± 7	30 ± 7	30 ± 7
$7.0 - 8.0$	13 ± 3	13 ± 3	15 ± 4	13 ± 3	12 ± 3	14 ± 4	14 ± 4	12 ± 3
$8.0 - 10.0$	7 ± 3	6 ± 3	8 ± 3	7 ± 3	8 ± 3	7 ± 3	10 ± 3	9 ± 3

Table 5.6: The D$^\pm$ yields for different variated variables for centrality 0–10%. Base yield represent yield obtained with cuts listed in Table 4.3 and the rest are variated variables according to list in Chapter 5.2.

5.3 Correction of the p_{T}

After the efficiency correction the bin content stands for the corrected integrated yield of the bin. If one places the data point in the bin center, the result would be unphysical because of the shape of the spectrum inside the p_{T} bin. As a solution, one can place the data points at the position of the mean of the corrected p_{T} spectrum inside the p_{T} bin. This way, the results can also be interpreted as a measurement at a fixed position along x-axis.

Let's assume the measurements can be fitted with a function $f(x)$, then we need to find a value x_0 as

$$f(x_0) = \frac{\int_{x_{min}}^{x_{max}} f(x)dx}{x_{max} - x_{max}}, \tag{5.5}$$

where x_{min} and x_{max} are the bin boundaries. This is an iterative process and we demanded 3 iterations. As a function f(x) we used Levy-function [56] for signal spectrum

$$f(p_T) = \frac{A}{2\pi} \cdot \frac{(b-1)(c-2)}{((bc+m)(m(c-1)+bc))} \cdot \left(\frac{bc + \sqrt{p_T^2 + m^2}}{bc + m}\right)^{-2}, \tag{5.6}$$

where A, b and c are real parameters, $m = 1.869$ GeV is our D-meson theoretical mass and p_{T} is transverse momenta. As can be seen, this correction will have larger impact to wider bins. This correction was done for all centralities, an example of centrality 0–80% can be seen in Figure 5.3. Corrected point position for all centralities is summarized in Table 5.7.
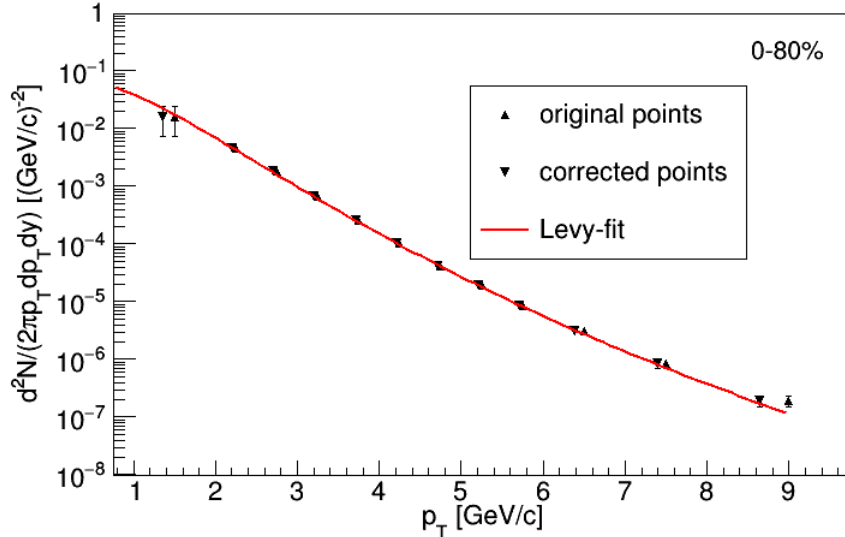

Figure 5.3: The invariant yield x-bin position correction owing to spectra shape for centrality 0–80%. The triangle represent original position and the upside down triangle corrected position after 3 iteration. For the spectra shape a Levy function (5.6) was used and the points errors include both systematic and statistical uncertainty.

p_T [GeV/c]	$p_T^{bin\ center}$ [GeV/c]	$p_T^{corrected}$ [GeV/c]			
		0–10%	10–40%	40–80%	0–80%
$0 - 1.0$	0.5	-	-	-	-
$1.0 - 2.0$	1.5	-	1.36	1.39	1.36
$2.0 - 2.5$	2.25	2.21	2.21	2.22	2.21
$2.5 - 3.0$	2.75	2.71	2.71	2.71	2.71
$3.0 - 3.5$	3.25	3.21	3.21	3.21	3.21
$3.5 - 4.0$	3.75	3.71	3.71	3.71	3.71
$4.0 - 4.5$	4.25	4.21	4.21	4.21	4.21
$4.5 - 5.0$	4.75	4.71	4.72	4.71	4.72
$5.0 - 5.5$	5.25	5.22	5.22	5.22	5.22
$5.5 - 6.0$	5.75	5.72	5.72	5.72	5.72
$6.0 - 7.0$	6.50	6.39	6.39	6.37	6.39
$7.0 - 8.0$	7.50	7.40	7.40	-	7.39
$8.0 - 10.0$	9.00	-	8.65	-	8.65

Table 5.7: The D$^\pm$ invariant yields p_T-position correction by Levy function. p_T is transverse momentum range, $p_T^{bin\ center}$ its bin center and $p_T^{corrected}$ corrected position for different centralities.

5.4 Corrected invariant yield

Finally, the yield after the normalization and the bin position correction can be found in Figure 5.4 and Figure 5.5. The probability of D$^\pm$ and D^0 formation differs, this is described by fragmentation functions

$$f(c \rightarrow D^0) = 0.565 \pm 0.032$$
$$f(c \rightarrow D^\pm) = 0.246 \pm 0.020 \tag{5.7}$$

Therefore, the D$^\pm$ have been multiplied by c-quark fragmentation function [18] to be comparable with D^0 measurements. The data were compared to 2010 published D^0 data [23] and 2014 preliminary data [20]. The D$^\pm$ invariant yield from measurement with HFT is consistent with the D^0 yield from measurement with (2014) and without (2010/2011) HFT within uncertainties. Moreover, the D$^\pm$ provides more points in p_T range $2 - 8$ GeV/c than the D^0 measurements.
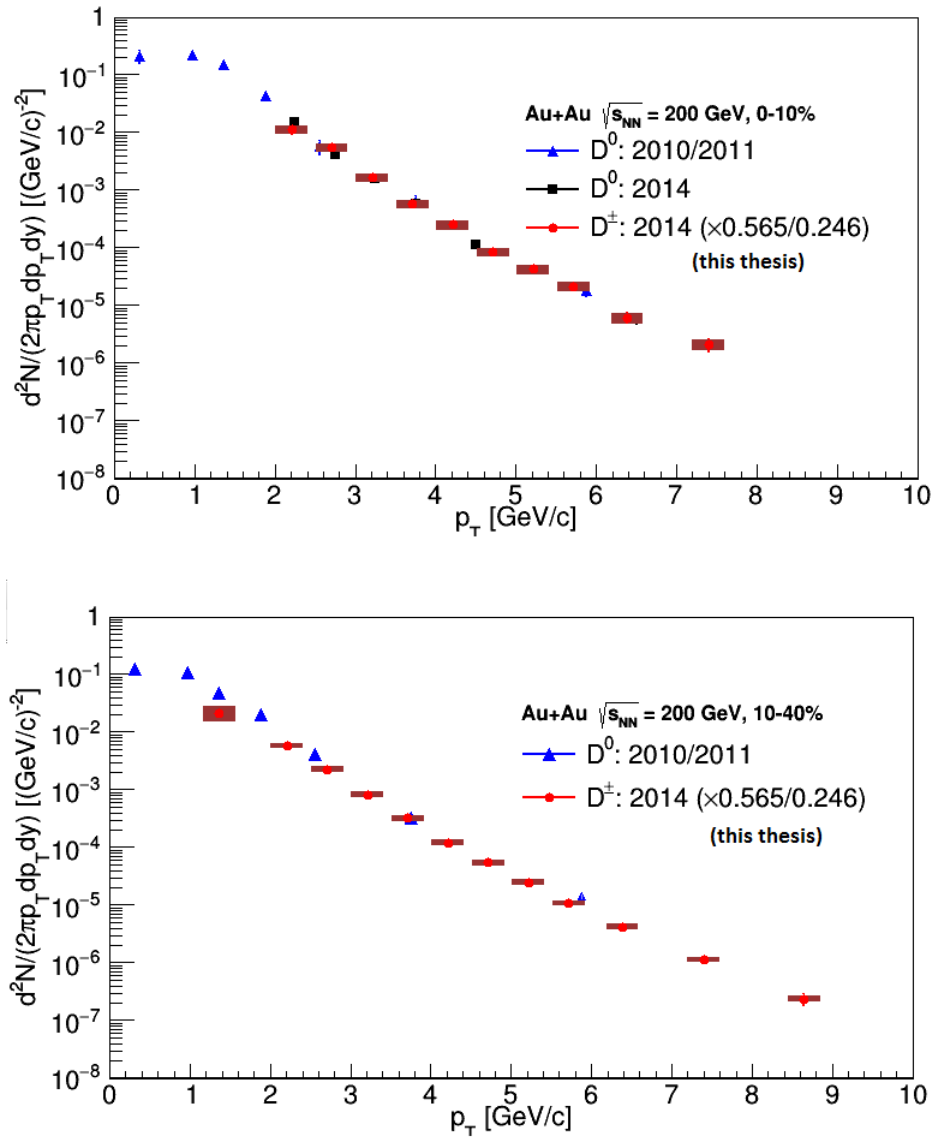
Figure 5.4: The $D^{\pm}$ invariant yield for centrality 0–10% and 10–40%. Red points are this analysis, blue points STAR published data from year 2010 [23] and black points preliminary data from 2014 [20]. $D^{\pm}$ are multiplied by c quark fragmentation function to be comparable with D^0.
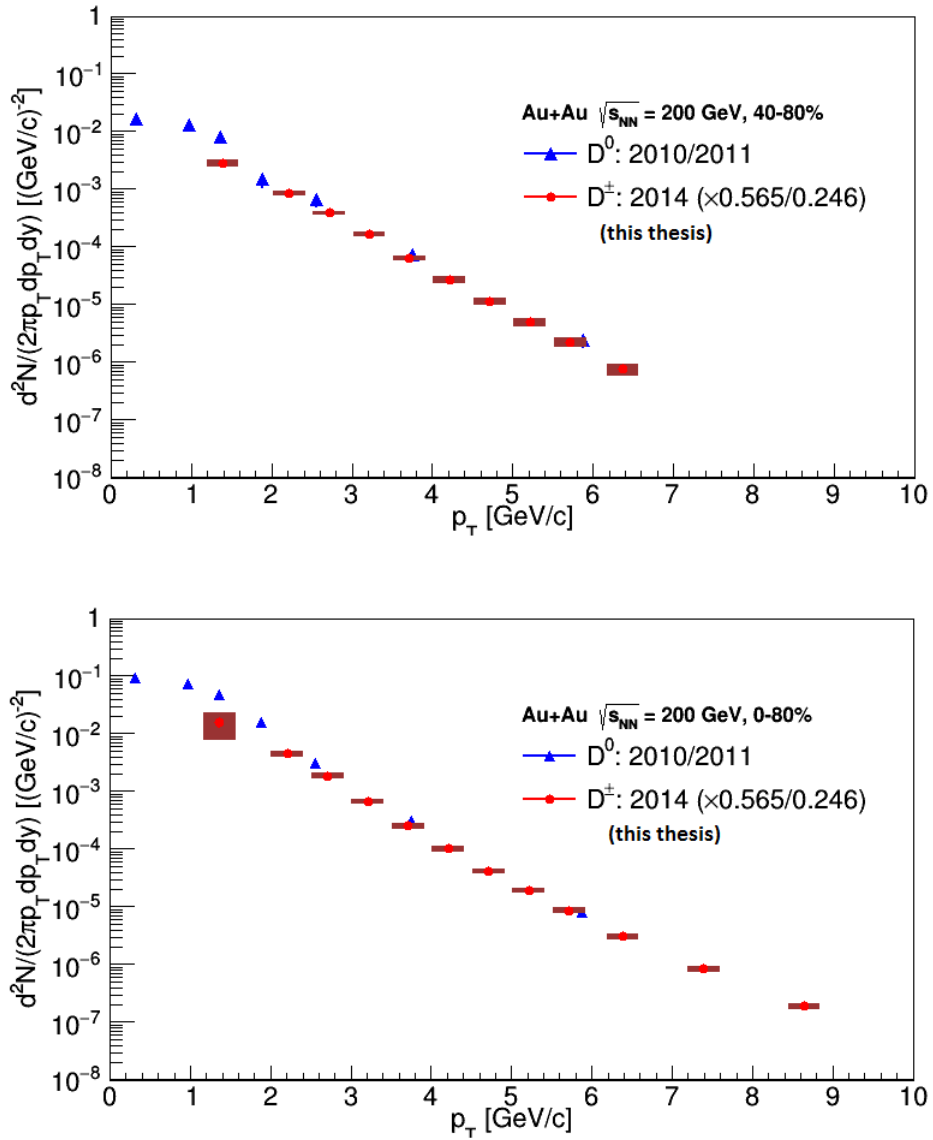
Figure 5.5: The $D^{\pm}$ invariant yield for centrality 40–80% and 0–80%. Red points are this analysis and blue points STAR published data from year 2010 [23]. $D^{\pm}$ are multiplied by c quark fragmentation function to be comparable with D^0.

Chapter 6

Nuclear modification factor of $D^{\pm}$

The nuclear modification factor was defined in Chapter 1.4. As can be seen nuclear modification factor shows the particle production modification between two systems and can be used to study the medium behavior, which is expected to be created in heavy-ion collisions.

As a proton–proton reference, D^0 invariant yields from data taken in the year 2009 were used. First, the baseline must be scaled to $D^{\pm}$ yield by fragmentation functions mentioned in Chapter (5.7), their systematic errors were included in the baseline systematic uncertainty.

The p+p reference was fitted with a Levy function and was used in our calculation. The p+p data go up to $p_T = 7$ GeV which is why the R_{AA} is plotted only up to 7 GeV/c as well. Since we have p+p uncertainty for only a few data points, which do not match ours the reference has to be interpolated. The uncertainty follows a common behavior which can be parametrized by the following second order polynomial

$$Yield_{pp}^{rel.\ unc.}(p_T) = 0.003p_T^2 - 0.01p_T + 0.32 \qquad (6.1)$$

The systematic uncertainties of R_{AA} can be seen in Table 6.1. The total uncertainty is calculated as square root of sum of squared uncertainties.

Uncertainty type	uncertainty [%]			
	0–10%	10–40%	40–80%	0–80%
$Yield_{AA}^{rel.\ unc.}$	Table 5.5			
$Yield_{pp}^{rel.\ unc.}$	equation 6.1			
$f(c \to D^0)$	5.7			
$f(c \to D^{\pm})$	8.1			
N_{coll}	2.9	7.8	24.3	7.0
σ_{pp}	8.0			

Table 6.1: The $D^{\pm}$ nuclear modification factor uncertainties. The uncertainty for the yields $Yield_{AA}$ and $Yield_{pp}$, the fragmentation function, the number of collisions N_{coll} and the proton–proton collision cross section σ_{pp} have been included.

The $D^{\pm}$ nuclear modification factor for centrality 0–10% and 10–40% can be seen in Figure 6.1 and for centrality 40–80% and 0–80% can be seen in Figure **??**. The measurement is consistent with D^0 for $p_{\mathrm{T}} > 3$ GeV/c showing a maximum suppression $R_{\mathrm{AA}} = 0.2$ for 0–10% and $R_{\mathrm{AA}} = 0.3$ for 10–40% centrality range, both around $p_{\mathrm{T}} \sim 6.5$ GeV/c. For the 40–80% centrality the measurements are consistent for $p_{\mathrm{T}} > 2$ GeV/c showing a maximum suppression $R_{\mathrm{AA}} = 0.4$ around $p_{\mathrm{T}} \sim 6.5$ GeV/c. This follows the expected behavior that central collisions are more suppressed then peripheral collisions. The 0–80% is consistent with $D^{\pm}$ for $p_{\mathrm{T}} > 2.5$ GeV/c showing a maximum $R_{\mathrm{AA}} = 0.3$ around $p_{\mathrm{T}} \sim 6.5$ GeV/c. The R_{AA} differs for $p_{\mathrm{T}} \lesssim 2.5$ GeV/c. The $D^{\pm}$ topological selection criteria are currently under study to get more point in this region. The D^0 is under study as well indicating that the enhancement will be much smaller.

The $D^{\pm}$ R_{AA} for centrality 0–10% compared with theoretical models can be seen in Figure 6.3. The Duke [14] model uses the diffusion coefficient of $2\pi T D_s = 7$, where D_s is the heavy quark diffusion coefficient and T is the temperature of the medium. The TAMU [11] model uses an a non-perturbative approach with the diffusion coefficient of $2\pi T D_s \sim 2$–10. The SUBATECH [13] model uses a pQCD calculation with $2\pi T D_s \sim 2$–4 [20]. The SUBATECH model is consistent with the measurement. TAMU and Duke calculations are slightly overestimated, but taking uncertainties into account, one can also claim that these calculations describe the data. To make a final conclusion about theoretical models one needs to test these model with flow v_2 as well.
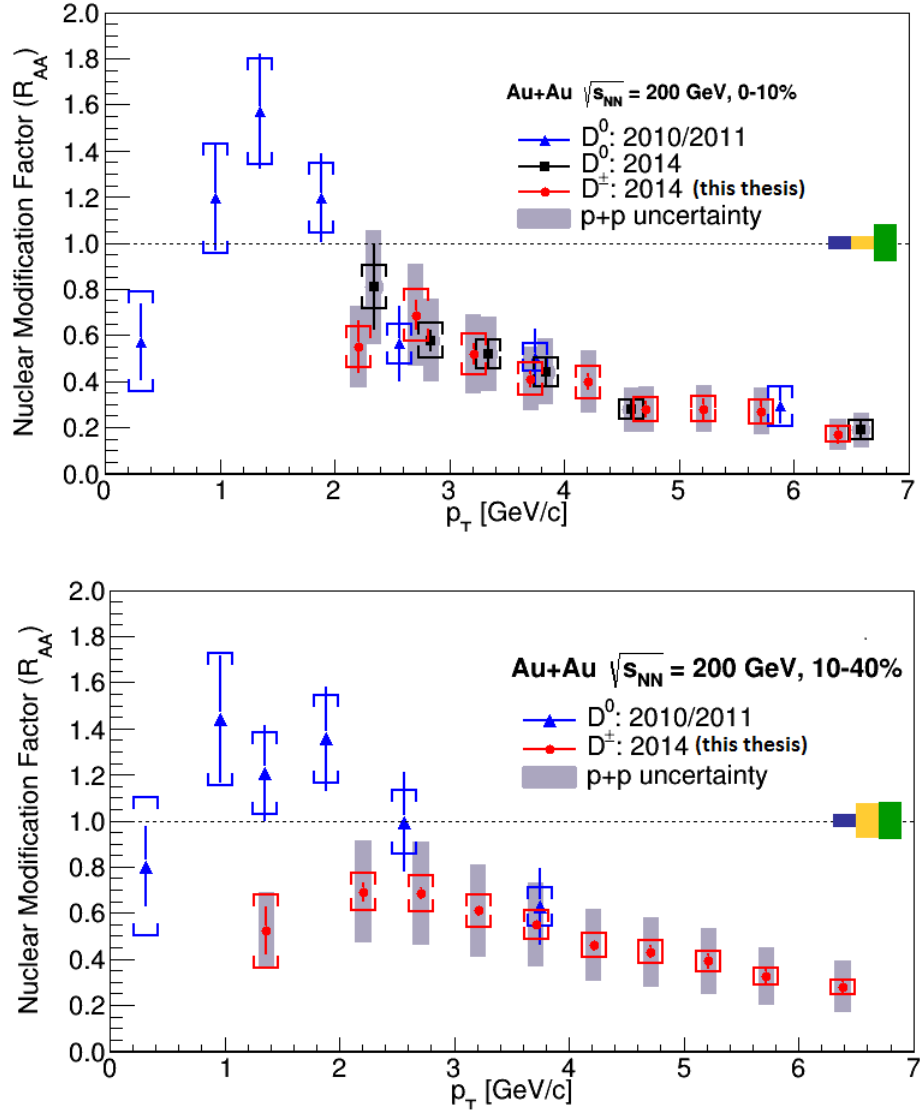
Figure 6.1: The $D^{\pm}$ nuclear modification factor for centrality 0–10% and 10–40%. The red points are this analysis, blue points are the STAR published data from the year 2010 [23] and black points are the preliminary data from 2014 [20]. The statistical uncertainties are drawn as lines and the systematical uncertainties are shown as the square brackets. The gray boxes indicate the uncertainty of the p+p reference spectra. The global uncertainties are: dark blue – number of collisions N_{coll} for year 2010, orange – N_{coll} for year 2014 and green – proton–proton cross section σ_{pp}.
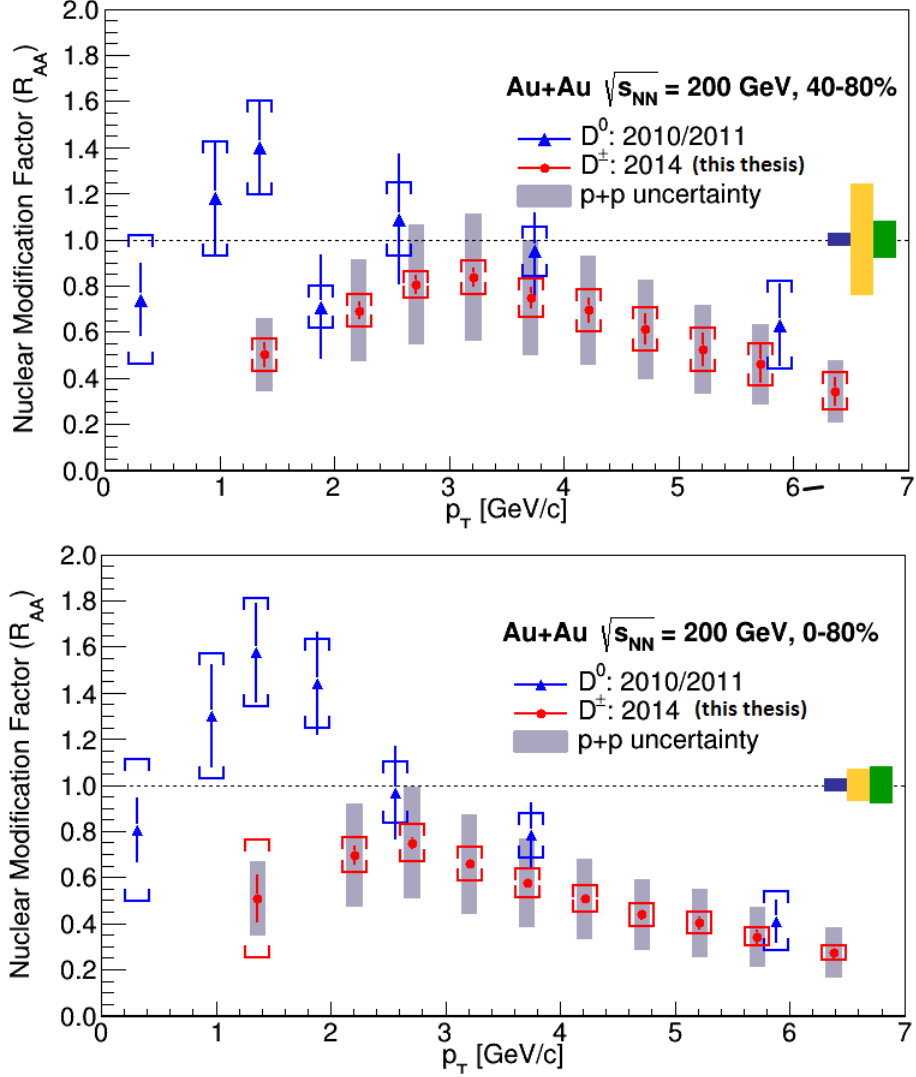
Figure 6.2: The $D^{\pm}$ nuclear modification factor for centrality 40–80% and 0–80%. The red points are this analysis and blue points are the STAR published data from the year 2010 [23]. The statistical uncertainties are drawn as lines and the systematical uncertainties are shown as the square brackets. The gray boxes indicate the uncertainty of the p+p reference spectra. The global uncertainties are: dark blue – number of collisions N_{coll} for year 2010, orange – N_{coll} for year 2014 and is green – proton–proton cross section σ_{pp}.
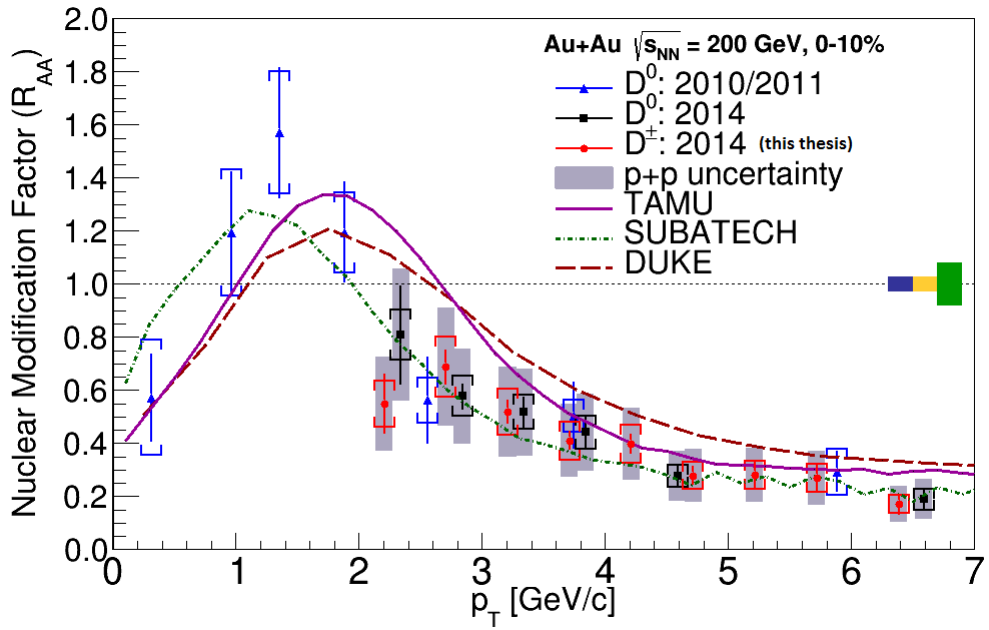
Figure 6.3: The $D^{\pm}$ nuclear modification factor for centrality 0–10% compared to theoretical models (TAMU [11], SUBATECH [13] and Duke [14]). The red points are this analysis, blue points are the STAR published data from the year 2010 [23] and black points are the preliminary data from 2014 [20]. The statistical uncertainties are drawn as lines and the systematical uncertainties are shown as the square brackets. The gray boxes indicate the uncertainty of the p+p reference spectra. The global uncertainties are: dark blue – number of collisions N_{coll} for year 2010, orange – N_{coll} for year 2014 and is green – proton–proton cross section σ_{pp}.

Chapter 7

Summary

The Heavy Flavor Tracker provides an excellent tool for measurements of heavy flavor hadrons via precise measurements of decay vertices. Heavy quarks (b,c) are created in hard processes at the beginning of the heavy-ion collision and, thus, experience the whole evolution of the hot and dense nuclear matter and can act as a good probe to the physical properties of the strongly interacting quark-gluon plasma.

First direct reconstruction of $D^{\pm}$ meson signal has been made in Au+Au collisions at $\sqrt{s_{NN}} = 200$ GeV. This measurement is possible because of the sufficient tracking resolution provided by the HFT. This is the first $D^{\pm}$ measurement made at RHIC. Finally, the invariant mass distribution has been evaluated with subtracted background via the wrong-sign method with a remarkable peak significance. The measurement was done in several transverse momentum bins p_{T}: $1.0 - 2.0$, $2.0 - 2.5$, $2.5 - 3.0$, $3.0 - 3.5$, $3.5 - 4.0$, $4.0 - 4.5$, $4.5 - 5.0$, $5.0 - 5.5$, $5.5 - 6.0$, $6.0 - 7.0$, $7.0 - 8.0$ and $8.0 - 10.0$ GeV/c for centralities 0–10%, 10–40%, 40–80% and 0–80%.

Furthermore, corrections on detector efficiency and acceptance were done and invariant yield spectra were calculated. This measurement is consistent with the D^{0} invariant yield. With a proton–proton baseline from the D^{0} data collected in the year 2009 a nuclear modification factor was evaluated. The nuclear modification factor is showing a large suppression of $D^{\pm}$ in 0–10% central Au+Au collisions. For larger p_{T} up to $R_{AA} = 0.2$, indicating a significant suppression to the D meson production in heavy ion collisions compared to the proton–proton collisions. In comparison the peripheral collisions (centrality 40–80%) is indicating smaller suppression in order $R_{AA} = 0.4$. Again, this measurement is consistent with the D^{0} measurement.

This work is a good baseline for further studies. We need to explore low p_{T} part of the spectra and also use data from 2016 to enlarge data sample. As well systematic uncertainties has to be further studied.

List of abbreviation

AGS .... Alternating Gradient Synchrotron

ALICE .... A Large Ion Collider Experiment

BEMC .... Barrel Electromagnetic Calorimeter

BGRR .... Brookhaven Graphite Research Reactor

BLIP .... Brookhaven Linac Isoptope Producer

BMRR .... Brookhaven Medical Research Reactor

BNL .... Brookhaven National Laboratory

BR .... Branching Ratio

BRAHAMS ...... Broad RAnge Hadron Magnetic Spectrometers

BSMD .... Barrel Shower Maximum detector

CBM .... Compressed Baryonic Matter experiment

CERN .... European Organization for Nuclear Research

CFN .... Center for Functional Nanomaterials

CMOS .... Complementary Metal Oxide Semiconductor

CMS .... Compact Muon Solenoid

CNM .... Cold Nuclear Matter

DAQ .... Data acquisition

DCA .... Distance of Closest Approach

EBIS .... Electron Beam Ion Source

eRHIC .... The electron Relativistic Heavy Ion Collider

FAIR .... Facility for Antiproton and Ion Research

FONLL .... Fixed-Order Next-to-Leading-Log

HFBR . . . . High Flux Beam Reactor

HFT . . . . Heavy Flavor Tracker

IST . . . . Intermediate Silicon Tracker

LHC . . . . The Large Hadron Collider

LHCb . . . . Large Hadron Collider beauty

Linac . . . . Linear accelerator

LO . . . . Leading order

MAPS . . . . Monolithic Active Pixel Sensor

MRPC . . . . Multigap Resistive Plate Chambers

MTD . . . . Muon Telescope Detector

MWPC . . . . Multi-Wire Proportional Chambers

NLO . . . . Next-to-Leading Order

NSLS . . . . National Synchrotron Light Source

NSLS-II . . . . National Synchrotron Light Source II

NSRL . . . . NASA Space Radiation Laboratory

PHENIX . . . . Pioneering High Energy Nuclear Interaction eXperiment

PIS . . . . Particle IDentification

pQCD . . . . perturbative Quantum Chromodynamics

PXL . . . . Pixel detector

QA . . . . Quality Assurance

QCD . . . . Quantum Chromodynamic

QGP . . . . Quark-Gluon Plasma

RHIC . . . . The Relativistic Heavy Ion Collider

RHICf . . . . RHIC forward

SPS . . . . Super Proton Synchrotron

SSD . . . . Silicon Strip Detector

STAR . . . . Solenoidal Tracker At RHIC

TOF .... Time of Flight

TPC .... Time Projection Chamber

VPD .... Vertex Position Detector

Bibliography

[1] M. Gyulassy, *The QGP discovered at RHIC*, C03-09-22.2, p.159-182

[2] D. Tlusty, *A Study of Open Charm Production in p+p Collisions at STAR*, PhD. thesis, FNSPE CTU, 2014.

[3] Brookhaven National Laboratory, *Supercomputing the Transition from Ordinary to Extraordinary Forms of Matter* [Online], cit. 15.4.2017 `https://www.bnl.gov/newsroom/news.php?a=24281`.

[4] M. Kliemant *et al.*, *Global Properties of Nucleus–Nucleus Collisions*, Lect. Notes Phys. 785, 23–103 (2010)

[5] S. Sarkar, H. Satz, B. Sinha, *The Physics of the Quark-gluon Plasma: Introductory Lectures*, Berlin: Springer, 2010.

[6] R. Vogt, *Ultrarelativistic Heavy-Ion Collisions*, Elsevier, 2007.

[7] M. L. Miller *et al.*, *Glauber modeling in high energy nuclear collisions*, Ann. Rev. Nucl. Part. Sci. 57 (2007) 205-243

[8] D. d'Enterria, B. Betz, *High-pT Hadron Suppression and Jet Quenching*, Lect. Notes Phys. 785, 285–339 (2010)

[9] R. Thomas *et al.*, *Gluon emission of heavy quarks: Dead cone effect*, Acta Phys.Hung. A22 (2005) 83-91

[10] STAR Collaboration, *Elliptic Flow in Au+Au Collisions at $\sqrt{s_{NN}}$ = 130 GeV*, Phys. Rev. Lett. 86 (2001) 402

[11] M. He, R. J. Fries, R. Rapp, *Heavy-Quark Diffusion and Hadronization in Quark-Gluon Plasma*, Phys.Rev. C86 (2012) 014903

[12] M. Lomnitz, *Measurement of D^0 elliptic and triangular flow in Au+Au collisions at $\sqrt{s_{NN}} = 200$ GeV at RHIC*, J. Phys.: Conf. Ser. 779 012059

[13] P.B. Gossiaux *et al.*, *Competition of Heavy Quark Radiative and Collisional Energy Loss in Deconfined Matter*, J.Phys. G37 (2010) 094019

[14] S. Cao, G. Qin, S. A. Bass, *Heavy quark dynamics and hadronization in ultra-relativistic heavy-ion collisions: collisional versus radiative energy loss*, Phys.Rev. C88 (2013) 044907

[15] R. Russo, *Measurement of* D^+ *Meson Production in p-Pb Collisions with AL-ICE detector*, PhD. thesis, University of Torino, 2014.

[16] A. Andronic *et al.*, *Heavy-flavour and quarkonium production in the LHC era: from proton–proton to heavy-ion collisions*, Eur. Phys. J. C **76** (2016) no.3, 107

[17] J. Beringer *et al.* (Particle Data Group), Phys. Rev. D86, 010001 (2012)

[18] C. Amsler et al. (Particle Data Group), Physics Letters B667, 1 (2008). `http://pdg.lbl.gov/2008/reviews/fragrpp.pdf`

[19] D. Tlusty, STAR Collaboration, *Open charm hadron production via hadronic decays at STAR*, Nucl.Phys. A910-911 (2013) 289-292.

[20] G. Xie, STAR Collaboration, *Nuclear Modification Factor of* D^0 *Meson in Au + Au Collisions at* $\sqrt{s_{\mathrm{NN}}} = 200$ *GeV*, Nucl.Phys. A956 (2016) 473-476

[21] ALICE Collaboration, *Transverse momentum dependence of D-meson production in Pb-Pb collisions at* $\sqrt{s_{NN}} = 2.76$ *TeV*, JHEP 1603 (2016) 081

[22] Md. Nasim, STAR collaboration, *Measurement of* $D_s^{\pm}$*-meson production in Au+Au collisions at* $\sqrt{s_{NN}} = 200$ *GeV in STAR*, Nuclear Physics A Volume 956, December 2016, Pages 509-512

[23] L. Adamczyk, STAR Collaboration, *Observation of* D^0 *Meson Nuclear Modification in Au+Au Collisions at* $\sqrt{s_{\mathrm{NN}}} = 200$ *GeV*, Phys.Rev.Lett. 113 (2014) no.14, 142301

[24] CMS Collaboration, D^0 *meson nuclear modification factor in PbPb collisions at* $\sqrt{s_{NN}} = 2.76$ *TeV*, CMS-PAS-HIN-16-001

[25] ALICE Collaboration, *Measurements of promtp charm production cross-section in pp at* $\sqrt{s} = 13$ *TeV*, JHEP 1603 (2016) 159

[26] Brookhaven National Laboratory, *Brookhaven's Research Facilities* [Online], cit. 16.3.2017 `https://www.bnl.gov/science/facilities.php`.

[27] Brookhaven National Laboratory, *A History of Leadership in Particle Accelerator Design* [Online], cit. 16.3.2017 `https://www.bnl.gov/about/history/accelerators.php`.

[28] Brookhaven National Laboratory, *Brookhaven History: Using Reactors as Research Tools* [Online], cit. 16.3.2017 `https://www.bnl.gov/about/history/reactors.php`.

[29] Brookhaven National Laboratory, *Research Awards* [Online], cit. 16.3.2017 `https://www.bnl.gov/about/awards`.

[30] Brookhaven National Laboratory, *Our History of Discovery* [Online], cit. 16.3.2017 `https://www.bnl.gov/about/history/discoveries.php`.

[31] H. Hahn, E. Forsyth, H. Foelsche, et al., *The RHIC design overview*, Nucl.Instrum.Meth., vol. A499, pp. 245–263, 2003

[32] Brookhaven National Laboratory, *The Relativistic Heavy Ion Collider* [Online], cit. 27.4.2017 `http://www.bnl.gov/rhic/default.asp`.

[33] Brookhaven National Laboratory, *The STAR experiment* [Online], cit. 27.4.2017 `https://www.star.bnl.gov/central/collaboration/`.

[34] W. Fischer, *Run overview of the Relativistic Heavy Ion Collider* [Online], cit. 27.4.2017 `http://www.rhichome.bnl.gov/RHIC/Runs/`.
.

[35] The STAR Collaboration, *RHIC Beam Use Request For Runs 17 and 18*, internal document, cit. 27.4.2017.

[36] D. Kharzeev, *Theoretical outlook*, QCD Chirality Workshop, UCLA, 2015

[37] Z. Xu, *STAR BES-I highlights and RHIC BES-II program*, CPOD, Wroclaw, Poland 2016

[38] The STAR Collaboration, *Memorandum of Understanding between the STAR and RHICf collaborations*, internal document, cit. 27.4.2017.

[39] K. M. Walsh, *Accelerating Particles Accelerates Science — With Big Benefits for Society* [Online], cit. 27.4.2017 `http://www.bnl.gov/rhic/news2/news.asp?a=3758&t=today`.

[40] W. Fisher, J. Alessi, M. Blaskiewicz, et al., *RHIC Collider Projections (FY 2016 - FY 2022)* [Online], cit. 27.4.2017 `http://www.rhichome.bnl.gov/RHIC/Runs/RhicProjections.pdf`.

[41] K.H. Ackermann, N. Adams, C. Adler, et al., *STAR detector overview*, Nucl.Instrum.Meth., vol. A499, pp. 624–632, 2003

[42] C. Yang, X. J. Huang, C. M. Du, et al., *Calibration and performance of the STAR Muon Telescope Detector using cosmic rays*, Nucl.Instrum.Meth., vol. A762, pp. 1-6, 2014

[43] STAR Collaboration, *STAR Muon Telescope Detector Proposal*, [Online], cit. 27.4.2017 `http://www.star.bnl.gov/~ruanlj/MTDreview2010/MTD_proposal_v14.pdf`.

[44] M. Beddo, E. Bielick, T. Fornek, et al., *The STAR Barrel Electromagnetic Calorimeter*, Nucl.Instrum.Meth., vol. A499, pp. 725-739, 2003

[45] Kohei Kajimoto, *A Large Area Time of Flight Detector for the STAR Experiment at RHIC* PhD thesis, The University of Texas in Austin, 2009, `http://repositories.lib.utexas.edu/handle/2152/7860`.

[46] STAR Collaboration, *Pion, kaon, proton and anti-proton transverse momentum distributions from p+p and d+Au collisions at 200 GeV*, Phys. Lett. B 616, pp. 8-16, 2005

[47] M. Andersona, J. Berkovitzb, W. Betts, et al., *The STAR time projection chamber: a unique tool for studying high multiplicity events at RHIC*, Nucl.Instrum.Meth., vol. A499, pp. 659–678, 2003

[48] STAR Collaboration, *A Proposal for STAR Inner TPC Sector Upgrade (iTPC)*, Cit. 27.4.2017 `https://drupal.star.bnl.gov/STAR/files/STAR_iTPC_proposal_06_09_2015.pdf`.

[49] K.A. Olive et al (Particle Data Group), Chin. Phys. C, 2014, 38(9): 090001

[50] D.Beavis et.al., *The STAR Heavy Flavor Tracker Technical Design Report*, Cit. 27.4.2017, `https://drupal.star.bnl.gov/STAR/system/files/HFT_TDR_Final.pdf`.

[51] M. Szelezniak, *Upgrade of the STAR silicon detectors*, Vertex 2014, Doksy, Czech Republic

[52] STAR Collaboration, *Measurement of D^0 azimuthal anisotropy at mid-rapidity in $Au+Au$ collisions at $\sqrt{s_{NN}} = 200$ GeV*, arXiv:1701.06060 [nucl-ex]

[53] G. Van Buren, *Developments in Tracking with STAR's Heavy Flavor Tracker*, Vertex 2015, Santa Fe, USA

[54] M. Lomnitz, *Measurement of D-meson azimuthal anisotropy in Au+Au 200GeV collisions at RHIC*, Quark Matter, Kobe, Japan 2015

[55] K.A. Olive et al. (Particle Data Group), *Review of Particle Physics, Chin. Phys. C, 38, 090001 (2014) and 2015 update*, `http://pdg.lbl.gov/2015/listings/rpp2015-list-D-plus-minus.pdf`.

[56] G. Wilk and Z. Włodarczyk, *Interpretation of the Nonextensivity Parameter q in Some Applications of Tsallis Statistics and Lévy Distributions*, Phys. Rev. Lett. 84, 2770

Appendices

Appendix A

Signal and background distributions
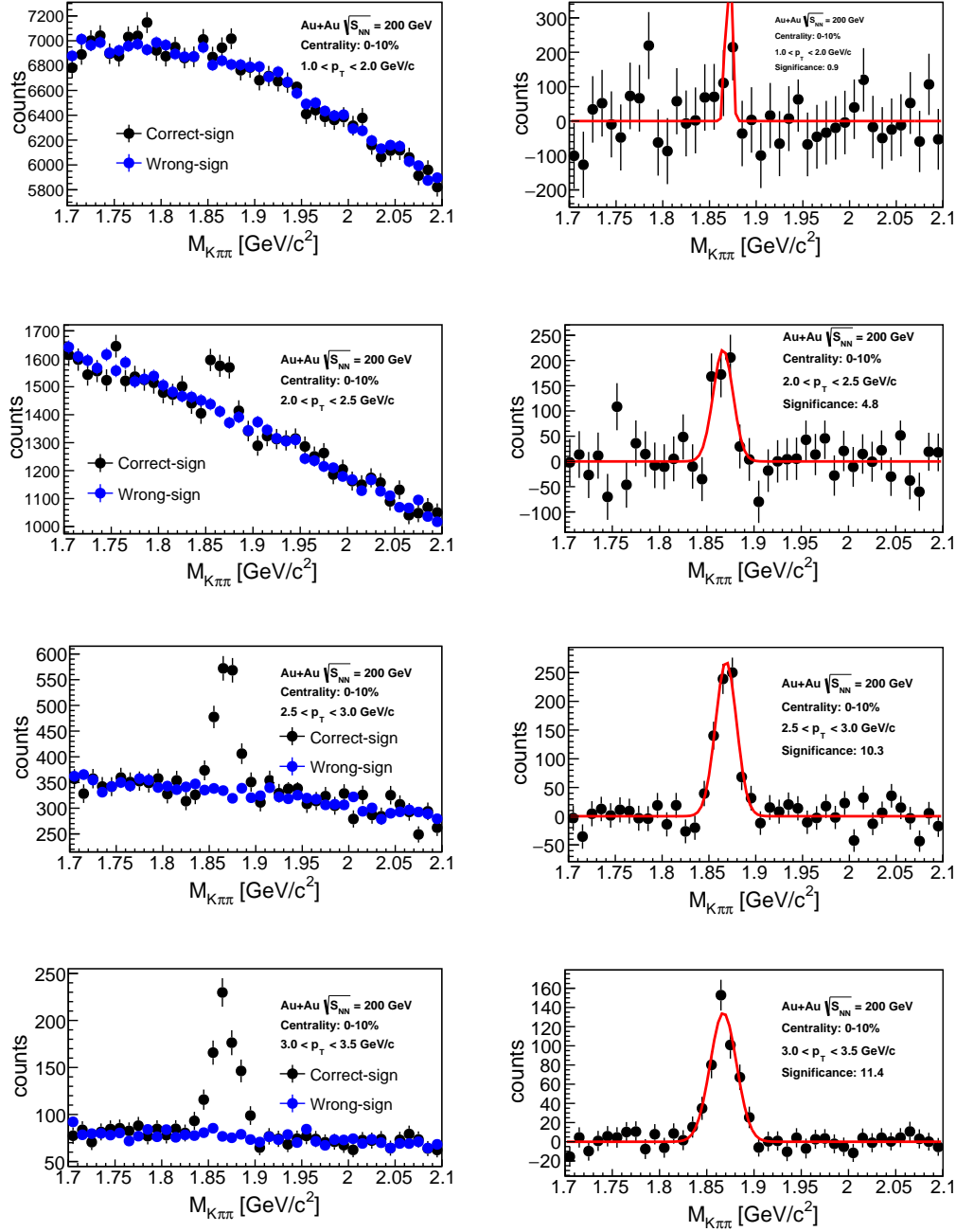
Figure A.1: The D$^{\pm}$ signal and background in centrality range 0–10% for 4 transverse momentum p_{T} bins.
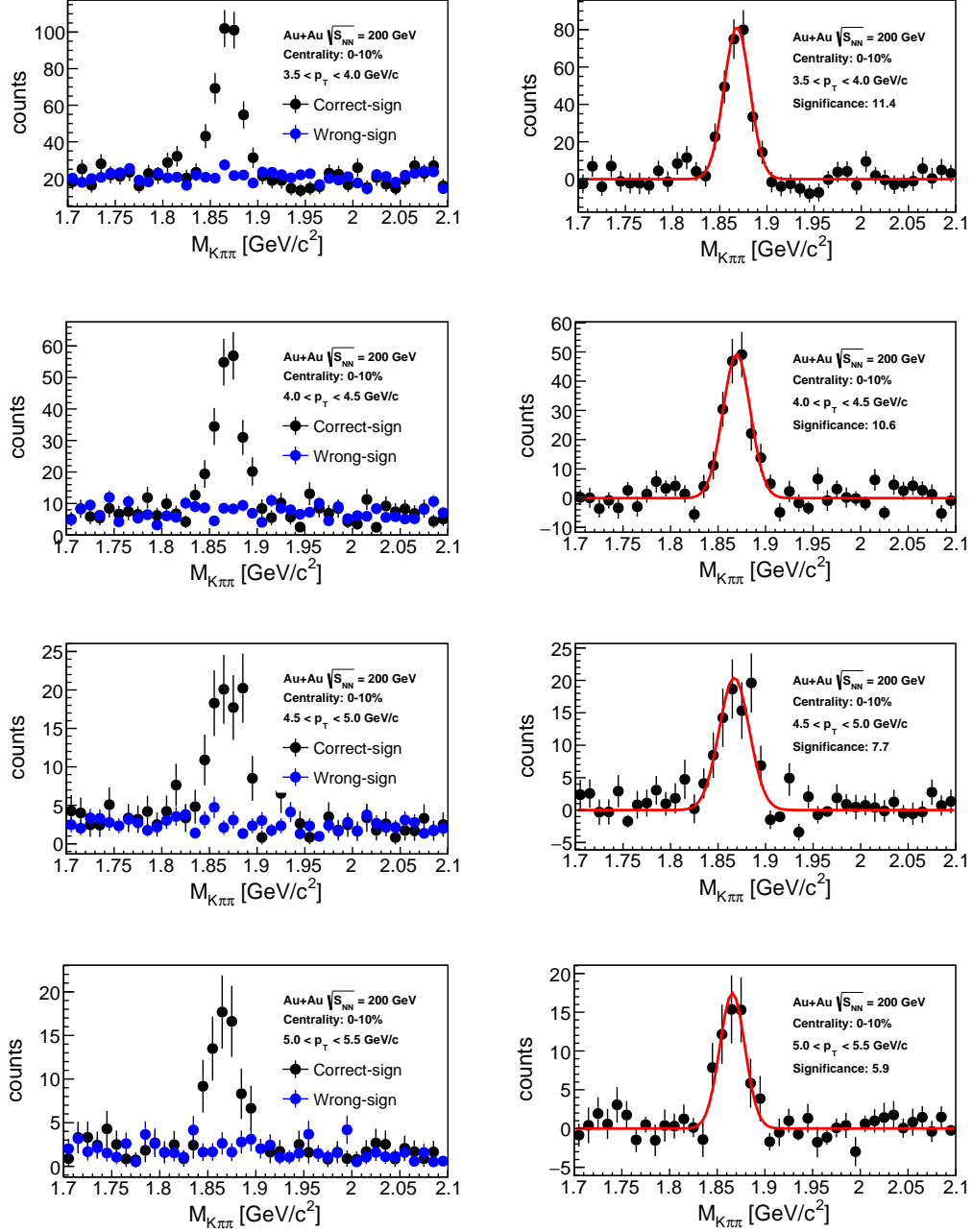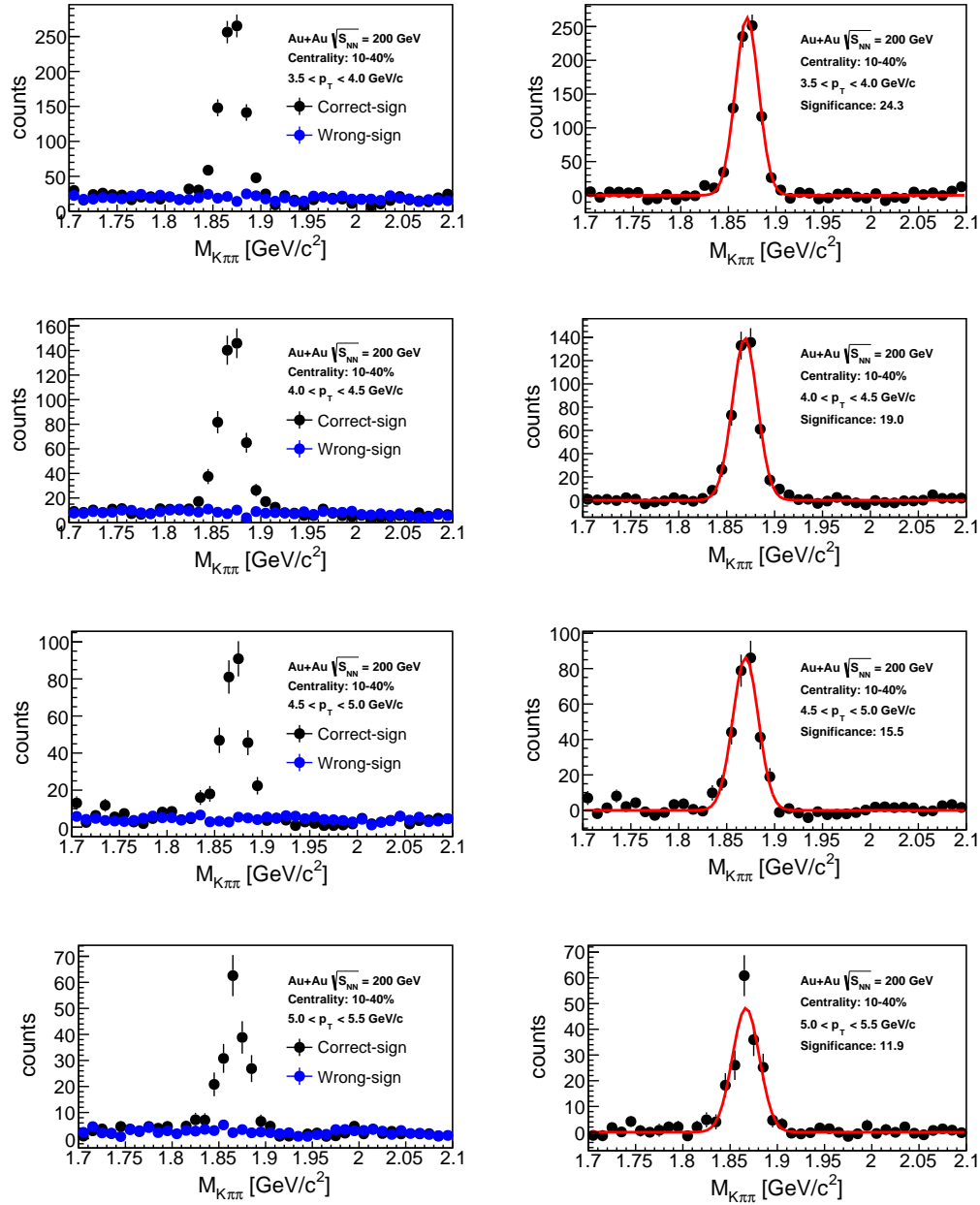
Figure A.2: The D$^{\pm}$ signal and background in centrality range 0–10% for 4 transverse momentum p_{T} bins.
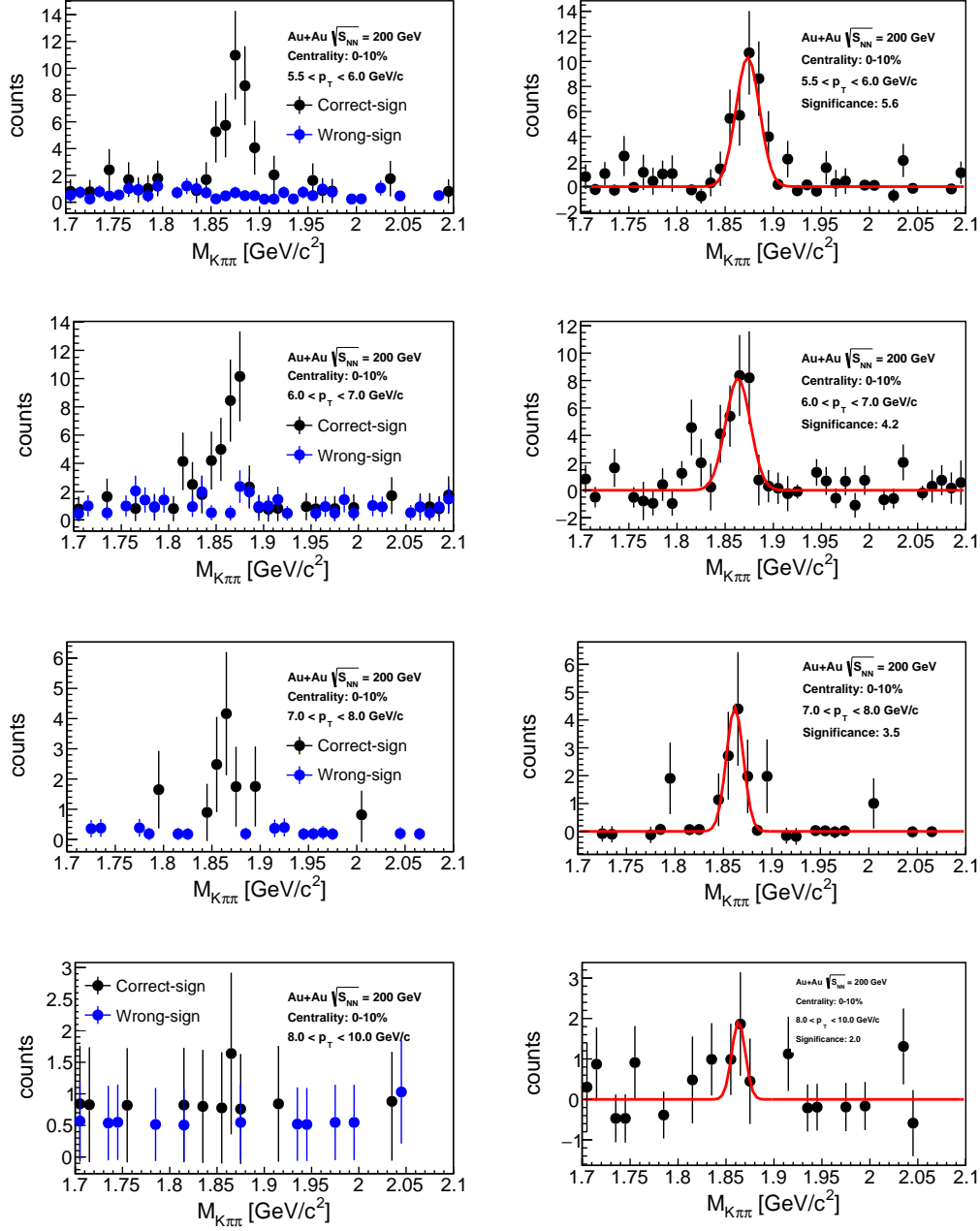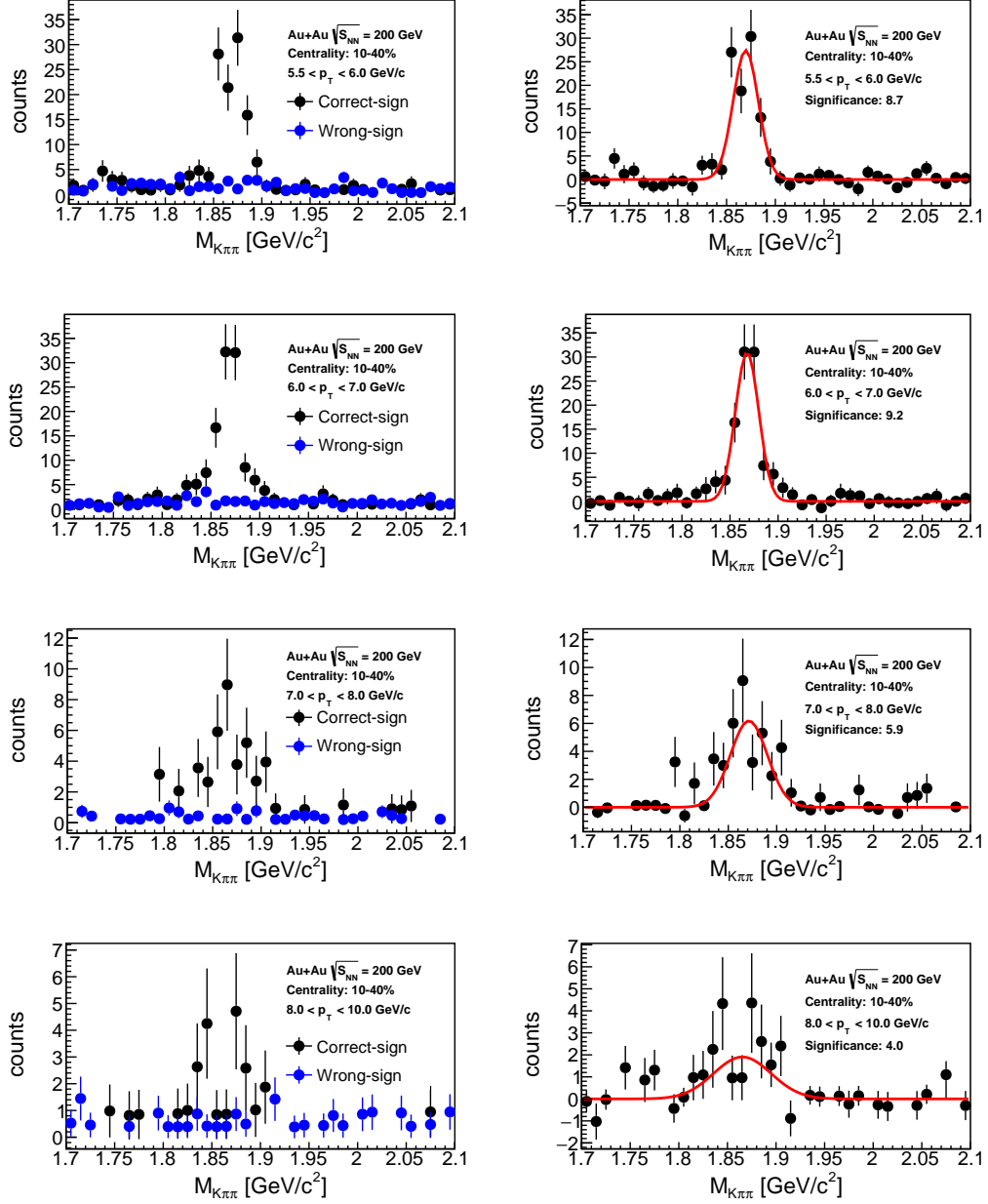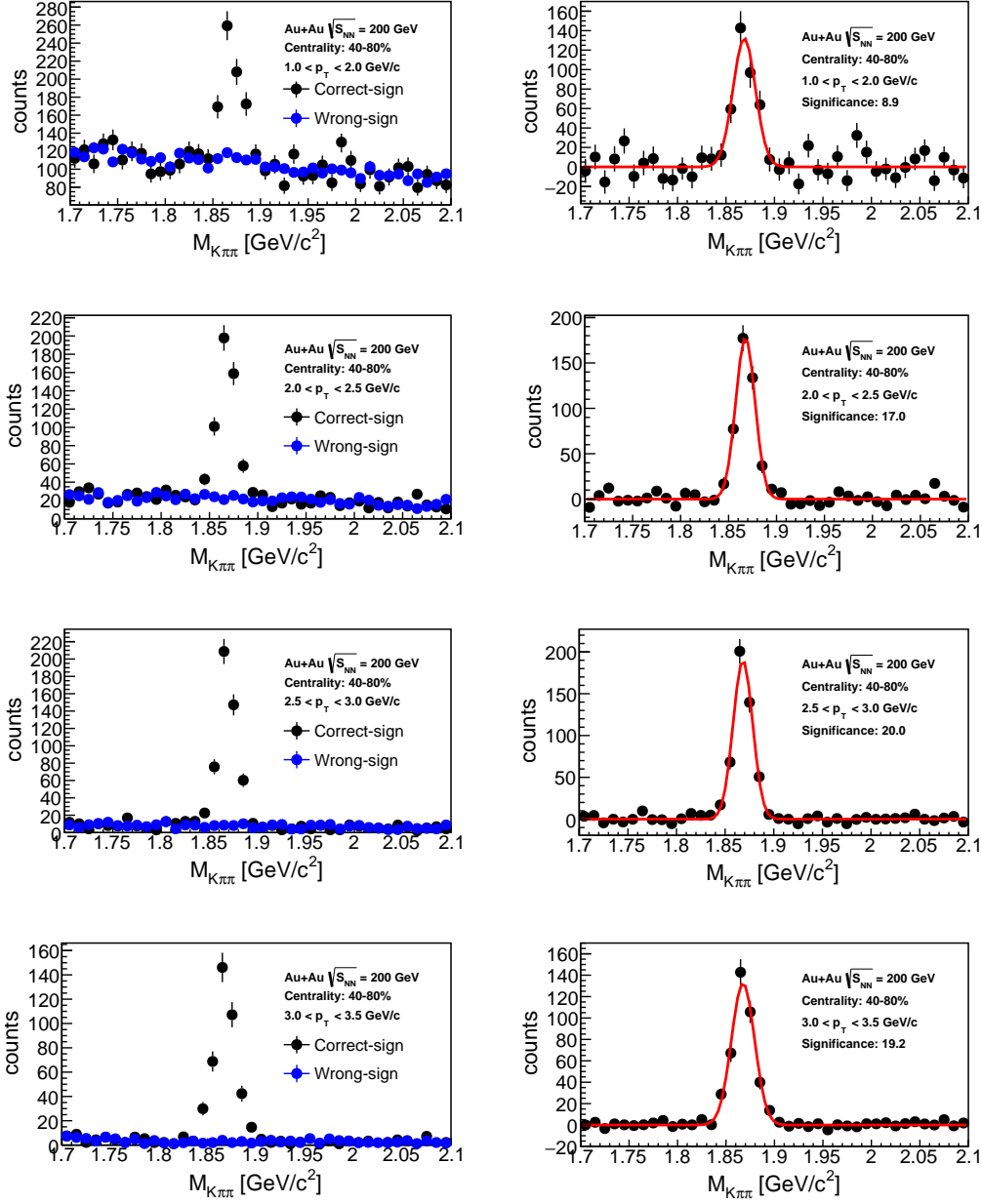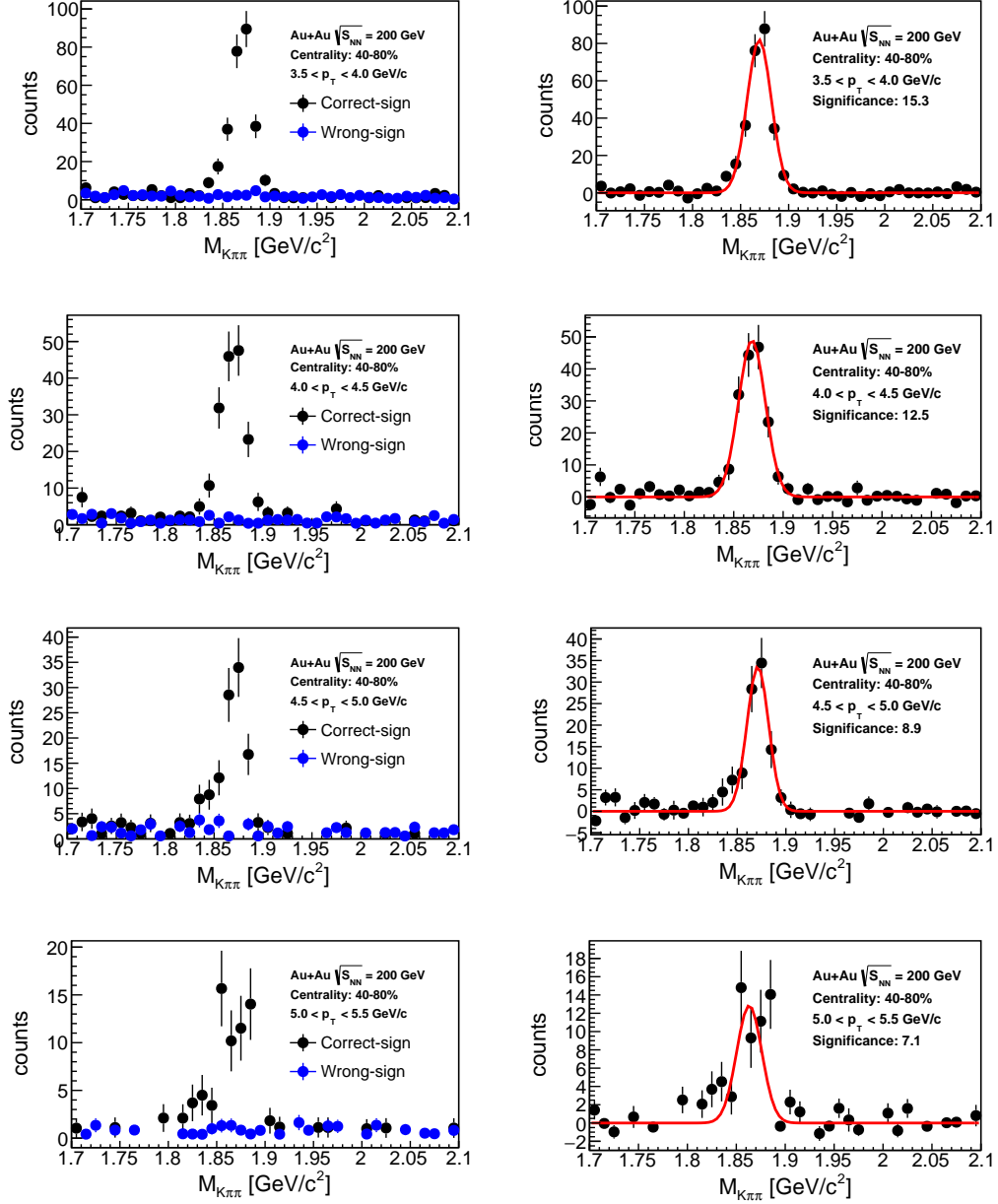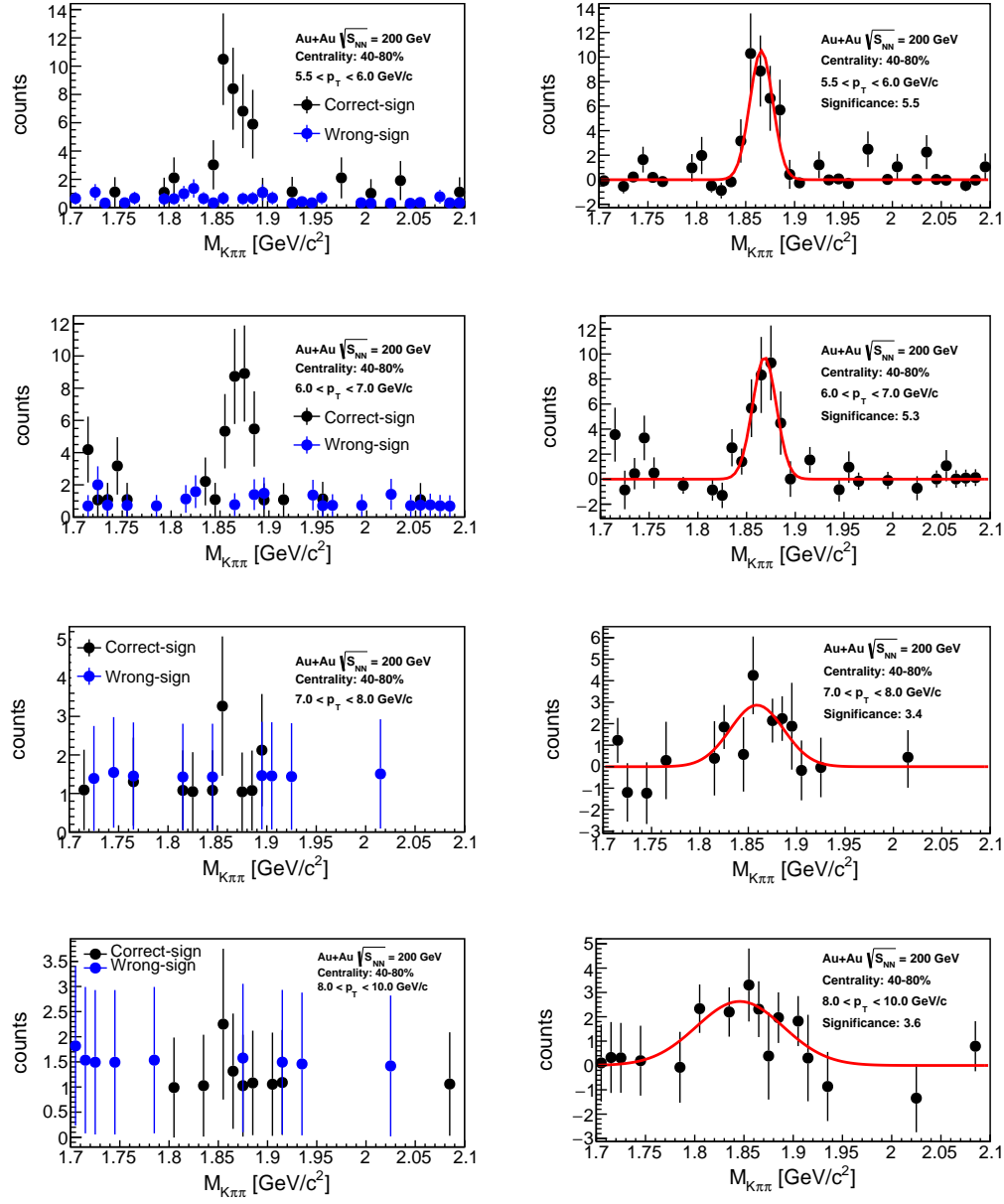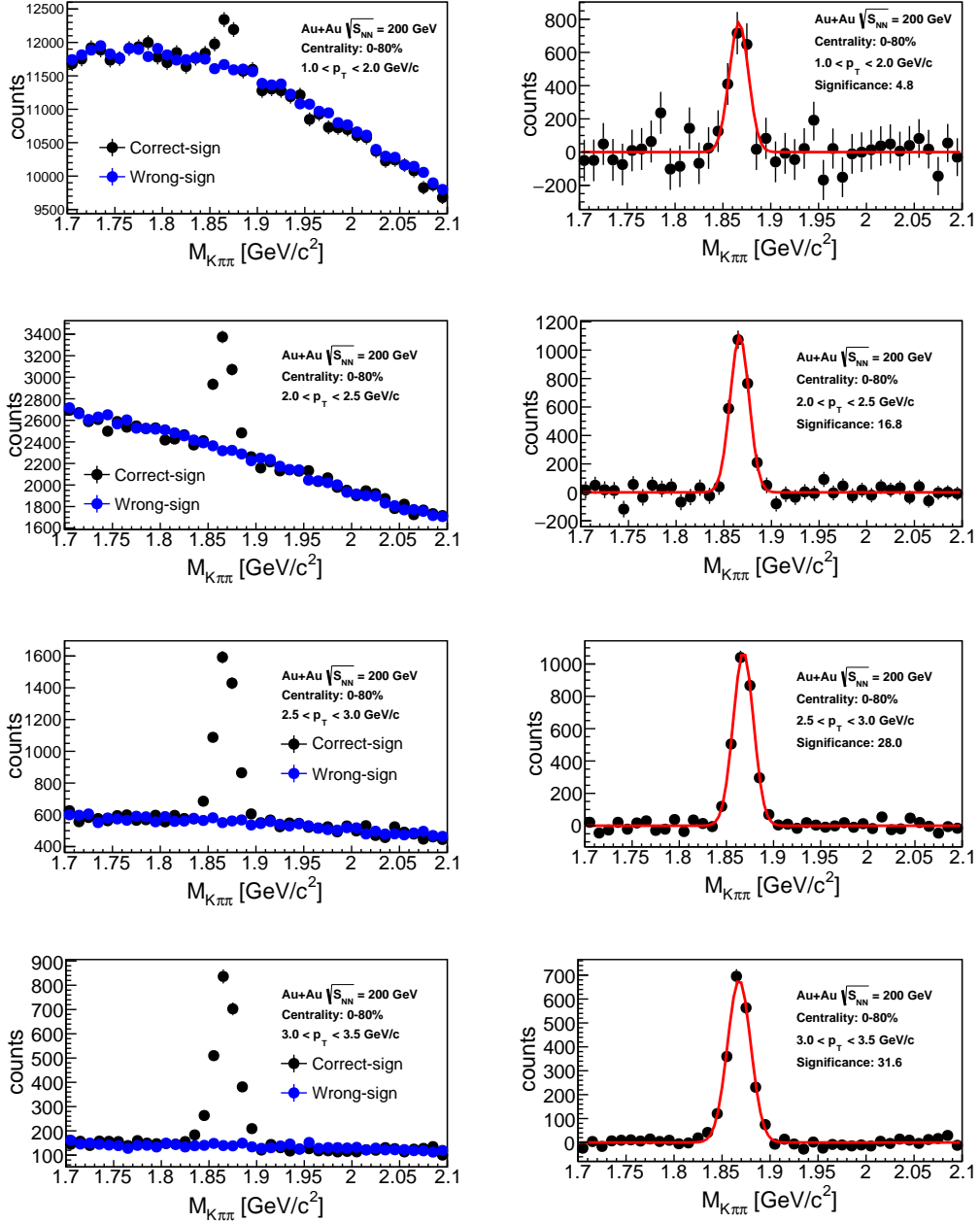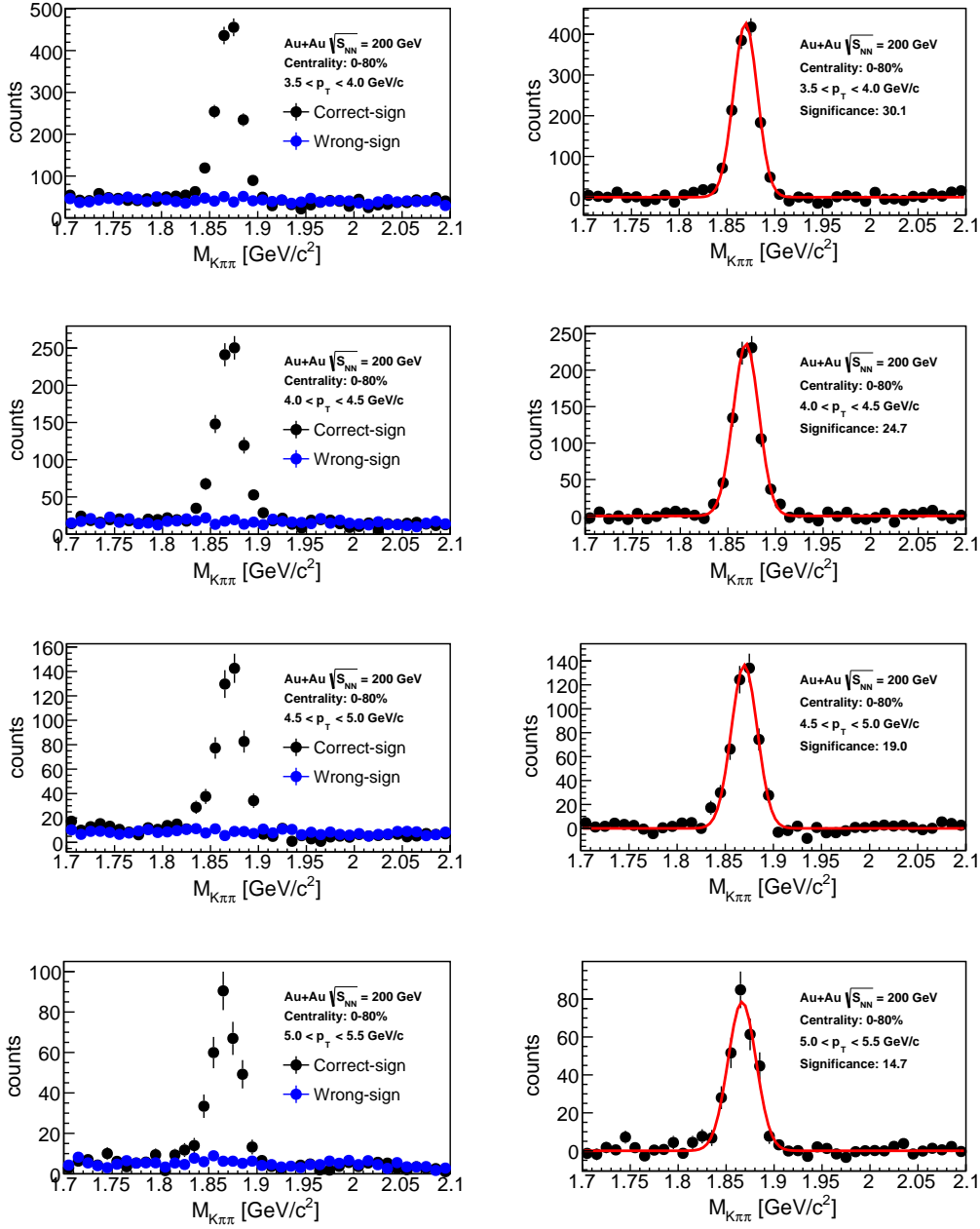
Figure A.3: The D$^\pm$ signal and background in centrality range 0–10% for 4 transverse momentum p_T bins.
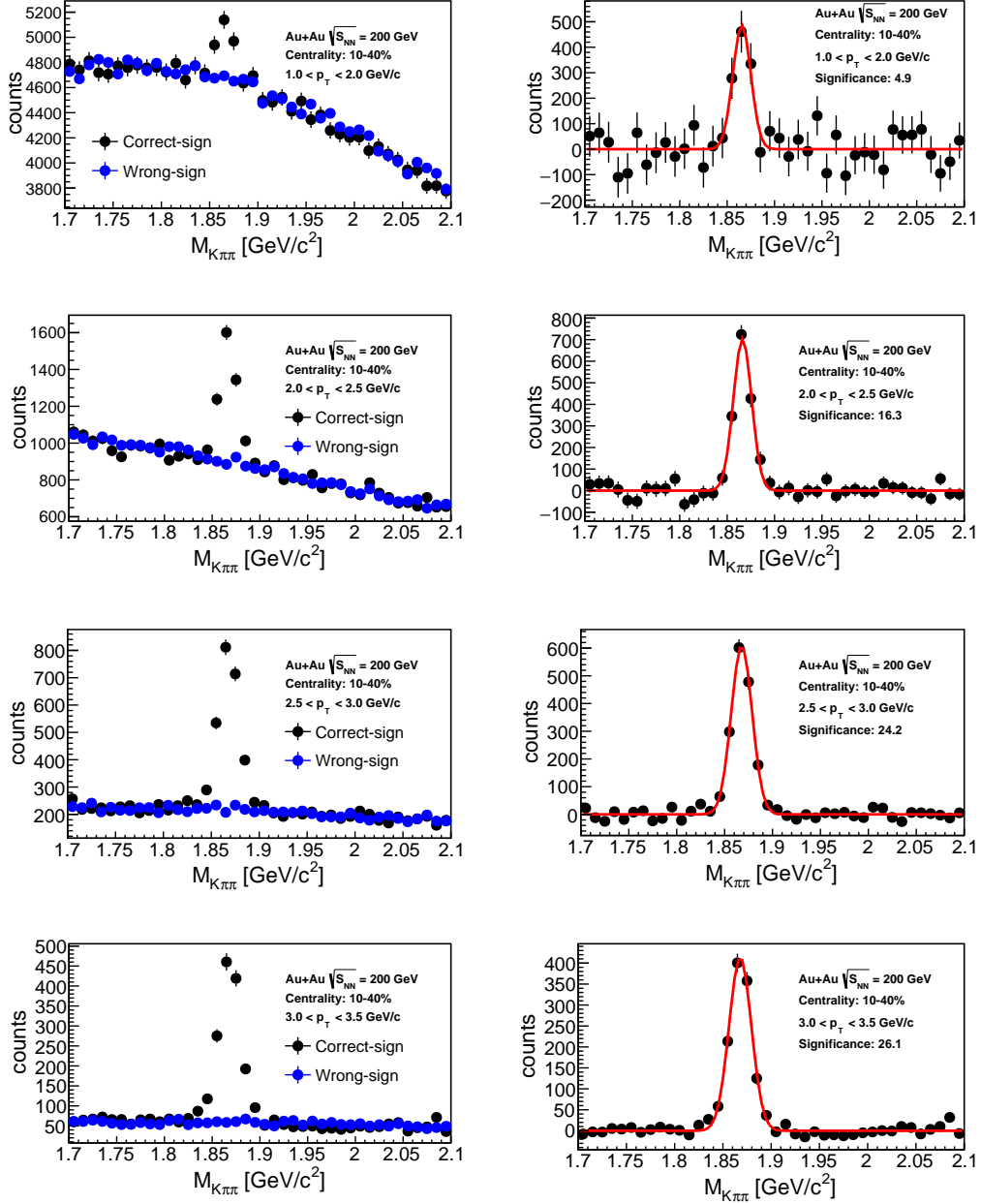
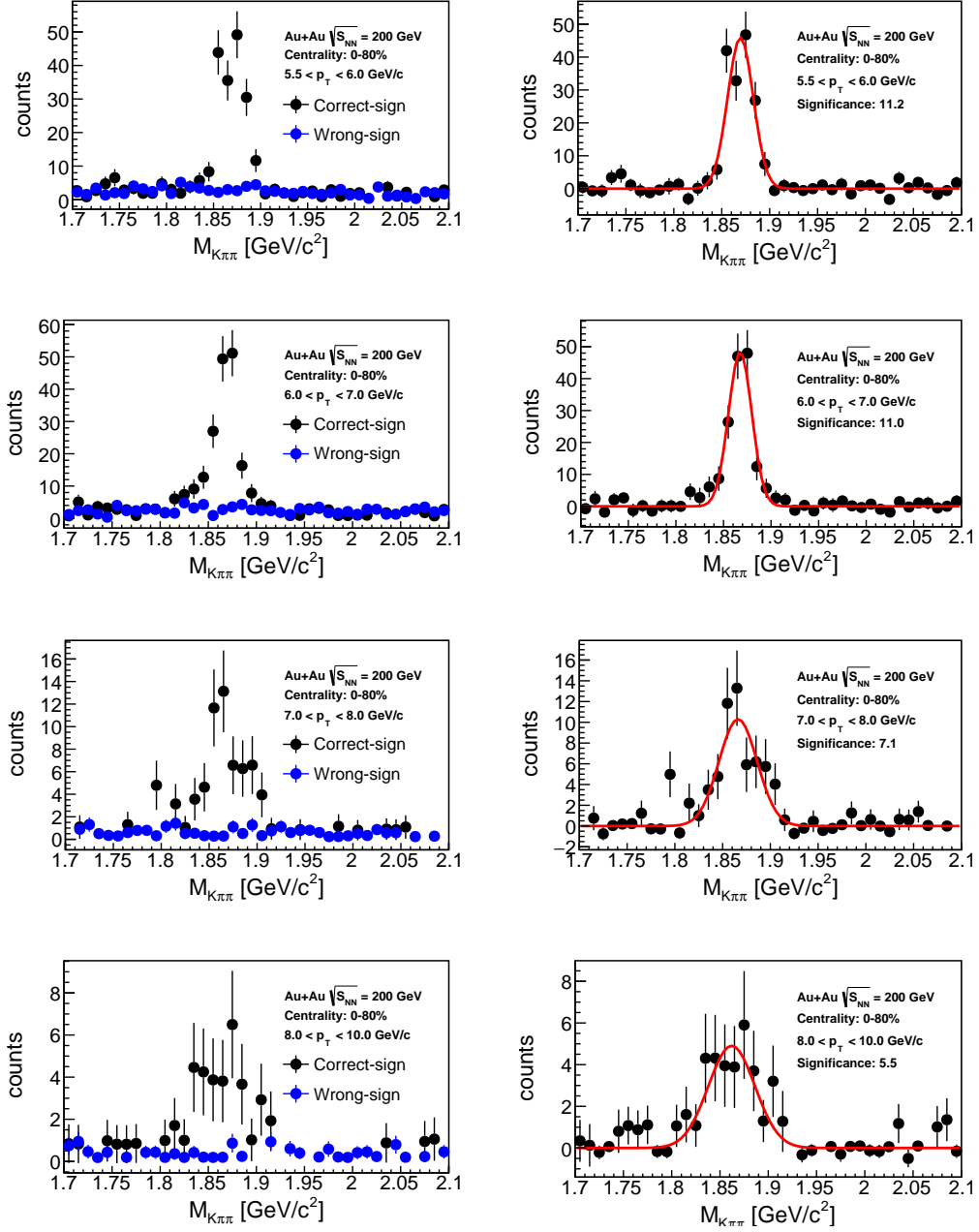Figure A.4: The $D^{\pm}$ signal and background in centrality range 10–40% for 4 transverse momentum p_T bins.

Figure A.5: The D$^{\pm}$ signal and background in centrality range 10–40% for 4 transverse momentum p_T bins.

Figure A.6: The D$^{\pm}$ signal and background in centrality range 10–40% for 4 transverse momentum p_{T} bins.

Figure A.7: The D$^\pm$ signal and background in centrality range 40–80% for 4 transverse momentum p_T bins.

Figure A.8: The D$^\pm$ signal and background in centrality range 40–80% for 4 transverse momentum p_T bins.

Figure A.9: The D$^{\pm}$ signal and background in centrality range 40–80% for 4 transverse momentum p_{T} bins.

Figure A.10: The $D^{\pm}$ signal and background in centrality range 0–80% for 4 transverse momentum p_T bins.

Figure A.11: The D$^{\pm}$ signal and background in centrality range 0–80% for 4 transverse momentum p_T bins.

Figure A.12: The $D^{\pm}$ signal and background in centrality range 0–80% for 4 transverse momentum p_T bins.

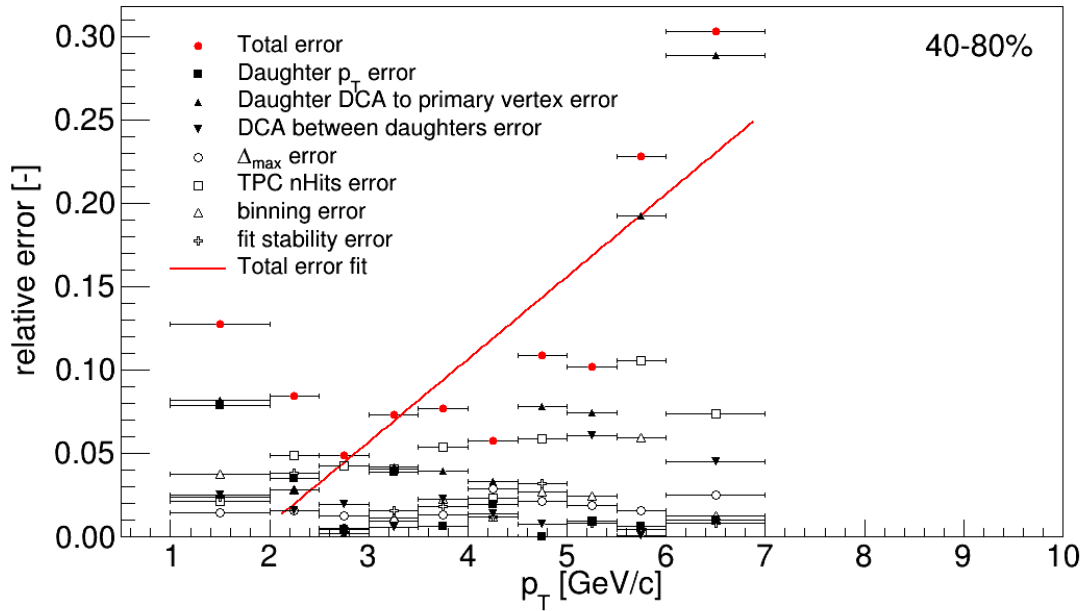# Appendix B

Systematic uncertainties
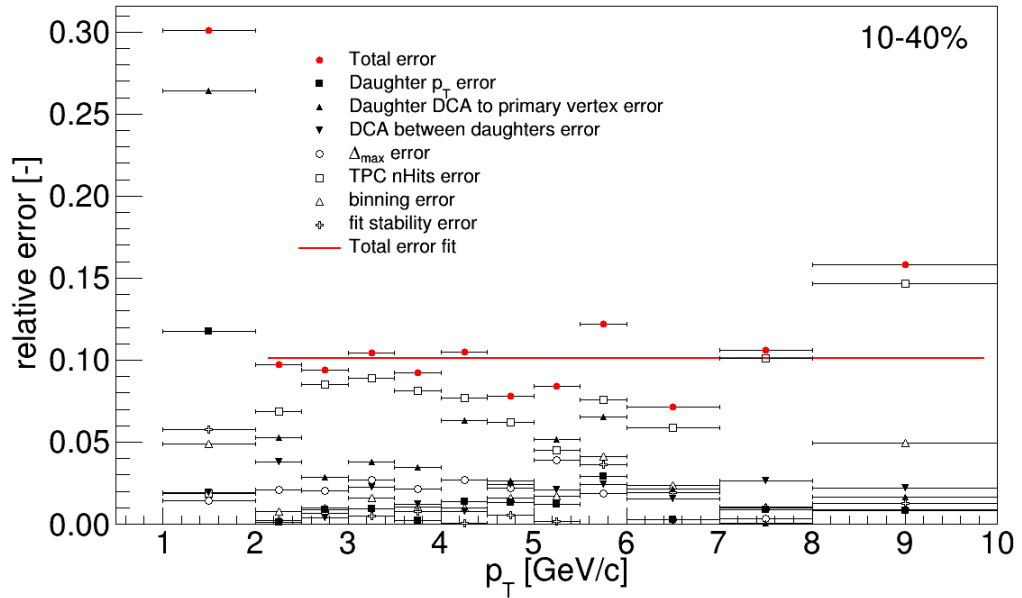
Figure B.1: The $D^{\pm}$ systematic uncertainty for 10–40%. Red circle represent total relative systematic uncertainty calculated with equation (5.4) and rest represent relative systematic uncertainty for each variation. Red curve is first order polynomial function to soften bin effect deviation.
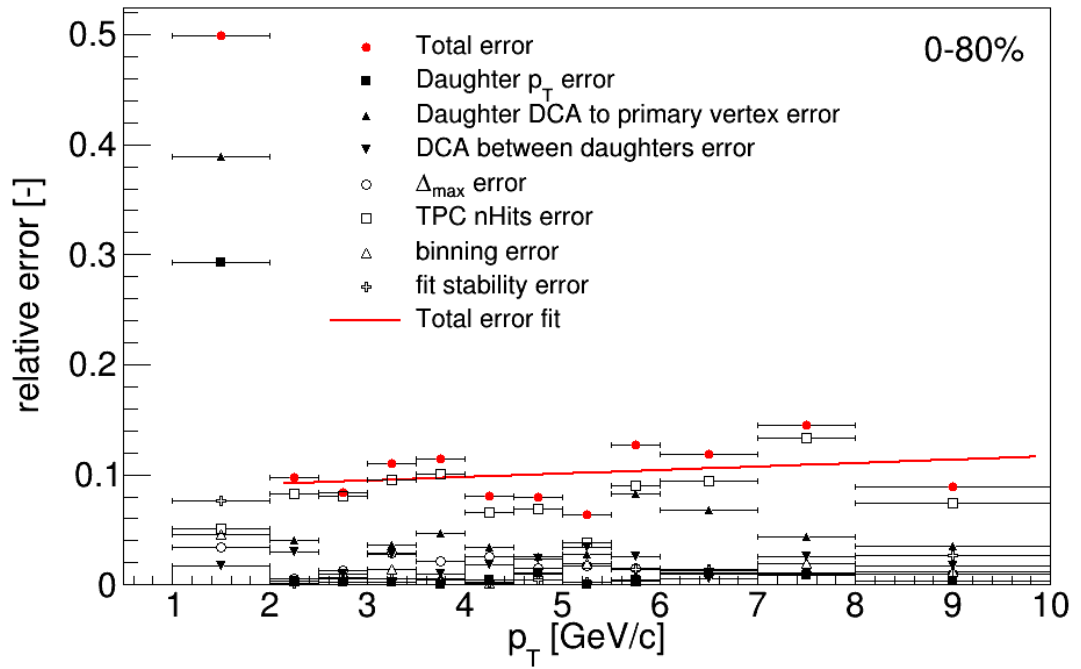
Figure B.2: The D$^{\pm}$ systematic uncertainty for 40–80%. Red circle represent total relative systematic uncertainty calculated with equation (5.4) and rest represent relative systematic uncertainty for each variation. Red curve is first order polynomial function to soften bin effect deviation.

Figure B.3: The D$^{\pm}$ systematic uncertainty for 0–80%. Red circle represent total relative systematic uncertainty calculated with equation (5.4) and rest represent relative systematic uncertainty for each variation. Red curve is first order polynomial function to soften bin effect deviation.

Appendix C

List of public posters

1. Talk from 15th Zimányi School, Wigner Research Centre for Physics, Budapest, Hungary, December 2015 – online: `https://indico.cern.ch/event/464154/overview`.

2. Poster from Quark Matter 2017 conference, Chicago, USA, February 2017. and 53rd Karpacz Winter School of Theoretical Physics, Karpacz, Poland, March 2017 – award: Best experimental poster.

D± meson production in Au+Au collisions at $\sqrt{s_{NN}} = 200$ GeV measured by the STAR experiment

Jakub Kvapil, *for the STAR Collaboration*
Faculty of Nuclear Sciences and Physical Engineering
Czech Technical University in Prague
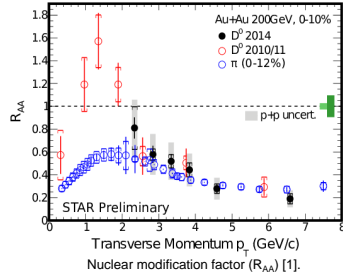
STAR

Quark Matter 2017

Abstract

Charm quarks are mainly created in hard processes at the beginning of heavy-ion collisions and can be used as a tool to study properties of the Quark-Gluon Plasma (QGP). The modification to D-meson production in heavy-ion collisions is sensitive to the energy loss of charm quarks in the QGP. The Heavy Flavor Tracker was installed at the STAR experiment in 2014 and enables the topological reconstruction of the decay vertices for open charm mesons. It significantly improves precision on charm meson measurements. Besides the measurement of D^0, $D^\pm$ provides an additional handle and cross-check to study the interaction between charm quarks and the medium. In this poster, we present measurements of $D^\pm$ production in Au+Au collisions at $\sqrt{s_{NN}} = 200$ GeV. $D^\pm$ mesons are reconstructed topologically via the hadronic decay channel $D^\pm \to K^\mp \pi^\pm \pi^\pm$ from the data collected in 2014 with the Heavy Flavor Tracker. The invariant yield of $D^\pm$ mesons in the transverse momentum range of $2 < p_T < 10$ GeV/c is extracted for 0-10% most central Au+Au collisions, and is found to be consistent with the D^0 yield.
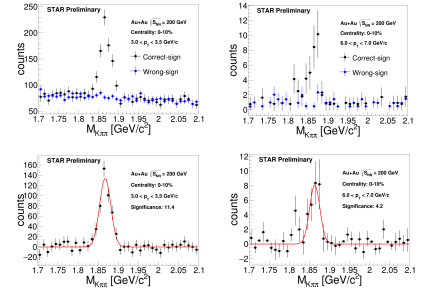
Motivation

- Heavy quarks are mostly created in the initial phase of heavy-ion collisions. Therefore they experience the entire evolution of the system and are a good probe to study the properties of the Quark-Gluon Plasma (QGP).
- The strong suppression of high-p_T D^0 meson yields indicates large energy loss of charm quarks in the QGP.
- Besides the D^0 meson, $D^\pm$ provides an independent handle to study the charm quark interaction with the medium.
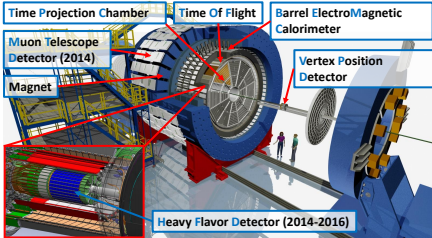

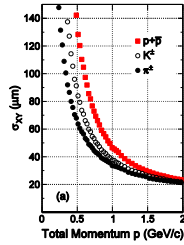Nuclear modification factor (R_{AA}) [1].

STAR detector

- The Solenoidal Tracker at RHIC (STAR) was designed to investigate the strongly interacting matter. It covers full azimuth at mid-rapidity ($|\eta| < 1$) with 0.5 T of solenoidal magnetic field.
- Main sub-detectors used in this analysis are:
  1. Time Projection Chamber (TPC): main tracking device, particle identification via specific energy loss dE/dx, momentum reconstruction.
  2. Time Of Flight (TOF): low p_T particle identification via velocity $1/\beta$.
  3. Heavy Flavor Tracker (HFT) [2]: new inner tracking system composed of three silicon detectors – the PIXEL made of two Monolithic Active Pixel Sensors layers, Intermediate Silicon Tracker (IST) and Silicon Strip Detector (SSD).


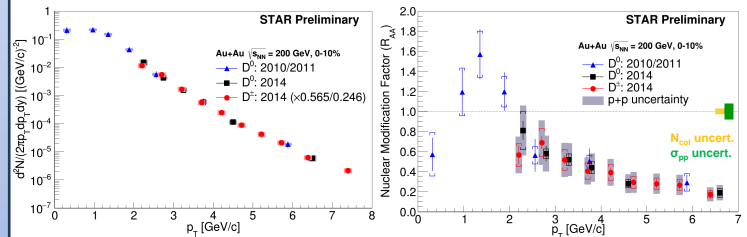STAR detector with main mid-rapidity detectors.

HFT resolution [3].

D± reconstruction

- About 900 million minimum-bias Au+Au events at $\sqrt{s_{NN}} = 200$ GeV recorded in year 2014 are used for this analysis.
- **Event selection cuts:**
  - Vertex position $|V_z| < 6$ cm
  - Vertex correlation $|V_z(VPD)-V_z| < 3$ cm.
- **Track selection cuts:**
  - Hits in the two PIXEL and one IST layers are required.
  - At least 20 space points in the TPC for track reconstruction.
  - Pseudo-rapidity: $|\eta| < 1$.
- **Topological cuts:**
  - Daughter DCA to primary vertex: $DCA_\pi > 100$ μm, $DCA_K > 80$ μm.
  - Pointing angle of reconstructed vertex to primary vertex: $\cos(\theta) > 0.998$.
  - $D^\pm$ decay length between 30 μm and 2000 μm (PDG $c\tau$ = 311.8 μm).
  - DCA between daughter pairs: $DCA_{pair} < 80$ μm.
  - Longest edge of the triangle formed by reconstructed daughter pair vertices must fulfil $\Delta_{max} < 200$ μm.
- **Particle identification:**
  - Daughter $p_T > 500$ MeV/c.
  - TPC: $|n\sigma_\pi| < 3.0$ for pions and $|n\sigma_K| < 2.0$ for kaons.
  - TOF: $|1/\beta-1/\beta_\pi| < 0.03$ for pions and $|1/\beta-1/\beta_K| < 0.03$ for kaons. TOF information is used when available, otherwise only TPC is used.

$D^\pm$ three body decay, DCA_{pair} (blue lines), Δ_{max} (red lines).

D± raw yields

- The Hadronic decay channel $D^\pm \to K^\mp \pi^\pm \pi^\pm$ is used.
- Background is estimated via the wrong-sign method: 2 correct-signal (D^+, D^-) and 6 wrong-signal (background) combinations.
- $D^\pm$ raw yields and significance are calculated using the bin-counting method in the 0-10% central Au+Au collisions for $2 < p_T < 10$ GeV/c.
- Significance: $\frac{signal}{\sqrt{signal+background}}$

Acceptance and reconstruction efficiency

- Data-driven fast simulator has been developed using
  1. centrality-dependent V_z distributions from data
  2. ratio of HFT matched tracks to TPC tracks from data
  3. TPC efficiency and momentum resolution from embedding
  and validated with full GEANT simulation.
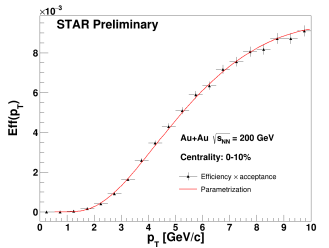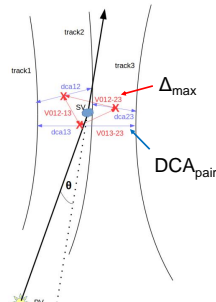

Results

- The $D^\pm$ raw yield is corrected using the following formula:
$$\frac{d^2N}{dp_T dy}\frac{1}{2\pi p_T} = \frac{Yield_{uncorrected}}{2\cdot\pi\cdot N_{charge}\cdot N_{events}\cdot BR\cdot p_T\cdot\Delta p_T\cdot\Delta y\cdot Eff(p_T)}$$
  where $N_{charge} = 2$, N_{events} number of events, BR = (9.13±0.19)%, Δp_T bin width, Δy rapidity width, $Eff(p_T)$ detector acceptance x efficiency.
- Systematic uncertainties are estimated by varying cuts on daughter p_T, daughter DCA, DCA_{pair}, Δ_{max}, TPC fit points, changing histogram binning and testing fit stability.
- The D^0 spectrum in p+p collisions measured using 2009 data is used as the baseline.

- The invariant yield of $D^\pm$ mesons with $2 < p_T < 8$ GeV/c in 0-10% central Au+Au collisions is consistent with that of D^0 mesons within uncertainties. The nuclear modification factor (R_{AA}) for $D^\pm$ also exhibits strong suppression at high p_T, indicating substantial energy loss of charm quarks in the medium.

Conclusion

- The $D^\pm$ invariant yield spectrum in 0-10% central Au+Au collisions at $\sqrt{s_{NN}} = 200$ GeV is measured via the hadronic decay channel $D^\pm \to K^\mp \pi^\pm \pi^\pm$ for the p_T range of 2-8 GeV/c.
- The $D^\pm$ and D^0 yields are consistent, both indicating strong energy losses of charm quarks in the medium.

References

[1] G. Xie, for the STAR Collaboration, Nuclear Physics A, Volume 956, Pages 473-476
[2] J. Schambach, for the STAR Collaboration, Physics Procedia, Volume 66, 2015, Pages 514-519
[3] L. Adamczyk, for the STAR Collaboration, arXiv:1701.06060 [nucl-ex]

ČESKÉ VYSOKÉ UČENÍ TECHNICKÉ V PRAZE

BROOKHAVEN NATIONAL LABORATORY